Measurement-Based Channel Simulation Models for Mobile Communication Systems

Dmitry Umansky

Measurement-Based Channel Simulation Models for Mobile Communication Systems

Doctoral Dissertation for the degree *Philosophiae Doctor (PhD)* in Mobile Communication Systems: Network, Security and Formal Methods

Universitetet of Agder
Faculty of Engineering and Science
2010

Doctoral Dissertations at the University of Agder 24
ISBN: 978-82-7117-671-6
ISSN: 1504-9272

Printed by the Printing Office, University of Agder
Kristiansand

Acknowledgments

I would like to thank my supervisor Prof. Matthias Pätzold. I also want to express my gratitude to Profs. Bernard H. Fleury, Sergei Primak, and Andreas Prinz for being members of the evaluation committee and for their useful suggestions regarding the improvement of the manuscript. I am very thankful to Prof. Valeri Kontorovich, CINVESTAV, Mexico, for many educational and inspiring discussions. My sincere gratitude goes to the Doctoral Fellows (present and former) in the Mobile Communication Group and the ICT department, especially to Adrian Gutierrez, Ali Chelli, Batool Talha, Bjørn O. Hogstad, Gulzaib Rafiq, Ram Kumar, and Yuanyuan Ma. Without their support and generous assistance it would have been much more difficult to complete my PhD study. I would like to acknowledge the members of the research group in UNIK, Oslo, Norway, headed by Are Hjørugnes. I am also thankful to the Project Secretary of the Mobile Communication Group, Katharina Pätzold, and the Coordinator of the PhD Program in the ICT department, Trine Tønnessen.

Last but not least, I would like to thank my parents, my wife Helen, and my son Alexander for their love and devotion. Without their support, I would have hardly come to the final stage of this adventure.

Contents

Summary

Channel simulation models have proved to be an indispensable tool for designing mobile radio communication systems. By means of computer simulations designers are able to assess the performance of wireless communication systems under various propagation conditions without resorting to field trials, which are costly and time consuming. The effectiveness of using channel simulation models to a large extend depends on how accurate the models are in reflecting the most important characteristics of real-world wave propagation environments. Clearly, when the parameters of a channel simulation model are determined from measurement data, a higher level of accuracy can be expected.

In this dissertation, we describe two approaches to designing measurement-based simulation models for mobile wireless communication channels. The first method allows synthesizing channel transfer functions with joint spatial-temporal-frequency correlation properties approximating those of real-world radio channels. The parameters of a channel simulator are determined by fitting the space-time-frequency correlation matrix of the simulation model to the estimated space-time-frequency correlation matrix of a physical channel. For this purpose, an iterative parameter computation algorithm has been developed. In the second approach, a multichannel two-dimensional autoregressive model is proposed for simulating multiple-input multiple-output wideband mobile wireless channels. The parameters of the autoregressive models are estimated from real-world measurement data. We also address the problem of possible instability of the multichannel two-dimensional autoregressive model and develop a model stabilization procedure, which is based on numerical optimization techniques.

The methods proposed for designing measurement-based channel simulation models presume stationarity of radio channels. We discuss a new test for determining the time intervals, over which a wireless channel can be considered stationary. The stationarity intervals are identified by comparing the delay power spectral densities estimated at different time instances. The test is applicable to single-input single-output as well as to multiple-input multiple-output real-world wireless channels.

In this thesis, we also investigate the problem of estimating the velocity of mobile stations. In particular, we analyze to what extend the velocity estimation can

be improved in wideband mobile stations equipped with multiple antennas. For this purpose, a simple algorithm, which is suitable for real-time implementations, has been developed.

List of Publications

1. D. Umansky and M. Patzold, Stationarity test for wireless communication channels, Proc. IEEE Global Communications Conference, IEEE GLOBECOM 2009, Honolulu, Hawaii, USA, Nov./Dec. 2009.

2. D. Umansky and M. Patzold, Design of measurement-based stochastic wideband MIMO channel simulators, Proc. IEEE Global Communications Conference, IEEE GLOBECOM 2009, Honolulu, Hawaii, USA, Nov./Dec. 2009.

3. D. Umansky and M. Patzold, Velocity Estimation in Wideband Mobile Stations Equipped with Multiple Antennas, Proc. IEEE 69th Vehicular Technology Conference, IEEE VTC2009-Spring, Barcelona, Spain, Apr. 2009.

4. D. Umansky and M. Patzold, A Two-Dimensional Autoregressive Model for MIMO Wideband Mobile Radio Channels, Proc. IEEE Global Communications Conference, IEEE GLOBECOM 2008, New Orleans, LA, USA, Nov./Dec. 2008. DOI 10.1109/GLOCOM.2008.ECP.758

5. D. Umansky and M. Patzold, Design of Wideband Mobile Radio Channel Simulators Based on Real-World Measurement Data, Proc. 67th IEEE Vehicular Technology Conference, VTC2008–Spring, Singapore, May. 2008, pp. 319–324.

6. D. Umansky and M. Patzold, Design of Measurement-Based Wideband Mobile Radio Channel Simulators, Proc. 4th IEEE International Symposium on Wireless Communication Systems, ISWCS 2007, Trondheim, Norway, Oct. 2007, pp. 229–235.

7. D. Umansky, M. Patzold, Estimation of Path Gains and Doppler Frequencies from the Temporal Autocorrelation Function of Mobile Fading Channels, Proc. of 13th European Wireless Conference, EW 2007, Paris, France.

List of Figures

List of Tables

Abbreviations

2D	two-dimensional
AR	autoregressive
AWGN	additive white Gaussian noise
BER	bit error rate
BIBO	bounded input bounded output
BS	base station
CCDF	complementary cumulative distribution function
CDF	cumulative distribution function
CLT	central limit theorem
CMF	correlation matrix fitting
COV	covariance-based
CPSD	cross-power spectral density
DFT	discrete Fourier transform
DOA	direction-of-arrival
DOD	direction-of-departure
FACF	frequency autocorrelation function
FCCF	frequency cross-correlation function
FFT	fast Fourier transform
IF	instantaneous frequency
i.i.d.	independent identically distributed
IR	impulse response
KLE	Karhunen-Loève expansion
LCR	level-crossing rate
LS	least-squares
LSI	linear shift-invariant
LRS	local region of stationarity
MIMO	multiple-input multiple-output
MP	matching pursuit
MS	mobile station
MSRE	mean-squared relative error
NSHP	nonsymmetric half-plane
OFDM	orthogonal frequency division multiplexing
PDF	probability density function
PDP	power delay profile
PEM	prediction error minimization
PSD	power spectral density
QP	quarter plane

SAGE	space-alternating generalized expectation-maximization
SISO	single-input single-output
SLAC	stochastic local area channel
SNR	signal-to-noise ratio
TACF	temporal autocorrelation function
TCCF	temporal cross correlation function
TF	transfer function
TLS	total least-squares
TVAR	time-variant autoregressive
TVFR	time-variant frequency response
UCA	uniform circular array
ULA	uniform linear array
UMB	ultra mobile broadband
w.r.t.	with respect to
WSS	wide-sense stationary
WSSUS	wide-sense stationary uncorrelated scattering
YW	Yule-Walker
ZCR	zero-crossing rate

Chapter 1

Introduction

1.1 Classification of Measurement-Based Channel Models

In the development and performance evaluation of wireless communication systems, channel models play an important role. Wireless channel models mathematically describe the essential properties of propagation environments, i.e., the properties that have considerable impact on the performance of radio communication systems. In recent years, a number of wireless channel models have been proposed in the literature, see, e.g., [1–4] and the multiple references therein.

According to the classification presented in [5] and also in [6], wireless channel models can be divided into physical models and analytical (non-physical) models. The parametrization of physical channel models explicitly accounts for the multipath propagation of the electromagnetic waves in wireless channels (consider, e.g., the double-directional model [7]). On the other hand, analytical models describe the statistical properties of the channel system functions, i.e., the impulse responses (IRs) or the transfer functions (TFs), without considering the physical aspects of the wave propagation. As an example representing analytical channel models, we can mention the correlation-based wireless channel models (see, e.g., [6]).

As it follows from the title, in this thesis we consider measurement-based channel models. The term *measurement-based* signifies the fact that some or all of the model parameters are determined from the measured IR or TF of a real-world wireless channel. Certainly, the classification of wireless channel models into physical and analytical ones can also be applied to measurement-based models. However, this classification scheme, which is based solely on the model parametrization, does not always allow us to judge what kind of information can be obtained from the model about a physical propagation channel. In attempt to resolve this issue and also in order to facilitate the interpretation of the results

presented in this thesis, we suggest another classification for measurement-based channel models. The proposed classification is based on the intended usage of a model and, therefore, allows us to differentiate channel models with respect to (w.r.t.) the model parametrization and also to the approach employed for determining the model parameters.

We distinguish between two types of wireless channel models. Models of the first type are oriented to the analysis of wireless channels, while models of the second type – to the synthesis (simulation) of wireless channels. A normal assumption made about a channel model of the first type is that it can adequately predict the behavior of a real-world wireless channel. Thus, by analyzing estimated parameters of the channel model, we obtain information about different properties of the physical radio channel. The double-directional channel model mentioned above, with the parameters estimated from the measured IR of a real-world channel by employing, e.g., the SAGE [8] or RIMAX [9] algorithms, can serve as an example of channel models of the first type.

On the other hand, the task delegated to channel models of the second type is of different nature. It consists in simulating wireless channels with *specified* statistics. Here, in contrast to the analysis task, we accept the fact that there might be more than one channel model parametrization that allows to synthesize channels with the specified statistical properties. The measurement-based channel simulation models constitute the main subject of this dissertation.

It should be noted that models of the first type can also be used to synthesize the channel IRs (TFs).

1.2 Measurement-Based Channel Simulation Models

The main virtue of channel simulation models designed based on measurement data is the capability of synthesizing realistic channel system functions. Furthermore, the advantage of resorting to measurement-based channel simulation models as compared to the stored TFs or IRs of real-world channels [4], becomes clear when we consider, as an example, the problem of estimating the bit error rate (BER) for a wireless communication system. A reliable estimation of the BER requires a large number of samples of the measured channel system functions. Consequently, it becomes prohibitively expensive (if possible) to acquire and store a required amount of measurement data, particularly for wideband multiple-input multiple-output (MIMO) channels. A feasible alternative is to use a measurement-based channel simulation model to assess this important system performance characteristic.

As it has been pointed out above, channel simulation models are aimed to generate realizations of the channel system functions with *specified* statistics. Under *specified* statistics, we understand the important first- and second-order statistical

characteristics, e.g., the probability density function (PDF) of the channel gains at different time instances and frequencies and the various correlation functions (see, e.g., [10]). In the following, our attention will be mainly concentrated on the correlation properties of the simulated channel system functions in time, frequency, and space. These second-order statistical characteristics of fading channels drastically affect the performance of many signal processing techniques including interleaving, error-correction coding, diversity, frequency hopping, and equalization [11]. Additionally, analytical performance analysis of wireless communication systems utilizing these processing techniques is very difficult. Thus, accurate representation of the correlation properties of fading channels in simulation models is particularly important.

For measurement-based channel simulation models, the statistics of interest are estimated from the measured system functions of real-world channels. The system functions of real-world channels are obtained by using channel sounders[1] during measurement campaigns (see, e.g., [12]).

It is worth mentioning that the problem of simulating channel system functions essentially falls into a more general framework of synthesizing realizations of random processes with specified first- and second-order statistics. This general problem has been studied in the literature (see, e.g., [13–15]).

In the previous subsection, we noted that there might exist more than one model parametrization allowing simulating the channel TFs or IRs with specified statistics. Thus, a practical approach to designing measurement-based channel simulation models starts with finding a model parametrization, which satisfies certain criteria, e.g., low computational load in synthesizing channel TFs, a small number of the channel simulation model parameters, etc. In the following chapters, we discuss two approaches to designing measurement-based simulation models for wireless communication channels. In these approaches, we have taken into account the following considerations:

- A model parametrization should be suitable for constructing measurement-based channel simulation models for narrowband single-input single-output (SISO) as well as narrowband MIMO time-variant wireless communication channels.

- A model parametrization should be suitable for constructing measurement-based channel simulation models for wideband SISO and wideband MIMO time-variant wireless channels.

- A model parametrization and methods for determining the values of the model parameters should enable constructing channel simulation models

[1] Hereafter, we presume that the measured system functions of real-world channels are digitized and converted to the complex baseband.

based on real-world wireless channels corresponding to various propagation environments, e.g., outdoor and indoor propagation environments.

- A model parametrization and methods for determining the values of the model parameters should enable constructing measurement-based channel simulation models without assuming separability of the channel correlation properties in time, frequency, and space (see, e.g., [16]).
- The parameters of the measurement-based channel simulation models should be determined efficiently.

1.3 Organization of the Thesis

The rest of the thesis is organized as follows. In Chapter 2, we describe a statistical test proposed for determining the intervals of stationarity for wireless communication channels. The stationarity test has been applied to several radio communication channels measured in different propagation scenarios. The results of the analysis of the identified stationarity intervals are presented. In Chapter 3, we discuss a method for designing measurement-based stochastic models for simulating wideband MIMO wireless channels. The proposed approach allows synthesizing channel TFs with the spatial-temporal-frequency correlation properties approximating those of real-world radio channels. In this chapter, we also present two modifications of the method for creating measurement-based channel simulation models for narrowband MIMO and wideband SISO channels, respectively. The multichannel two-dimensional (2D) autoregressive (AR) model for MIMO wideband mobile wireless channels is presented in Chapter 4. In Chapter 5, we consider the problem of estimating the velocity of mobile stations (MSs) in wireless communication systems. In particular, we investigate to what extend the velocity estimation can be improved in wideband MS equipped with multiple antennas. For this purpose, we develop a simple velocity estimation algorithm. The performance of the algorithm is assessed by simulations. Finally, we summarize the results presented in this thesis in Chapter 6.

Chapter 2

Stationarity of Wireless Communication Channels

2.1 Introduction

Chapters 3 and 4 of this thesis deal with modeling of mobile wireless communication channels. The channel models considered in these chapters presume the wide-sense stationarity of randomly time-variant radio channels [10]. In practice, however, real-world channels often demonstrate 'quasi-stationary' behavior, i.e., the assumption of wide-sense stationarity can be accepted only for limited intervals of time and frequency [10, 17]. The simplest way to justify the quasi-stationarity of a measured wireless channel is by taking into account the physical arguments such as the transmitter/receiver speed, the frequency bandwidth, the distance to the scatterers surrounding the transmitter/receiver, etc. Unfortunately, the choice of stationarity intervals based on these simple physical considerations is not always valid. Thus, it is important to develop a test procedure that can be used to reliably identify regions of stationarity for wireless channels.

A number of stationarity tests have been proposed in the literature related to such disciplines as wireless channel modeling, spectrum analysis, signal detection, etc. The correlation between consecutive 'instantaneous' delay power spectral densities (PSDs) has been used in [18] to identify the local region of stationarity (LRS) for wireless channels. A nonstationarity detector based on the time-variant autoregressive (TVAR) model has been described in [19]. In [20], the authors suggest to identify the intervals of stationarity by analyzing changes in the wavenumber spectrum estimated at different locations. The use of the nonparametric *run*-test [21] for determining the stationarity intervals of radio channels has been investigated in [22]. An interesting test for wide-sense stationarity of MIMO wireless channels has been developed in [23]. This approach is based on analyzing the evolutionary spectrum of a signal estimated at different instances of time [24].

Also one cannot help mentioning the tests for stationarity developed based on the time-frequency (time-scale) analysis of signals (see, e.g., [25,26]).

In the development of the stationarity test proposed in [27] and presented below in this chapter, the primary importance has been assigned to analyzing the statistical properties of radio channels without time averaging, under condition that the available frequency bandwidth allows that. Time averaging intrinsically leads to a contradiction, i.e., the test validates the stationarity of the data by presuming its stationarity on intervals determined by the length of the window. Often (if not always), the length of the window is chosen heuristically by conducting preliminary eyeball analysis of the measurement data. The proposed approach allows to skip windowing of the measurement data in time. Hence, a greater level of automation in the test procedure can be provided. The proposed test is based on the hypothesis that the estimated delay PSD of a channel does not change with time over the interval of stationarity. The test is applicable both to SISO and MIMO radio channels. The design of the test procedure relies on the definition of a random (multivariate) wide-sense stationary (WSS) process (see, e.g. [28]). It is assumed that the time-variant frequency response (TVFR) of a channel is WSS (jointly WSS for MIMO channels) w.r.t. frequency. However, it appears that this assumption is not restrictive, if, similar to [18], the channel stationarity intervals are defined as the intervals over which the locations of the scatterers, transmitter, and receiver do not change significantly.

This chapter is organized as follows. In Section 2.2, the stationarity test for SISO and MIMO wireless communication channels is developed. The results of the performance evaluation for the developed test are presented in Section 2.3. The analysis of the stationarity intervals for several real-world propagation environments is presented in Section 2.4. The concluding remarks are given in Section 2.5.

2.2 Stationarity Tests

Let the TVFR $H(f',t)$ describing a SISO wireless channel in frequency f' and time t be a complex 2D random process. It is assumed that the TVFR $H(f',t)$ is an ergodic process w.r.t. frequency f'.

Wide-sense stationarity of the TVFR $H(f',t)$ w.r.t. time t implies that the delay PSD is time-invariant. This observation forms the basics of the statistical test proposed for validating the hypothesis that the measured TVFR $H(f',t)$ is a WSS processes w.r.t. time t.

In the following subsection, the stationarity test for SISO wireless channels is described. In Subsection 2.2.2, the procedure will be extended to test the stationarity of MIMO radio channels.

2.2.1 Stationarity Test for SISO Channels

Suppose that the TVFR $H(f',t)$ of a SISO radio channel has been measured at discrete frequencies $f'_m = -B/2 + m\triangle f' \in [-B/2, B/2]$, $m = 0, \ldots, M-1$, and at discrete time instances $t_n = n\triangle t \in [0, T]$, $n = 0, \ldots, N-1$. Hereafter, the sampling interval in the frequency domain is signified by $\triangle f'$, while $\triangle t$ stands for the sampling interval in the time domain. The frequency bandwidth and the measurement time interval are denoted as B and T, respectively. The measured TVFR of the channel can be represented in a matrix form

$$\mathbf{H} = \begin{pmatrix} H[0,0] & \ldots & H[0,N-1] \\ \vdots & \ddots & \vdots \\ H[M-1,0] & \ldots & H[M-1,N-1] \end{pmatrix}. \tag{2.1}$$

The elements $H[m,n]$ of the matrix $\mathbf{H}$ in (2.1) are complex random variables. As it was mentioned above, it is assumed that the columns of the channel matrix $\mathbf{H}$, i.e., the snapshots of the channel TVFR at time instances t_n, are ergodic processes. Thus, for each of these processes, the mean can be determined as

$$\eta[n] = \langle H[m,n] \rangle_{f'} \tag{2.2}$$

and the frequency autocorrelation function (FACF) is given by

$$r_{f'}[\kappa, n] = \langle H[m,n] H^*[m+\kappa, n] \rangle_{f'} \tag{2.3}$$

where * designates the complex conjugate and $\langle \cdot \rangle_{f'} = \frac{1}{M} \sum_{m=0}^{M-1} (\cdot)$ denotes averaging over frequency.

The delay PSD of the radio channel at time t_n is given by

$$P(\tau', t_n) = \triangle f' \sum_{\kappa=-\infty}^{\infty} r_{f'}[\kappa, n] e^{-j2\pi\tau'\kappa\triangle f'}. \tag{2.4}$$

where τ' stands for the propagation delay.

According to the definition, wide-sense stationarity of the TVFR $\mathbf{H}$ w.r.t. time requires that the mean $\eta[n]$ and the FACF $r_{f'}[\kappa, n]$ are time-invariant, i.e.,

$$\eta[n] = \eta \tag{2.5}$$

$$r_{f'}[\kappa, n] = r_{f'}[\kappa]. \tag{2.6}$$

Condition (2.6) corresponds to the time-invariance of the delay PSD $P(\tau', t_n)$, which can be written as

$$P(\tau', t_n) = P(\tau'). \tag{2.7}$$

Using (2.7), the null hypothesis $\mathcal{H}_0$ can be formulated as follows

$$\mathcal{H}_0 : \big(P(\tau', t_{n_1}) - P(\tau', t_{n_2})\big) = 0, \qquad t_{n_1} \neq t_{n_2} \tag{2.8}$$

which implies that the delay PSD at time t_{n_1} equals the delay PSD at time t_{n_2}.

Note that the hypothesis $\mathcal{H}_0$ also suggests the equality of the mean values, i.e., $\eta[n_1] = \eta[n_2]$. This follows from the observation that

$$\int_{-\infty}^{\infty} P(\tau', t_n) d\tau' = r_{f'}[0, n] = \sigma^2[n] + \eta^2[n] \tag{2.9}$$

where $\sigma^2[n]$ denotes the variance $\sigma^2[n] = \langle (H[m, n] - \eta[n])(H[m, n] - \eta[n])^* \rangle_{f'}$.

The procedure presented below allows to compare the delay PSDs estimated at two different time instances[1] and to determine whether the hypothesis $\mathcal{H}_0$ can be excepted.

The following five-step data processing algorithm significantly simplifies the statistical analysis of the null hypothesis $\mathcal{H}_0$.

Step 1. The n-th column of the channel matrix $\mathbf{H}$ in (2.1) is divided into K nonoverlapping segments each of length M_s. The restriction imposed here is $K > M_s$. Let

$$x_m^{(k)} = H[(k-1)M_s + m, n], \quad m = 0, \ldots, M_s - 1 \tag{2.10}$$

denote a complex data sequence corresponding to the k-th segment, $k = 1, \ldots, K$.

Step 2. For each of the K sequences $\{x_m^{(k)}\}_{m=0}^{M_s-1}$, $k = 1, \ldots, K$, calculate the periodogram at the discrete delays $\tau'_q = \frac{q}{M_s \triangle f'}$, $q = 0, \ldots, M_s - 1$, i.e.,

$$\hat{P}_q^{(k)} = \frac{\triangle f'}{M_s} \left| \sum_{m=0}^{M_s-1} x_m^{(k)} e^{-j2\pi\tau'_q \triangle f' m} \right|^2 . \tag{2.11}$$

It is known (see, e.g., [29]) that asymptotically ($M_s \to \infty$)

$$\hat{P}_q^{(k)} \sim \begin{cases} P_q \chi_2^2/2, & q = 1, \ldots, \frac{M_s}{2} - 1, \frac{M_s}{2} + 1, \ldots, M_s - 1 \\ P_q \chi_1^2, & q = 0 \text{ and } \frac{M_s}{2} \end{cases} \tag{2.12}$$

where χ_1^2 and χ_2^2 signify the chi-square distributions with one and two degrees of freedom, respectively. The symbol $\sim$ stands for the equality in distribution. The true value of the delay PSD at the discrete delay τ'_q is denoted by P_q.

Step 3. For each of the K periodograms $\{\hat{P}_q^{(k)}\}_{q=0}^{M_s-1}$, $k = 1, \ldots, K$, create an

[1] As will be shown shortly, the comparison is actually done in terms of the estimated cepstrum. Recall that the cepstrum of a signal is related to the PSD through an invertible one-to-one transformation.

auxiliary data sequence $\{y_p^{(k)}\}_{p=0}^{2M_s-3}$ as follows

$$y_p^{(k)} = \begin{cases} \hat{P}_p^{(k)}, & p = 0, \ldots, M_s - 1 \\ \hat{P}_{2M_s-2-p}^{(k)}, & p = M_s, \ldots, 2M_s - 3. \end{cases} \tag{2.13}$$

Step 4. For each of the K sequences $\{y_p^{(k)}\}_{p=0}^{2M_s-3}$, $k = 1, \ldots, K$, estimate the cepstrum $\hat{\Phi}_l^{(k)}$ at the discrete frequencies $\omega_l = l\pi/(M_s - 1)$, $l = 0, \ldots, 2M_s - 3$, according to

$$\hat{\Phi}_l^{(k)} = \frac{1}{2M_s - 2} \sum_{p=0}^{2M_s-3} \ln(y_p^{(k)}) e^{j\omega_l p}. \tag{2.14}$$

Here, it is implicitly assumed that $y_p^{(k)} > 0$ for all p, which is true in practical situations. Also note that due to the symmetry in $\{y_p^{(k)}\}_{p=0}^{2M_s-3}$, $\hat{\Phi}_l^{(k)}$ is real and $\hat{\Phi}_{2M_s-2-l}^{(k)} = \hat{\Phi}_l^{(k)}$ for $l = 0, \ldots, M_s - 1$.

It has been shown in [30, 31] that asymptotically, i.e., as $M_s \to \infty$, the estimated cepstrum $\{\hat{\Phi}_l^{(k)}\}_{l=0}^{M_s-1}$ follows the multivariate Gaussian distribution with the covariance matrix $\mathbf{C}$. The matrix $\mathbf{C}$ is a constant diagonal matrix independent of the periodogram $\{\hat{P}_q^{(k)}\}_{q=0}^{M_s-1}$.

Step 5. Stack the estimated cepstrum sequences $\{\hat{\Phi}_l^{(k)}\}_{l=0}^{M_s-1}$, $k = 1, \ldots, K$, as columns into a matrix $\mathbf{U}_n$ of dimensions $M_s \times K$. Let the column vector $\bar{\mathbf{u}}_n$ of dimensions $M_s \times 1$ contain the sample mean of each row of the matrix $\mathbf{U}_n$.

To verify the hypothesis $\mathcal{H}_0$, the algorithm described above is applied to the n_1-th and the n_2-th columns of the channel matrix $\mathbf{H}$ representing the channel frequency response at two distinct time instances t_{n_1} and t_{n_2}. As the outcome, we obtain two matrices $\mathbf{U}_{n_1}$, $\mathbf{U}_{n_2}$ and two column vectors $\bar{\mathbf{u}}_{n_1}$, $\bar{\mathbf{u}}_{n_2}$. The vectors $\bar{\mathbf{u}}_{n_1}$ and $\bar{\mathbf{u}}_{n_2}$ are the cepstrum estimates at the time instances t_{n_1} and t_{n_2}, respectively. The matrices $\mathbf{U}_{n_1}$, $\mathbf{U}_{n_2}$ and the vectors $\bar{\mathbf{u}}_{n_1}$, $\bar{\mathbf{u}}_{n_2}$ can now be supplied to the Hotelling T^2-test [32, 33].

First, define two matrices

$$\begin{aligned} \mathbf{S}_1 &= \mathbf{U}_{n_1}\mathbf{U}_{n_1}^T - K\bar{\mathbf{u}}_{n_1}\bar{\mathbf{u}}_{n_1}^T \\ \mathbf{S}_2 &= \mathbf{U}_{n_2}\mathbf{U}_{n_2}^T - K\bar{\mathbf{u}}_{n_2}\bar{\mathbf{u}}_{n_2}^T \end{aligned} \tag{2.15}$$

where K is the number of segments (see ***Step 1*** of the algorithm above) and the operator $\{\cdot\}^T$ denotes transposition. It is known [32] that the statistic $\varphi(\mathbf{S}_1, \mathbf{S}_2, \bar{\mathbf{u}}_{n_1}, \bar{\mathbf{u}}_{n_2})$ given by

$$\varphi(\mathbf{S}_1, \mathbf{S}_2, \bar{\mathbf{u}}_{n_1}, \bar{\mathbf{u}}_{n_2}) = \frac{K(2K - M_s - 1)}{2M_s} (\bar{\mathbf{u}}_{n_1} - \bar{\mathbf{u}}_{n_2})^T (\mathbf{S}_1 + \mathbf{S}_2)^{-1} (\bar{\mathbf{u}}_{n_1} - \bar{\mathbf{u}}_{n_2}) \tag{2.16}$$

follows the F-distribution, i.e., $\varphi(\mathbf{S}_1, \mathbf{S}_2, \bar{\mathbf{u}}_{n_1}, \bar{\mathbf{u}}_{n_2}) \sim \mathrm{F}(M_s, 2K - M_s - 1)$.

Thus, the null hypothesis $\mathcal{H}_0$ in (2.8) is accepted if

$$\varphi(\mathbf{S}_1, \mathbf{S}_2, \bar{\mathbf{u}}_{n_1}, \bar{\mathbf{u}}_{n_2}) < f_\alpha \tag{2.17}$$

where f_α is the critical value corresponding to the $100(1-\alpha)\%$ confidence level.

2.2.2 Stationarity Test for MIMO Channels

We consider a MIMO wireless channel with N_T transmitting and N_R receiving antennas. Each of the $N_T N_R$ subchannels establishing the communication links between each transmitting and each receiving antennas, is represented by the measured TVFR channel matrix $\mathbf{H}_i$, $i = 1, \ldots, N_T N_R$, defined in (2.1). As in the previous subsection, the elements $H_i[m, n]$ of the channel matrices $\mathbf{H}_i$ are assumed to be complex random variables. Furthermore, it is assumed that at every time instance t_n, the TVFRs of all the subchannels are jointly WSS processes w.r.t. frequency.

The delay cross power spectral densities (CPSDs) at time t_n is defined as

$$\begin{aligned} P_{H_i,H_{i'}}(\tau', t_n) &= \triangle f' \sum_{\kappa=-\infty}^{\infty} r_{f'_{H_i,H_{i'}}}[\kappa, n] e^{-j2\pi\tau'\kappa\triangle f'}, \\ & \quad i, i' = 1, \ldots, N_T N_R \end{aligned} \tag{2.18}$$

where $r_{f'_{H_i,H_{i'}}}[\kappa, n]$ is the frequency cross-correlation function (FCCF) at time t_n between the TVFR $\mathbf{H}_i$ of the i-th subchannel and the TVFR $\mathbf{H}_{i'}$ of the i'-th subchannel given by

$$\begin{aligned} r_{f'_{H_i,H_{i'}}}[\kappa, n] &= \langle H_i[m, n] H^*_{i'}[m + \kappa, n] \rangle_{f'}, \\ & \quad i, i' = 1, \ldots, N_T N_R. \end{aligned} \tag{2.19}$$

The wide-sense stationarity of the considered MIMO channel w.r.t. time requires that the delay CPSDs $P_{H_i,H_{i'}}(\tau', t_n)$, $i, i' = 1, \ldots, N_T N_R$, are time invariant. Therefore, the null hypothesis $\mathcal{H}_0$ can be expressed as

$$\begin{aligned} \mathcal{H}_0 \; : \; & \big(P_{H_i,H_{i'}}(\tau', t_{n_1}) - P_{H_i,H_{i'}}(\tau', t_{n_2})\big) = 0, \\ & i, i' = 1, \ldots, N_T N_R \text{ and } t_{n_1} \neq t_{n_2}. \end{aligned} \tag{2.20}$$

The objective here is to validate the null hypothesis $\mathcal{H}_0$ by using the procedure developed in the previous subsection for SISO wireless channels.

In [34, Chapter 15], the author describes an interesting approach to estimating CPSDs. It is mentioned, however, that this approach cannot guarantee the magnitude squared coherence [34] between two subchannels to be always bounded

by 1. As we are interested in the time variation of the estimated delay CPSD and not in the estimated coherence between the subchannels, this drawback is not relevant for our purpose.

Following [34], the real and the imaginary parts of the delay CPSDs $P_{H_i,H_{i'}}(\tau', t_n)$ can be written as

$$\begin{aligned} \Re\{P_{H_i,H_{i'}}(\tau', t_n)\} &= \frac{1}{2}(P_{Z_{ii'},Z_{ii'}}(\tau', t_n) - P_{H_i,H_i}(\tau', t_n) - P_{H_{i'},H_{i'}}(\tau', t_n)) \\ \Im\{P_{H_i,H_{i'}}(\tau', t_n)\} &= \frac{1}{2}(P_{W_{ii'},W_{ii'}}(\tau', t_n) - P_{H_i,H_i}(\tau', t_n) - P_{H_{i'},H_{i'}}(\tau', t_n)) \end{aligned} \tag{2.21}$$

for $i, i' = 1, \ldots, N_T N_R$ and $i \neq i'$, where $P_{Z_{ii'},Z_{ii'}}(\tau', t_n)$ and $P_{W_{ii'},W_{ii'}}(\tau', t_n)$ denote, respectively, the delay PSDs of the signals

$$\begin{aligned} Z_{ii'}[m,n] &= H_i[m,n] + H_{i'}[m,n] \\ W_{ii'}[m,n] &= H_i[m,n] + jH_{i'}[m,n]. \end{aligned} \tag{2.22}$$

Taking (2.21) into account, the null hypothesis $\mathcal{H}_0$ in (2.20) can be reformulated as follows

$$\begin{aligned} \mathcal{H}_{0a} &: \big(P_{H_i,H_i}(\tau', t_{n_1}) - P_{H_i,H_i}(\tau', t_{n_2})\big) = 0, \\ &\quad i = 1, \ldots, N_T N_R \text{ and } t_{n_1} \neq t_{n_2} \\ \mathcal{H}_{0b} &: \big(P_{Z_{ii'},Z_{ii'}}(\tau', t_{n_1}) - P_{Z_{ii'},Z_{ii'}}(\tau', t_{n_2})\big) = 0, \\ &\quad i, i' = 1, \ldots, N_T N_R, i \neq i' \text{ and } t_{n_1} \neq t_{n_2} \\ \mathcal{H}_{0c} &: \big(P_{W_{ii'},W_{ii'}}(\tau', t_{n_1}) - P_{W_{ii'},W_{ii'}}(\tau', t_{n_2})\big) = 0, \\ &\quad i, i' = 1, \ldots, N_T N_R, i \neq i' \text{ and } t_{n_1} \neq t_{n_2}. \end{aligned} \tag{2.23}$$

Note the absence of the delay CPSDs in (2.23). Thus, the null hypotheses $\{\{\mathcal{H}_{0a}\}, \{\mathcal{H}_{0b}\}, \{\mathcal{H}_{0c}\}\}$ can be verified by using the method described in Subsection 2.2.1 for SISO channels.

The total number of the null hypotheses in (2.23) is equal to $(N_T N_R)^2$. Based on the results of testing these hypotheses, the decision is to be taken on whether a MIMO channel is WSS. One approach is to accept the wide-sense stationarity of a MIMO channel only if all of the hypotheses $\{\{\mathcal{H}_{0a}\}, \{\mathcal{H}_{0b}\}, \{\mathcal{H}_{0c}\}\}$ have been validated. The probability of the Type I error, i.e., erroneously rejecting any of the hypotheses $\{\{\mathcal{H}_{0a}\}, \{\mathcal{H}_{0b}\}, \{\mathcal{H}_{0c}\}\}$, is equal to α (see (2.17)). Thus, assuming the independence of such errors, the probability of falsely rejecting the hypothesis that a MIMO channel is WSS can be expressed as

$$\Pr\{\text{error}\} = 1 - (1 - \alpha)^{(N_T N_R)^2}. \tag{2.24}$$

As it follows from Table 2.1, even for MIMO channels of moderate dimensions, the probability of error Pr{error} is unacceptable. A possible solution to this problem is to allow a certain number of hypotheses in (2.23) to be rejected. For example, suppose the stationarity of a 2×2 MIMO channel is verified. The probability of error in a single hypothesis test α is set to 0.01. The goal is to maintain Pr{error} equal to or less than α for the decision based on the results of $(N_T N_R)^2 = 16$ hypothesis tests. Using the Bernoulli trials scheme [28], it can be easily shown that in this case Pr{error} ≤ 0.01 if at least 1 of 16 hypotheses in (2.23) is allowed to be rejected.

Table 2.1: Probability Pr{error} of a wrong rejection of the hypothesis that a MIMO channel of dimensions $N_T \times N_R$ is WSS

$N_T \times N_R$	$\alpha = 0,05$	$\alpha = 0.01$	$\alpha = 0.003$
2×2	0.36	0.14	0.047
3×3	0.984	0.557	0.216
4×4	0.9998	0.924	0.537

Let us now reconsider the assumption of the wide-sense stationarity of the channel TVFR w.r.t. frequency. What can be said if this assumption is not valid? As it is described in Subsection 2.2.1, the Hotelling T^2-test verifies the hypothesis that the two column vectors $\bar{\mathbf{u}}_{n_1}$ and $\bar{\mathbf{u}}_{n_2}$ are equal. If the WSS assumption of the TVFR in the frequency domain is not valid, then the vectors $\bar{\mathbf{u}}_{n_1}$ and $\bar{\mathbf{u}}_{n_2}$ are derived from the inconsistent estimates of the delay PSDs. Thus, the null hypotheses formulated in (2.8) and (2.23) cannot be verified, i.e., nothing can be said about WSS property of the channel TVFR w.r.t. time.

However, it is plausible to assume that if the geographical locations of the scatterers, transmitter, and receiver remain unchanged between the time instances t_{n_1} and t_{n_2}, then the vectors $\bar{\mathbf{u}}_{n_1}$ and $\bar{\mathbf{u}}_{n_2}$ are equal. In this case, the tests developed above verify the empirical channel stationarity as defined in [18].

2.3 Performance Evaluation

The performance of the proposed stationarity test has been evaluated based on synthetic TVFRs generated using the geometrical two-ring channel simulation model (see e.g., [35]). Some of the channel simulator parameters are specified below:

- Carrier frequency: 5.255 GHz;
- Bandwidth: $B = 100$ MHz;
- Receiving antenna: uniform linear array;
- Transmitting antenna: uniform linear array;

- Antenna element spacing at the receiver: 0.5λ;
- Antenna element spacing at the transmitter: 0.5λ;
- Interval between the frequencies: $\triangle f' = 1.957 \cdot 10^5$ Hz;
- Time between channel snapshots: $\triangle t = 0.02$ s;
- Maximum Doppler frequency: 22 Hz;
- SNR: 10 dB.

A hundred scatterers are located on the rings around the base station (BS) and the MS (see also Chapter 5). It has been verified that the Doppler frequencies and the propagation delays are different for all propagation paths. Under this condition the generated TVFR is ergodic w.r.t. time and frequency [11]. All the propagation path gains are equal to $1/\sqrt{100}$. The parameters of the channel simulator do not change with time. It has been observed that for the confidence level of 99% ($\alpha = 0.01$) and the parameter $M_s = 16$, the error probability Pr{error} is equal to 0.0073, 0.0145, and 0.0064 for SISO, 2×2 MIMO, and 4×4 MIMO channels, respectively. Evidently, the resulting error probabilities are close to the target value of 0.01.

Analysis of the test sensitivity based on the simulated channel TVFRs reveals that the maximum Doppler frequency does not significantly influence the performance of the test procedure. On the other hand, a non-Gaussianity of the TVFRs (as in the case of a small number of scatterers, e.g., below 20, in the simulation setup described above) demonstrates a strong impact on the error probability Pr{error}. Such impact can be reduced by increasing the segment length M_s.

2.4 Applications to Measurement Data

In this section, we present the results of applying the test procedure developed in Section 2.2 to real-world measurement data. The measurement campaign has been conducted by Telenor R&D, Norway. The description of the measurement sites as well as the measurement equipment can be found in Appendix A.

The antenna arrays at the transmitter and the receiver allow us to investigate the distribution of the stationarity interval lengths for SISO and MIMO channels. For the measurements considered below, the parameter M_s (see Subsection 2.2.1) is equal to 16. The confidence level is set to 99% ($\alpha = 0.01$).

2.4.1 Micro Cell Site – Regular Street Geometry

The first propagation environment corresponds to an urban micro-cell site with a regular street grid. A series of the measured impulse responses for this propagation

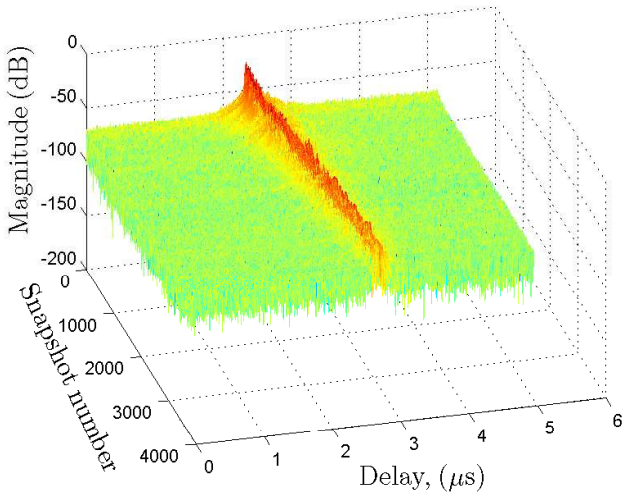

Figure 2.1: Magnitude of the impulse response (micro cell site – regular street geometry).

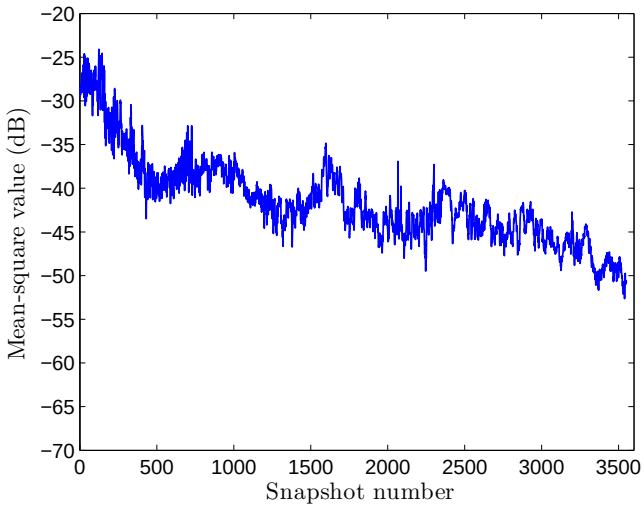

Figure 2.2: Mean-square value of the TVFR (micro cell site – regular street geometry).

scenario is shown in Fig. 2.1. The trend existing in the time variation of the mean-square value of the TVFR can be observed in Fig. 2.2.

In Fig. 2.3, the P-value in the Hotelling T^2-test is shown for the SISO channel. The P-value is the probability that the statistic $\varphi(\mathbf{S}_1, \mathbf{S}_2, \bar{\mathbf{u}}_{n_1}, \bar{\mathbf{u}}_{n_2})$, defined in (2.16), would take a value greater than the observed one $\hat{\varphi}(\mathbf{S}_1, \mathbf{S}_2, \bar{\mathbf{u}}_{n_1}, \bar{\mathbf{u}}_{n_2})$, under condition the null hypothesis $\mathcal{H}_0$ (2.8) is true [36]. The significance value $\alpha = 0.01$ is also depicted in Fig. 2.3.

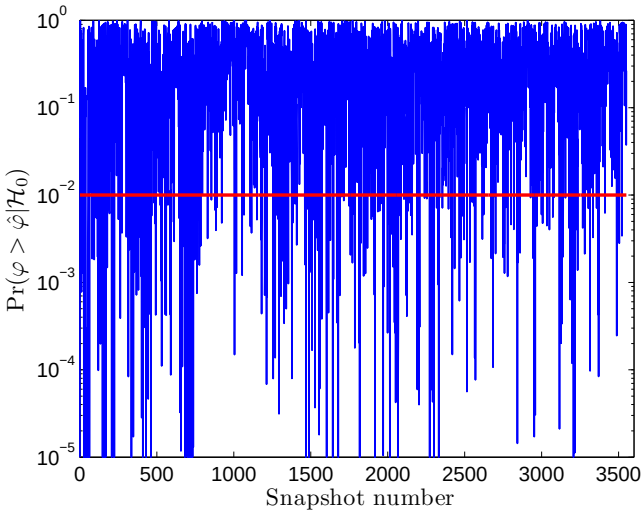

Figure 2.3: P-value in the Hotelling T^2-test for the SISO channel (micro cell site – regular street geometry).

The complementary cumulative distribution functions (CCDFs) of the length of the stationarity intervals[2] obtained for SISO, 2×2 MIMO, and 4×4 MIMO channels are presented in Fig. 2.4. The mean length of the identified stationarity intervals decreases from 0.59 s for the SISO channel to 0.28 s for the 2×2 MIMO and to 0.18 s for 4×4 MIMO channels. The standard deviations of the interval lengths are equal to 0.79 s, 0.34 s, and 0.21 s, for the SISO, 2×2 MIMO, and 4×4 MIMO channels, respectively. Also, the percentage of the identified stationarity intervals longer or equal than for example 0.5 s drops from 40% for the SISO channel to 20% for the 2×2 MIMO and 10% for 4×4 MIMO channels.

[2]Since the moving speed is known only approximately, the stationarity intervals are measured in seconds and not in wavelengths, which otherwise might be a preferable measure.

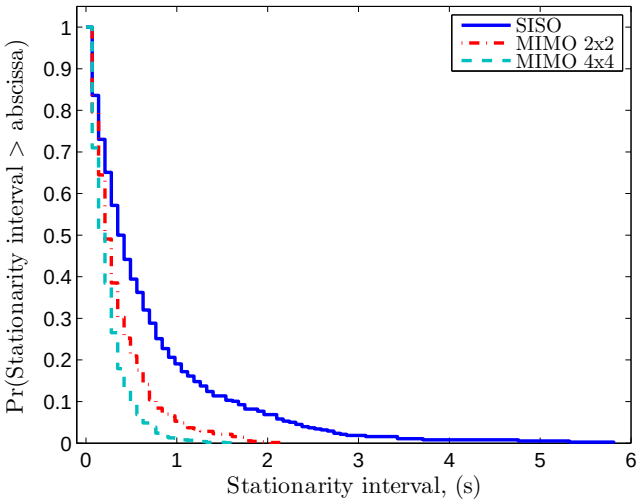

Figure 2.4: CCDF of the length of the stationarity intervals (micro cell site – regular street geometry).

2.4.2 Micro Cell Site – Open Market Place

The second propagation environment corresponds to a town market square.

The measured impulse responses and the graph of the TVFR mean-square value are demonstrated in Figs. 2.5 and 2.6, respectively.

The P-value in the Hotelling T^2-test for the SISO channel is shown in Fig. 2.7.

The CCDFs of the length of the stationarity intervals for the SISO, 2×2 MIMO, and 4×4 MIMO channels are depicted in Fig. 2.8. The average length of the identified stationarity intervals decreases from 0.51 s for the SISO channel to 0.25 s for the 2×2 MIMO and 0.14 s for 4×4 MIMO channels, while the standard deviations of the interval lengths are equal to 0.64 s, 0.25 s, and 0.14 s, respectively. Note that similar to the previously considered propagation environment, the number and the length of the stationarity intervals decrease as the number of antennas at the receiver and transmitter increases. The percentage of the identified stationarity intervals longer or equal than 0.5 s is equal to 36% for the SISO channel, 15% for the 2×2 MIMO channel, and 4% for the 4×4 MIMO channel.

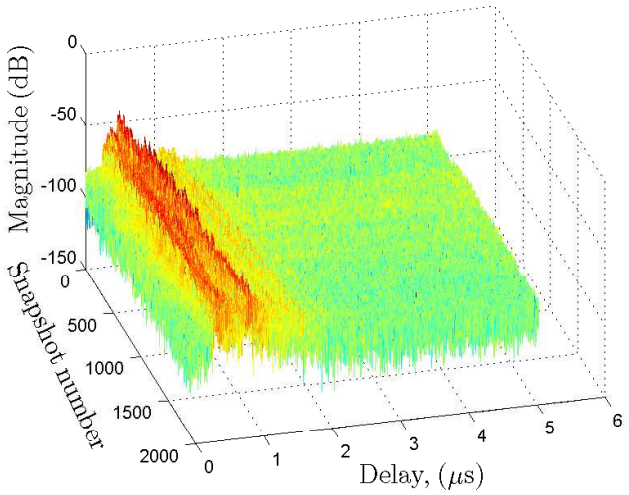

Figure 2.5: Magnitude of the impulse response (micro cell site – open market place).

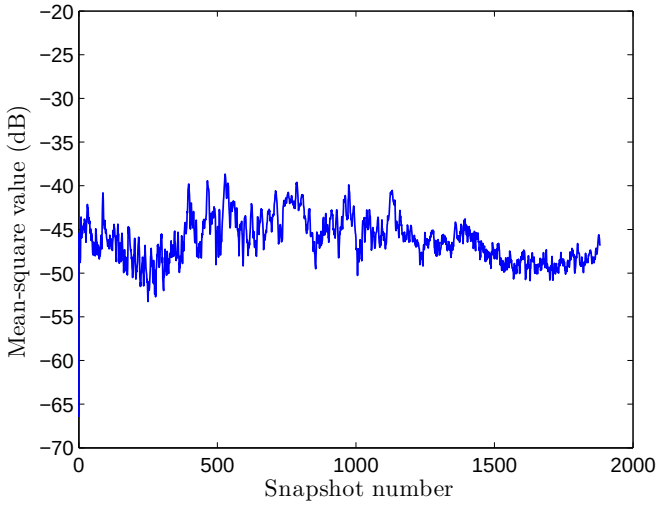

Figure 2.6: Mean-square value of the TVFR (micro cell site – open market place).

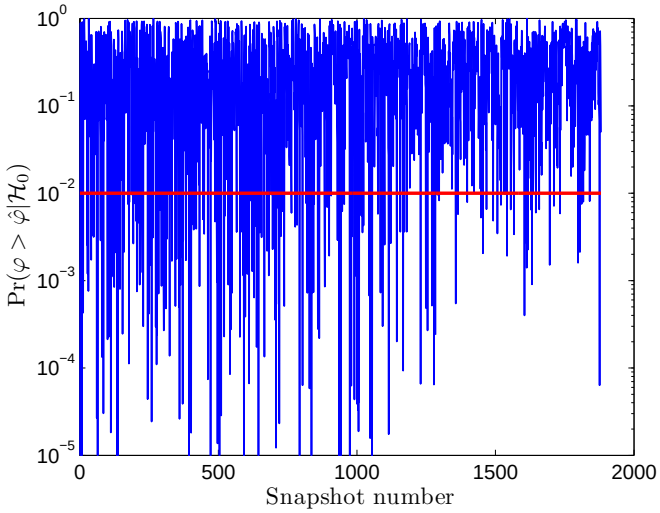

Figure 2.7: P-value in the Hotelling T^2-test for the SISO channel (micro cell site – open market place).

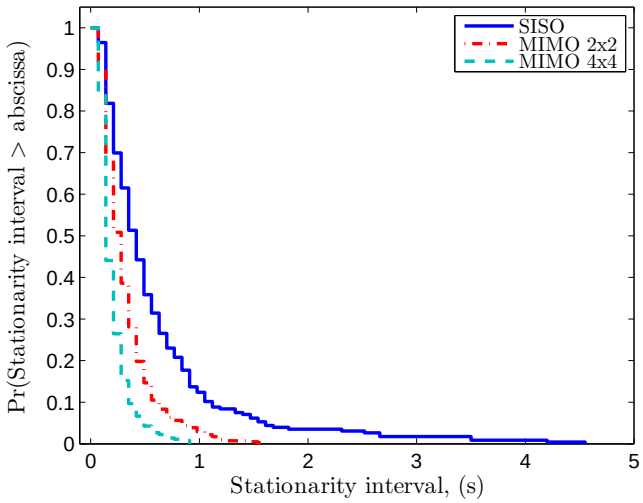

Figure 2.8: CCDF of the length of the stationarity intervals (micro cell site – open market place).

2.4.3 Micro/Pico Cell Site – Passageway

The measurement data has been collected in a passageway connecting the market square, mentioned in the previous subsection, with a side street (see Appendix A).

A series of the impulse responses of the measured channel is depicted in Fig. 2.9. The mean-square value of the TVFR of the measured channel is demonstrated in Fig. 2.10.

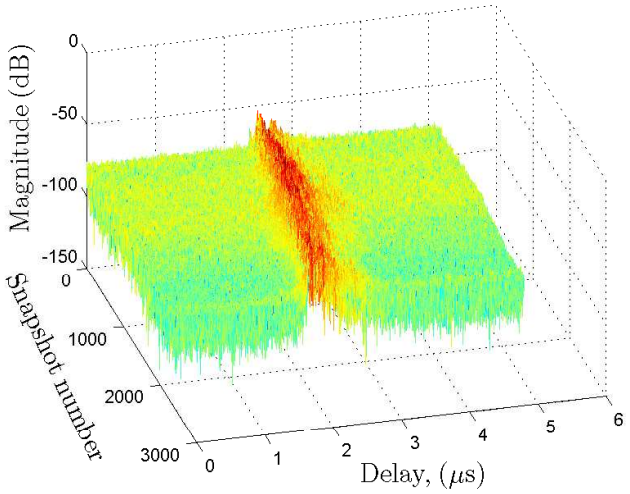

Figure 2.9: Magnitude of the impulse response (micro/pico cell site – passageway).

The P-value for the SISO channel and the empirical CCDFs of the length of the stationarity intervals for the SISO, 2×2 MIMO, and 4×4 MIMO channels are shown in Figs. 2.11 and 2.12, respectively. The means and the standard deviations of the length of identified stationarity intervals are equal to 0.61 s and 0.79 s for the SISO channel, 0.29 s and 0.31 s for the 2×2 MIMO channel, 0.13 s and 0.17 s for the 4×4 MIMO channel. The percentage of the identified stationarity intervals longer or equal than 0.5 s is equal to 39% for the SISO channel, 23% for the 2×2 MIMO channel, and 4% for 4×4 MIMO channel.

Note again that the number and the length of the stationarity intervals decrease as the number of antennas at the receiver and transmitter increases.

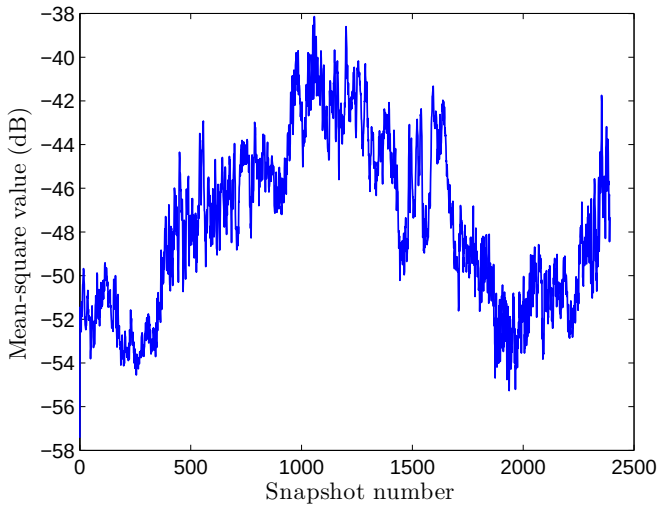

Figure 2.10: Mean-square value of the TVFR (micro/pico cell site – passageway).

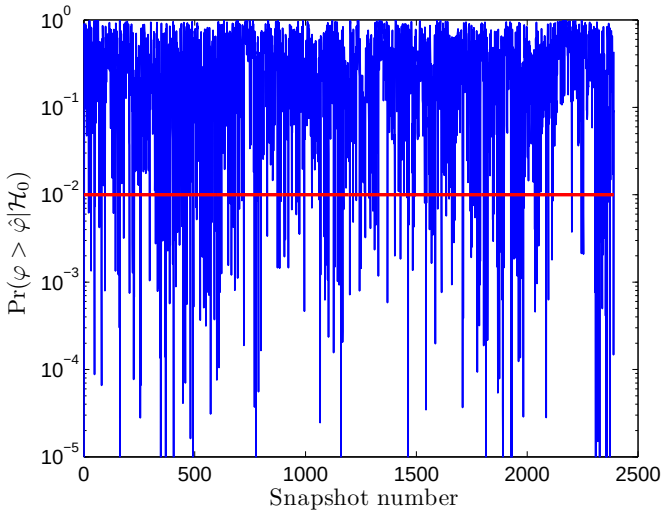

Figure 2.11: P-value in the Hotelling T^2-test for the SISO channel (micro/pico cell site – passageway).

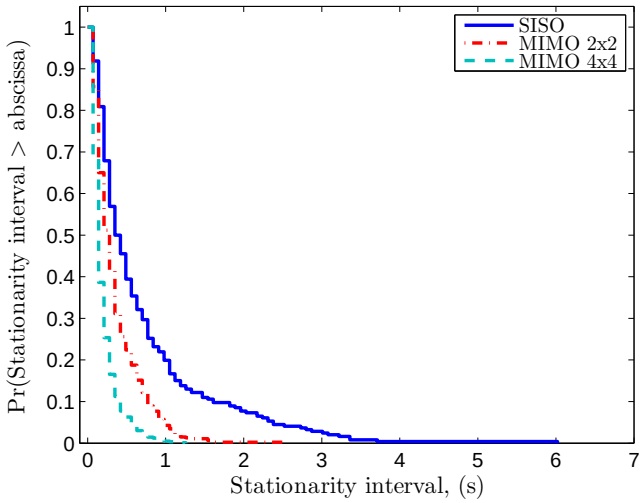

Figure 2.12: CCDF of the length of the stationarity intervals (micro/pico cell site – passageway).

2.4.4 Indoor Cell Site

The stationarity test outlined in Section 2.2 has been applied to a measured indoor wireless channel.

The sequence of the impulse responses and the graph of the mean-square value of the TVFR are shown in Figs. 2.13 and 2.14, respectively. As it follows from 2.14, the variability of the measured TVFR in time is significantly smaller compared to the TVFRs of the channels analyzed above. This observation is supported by the results presented in Figs. 2.15 and 2.16 for the P-value in the Hotelling T^2-test for the SISO channel and the empirical CCDFs of the length of the stationarity intervals for the SISO, 2×2 MIMO, and 4×4 MIMO channels. A possible explanation to the reduced variability of the measured TVFR is the absence of the moving objects along the measurement route. For this channel, the percentage of the identified stationarity intervals longer or equal than 0.5 s is equal to 56% for the SISO channel, 45% for the 2×2 MIMO channel, and 32% for the 4×4 MIMO channel. The mean lengths of the stationarity intervals and the standard deviations are equal , respectively, to 1 s and 1.51 s for the SISO channel, 0.77 s and 1.31 s for the 2×2 MIMO channel, 0.47 s and 0.76 s for the 4×4 MIMO channel. As for all previously considered channels, we note that the number and the length of the stationarity intervals decrease for this environment as the number of antennas at the receiver and transmitter increases.

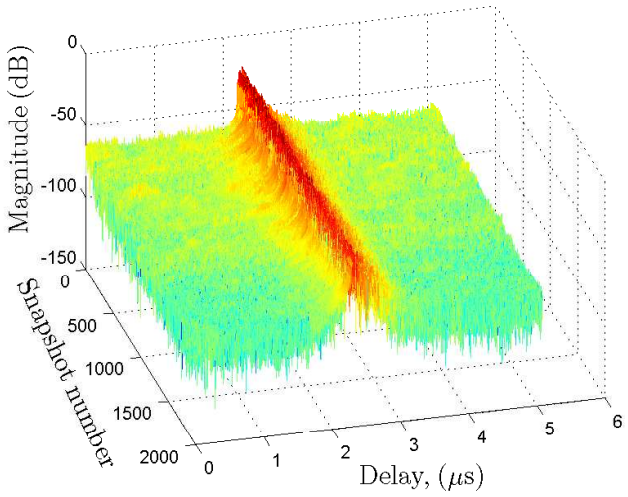

Figure 2.13: Magnitude of the impulse response (indoor cell site).

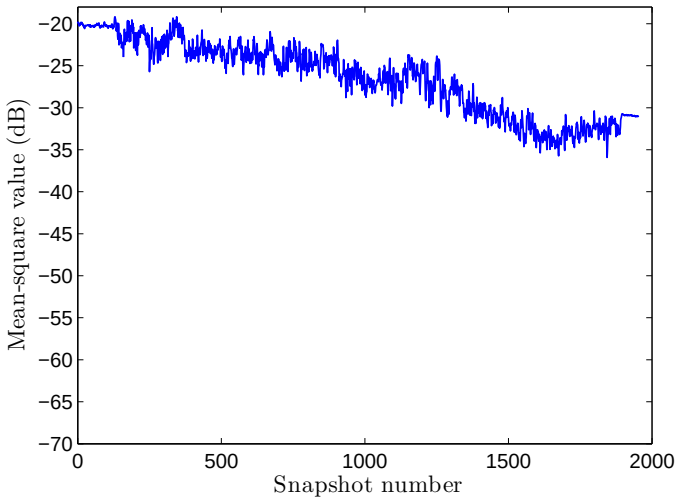

Figure 2.14: Mean-square value of the TVFR (indoor cell site).

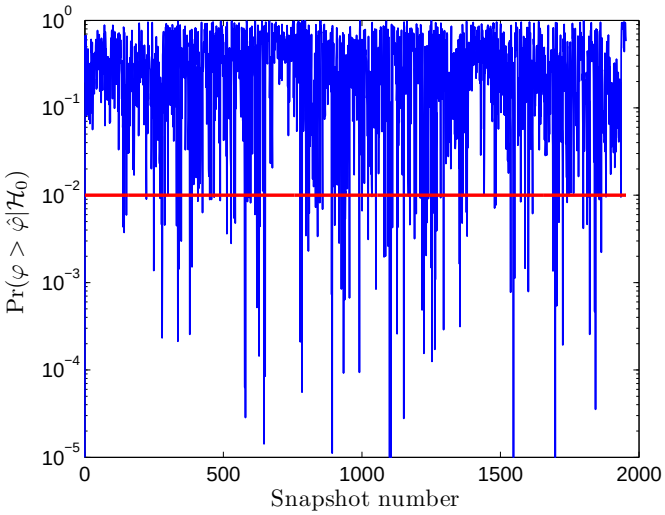

Figure 2.15: P-value in the Hotelling T^2-test for the SISO channel (indoor cell site).

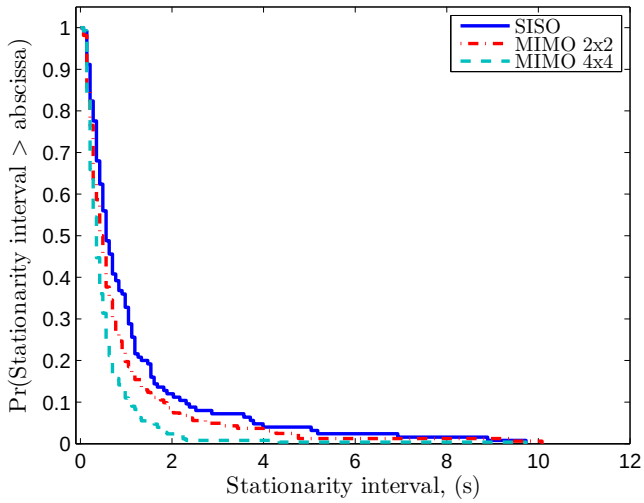

Figure 2.16: CCDF of the length of the stationarity intervals (indoor cell site).

2.5 Chapter Summary

In this chapter, we describe a stationarity test for wireless communication channels. The test is based on analyzing the delay PSD estimated at two different time instances. If the changes in the estimated delay PSDs are statistically insignificant, the hypothesis that the channel is stationary during the considered time interval is accepted. The proposed stationarity test has been extended to validate the stationarity of real-world MIMO wireless channels.

In selecting values for the parameters of the test procedure, particularly the confidence level, which has been set in all our experiments to 99%, we have been guided by considering the probability of the Type I error as the primary performance evaluation criterion. The reason for choosing this particular criterion lies in the fact that the risk of erroneous rejection of the null hypothesis for the developed test can be assessed objectively. On the other hand, evaluating the statistical power of the test, i.e., the probability of the Type II error, requires the non-stationary channel TVFRs. On closer inspection it turns out that the non-stationary channel TVFRs can be synthesized in a variety of manners. For example, the changes in the channel delay PSDs can be abrupt and easily identified, while gradual transitions in the delay PSDs make the definition of the channel stationarity interval itself rather difficult and subjective.

The analysis of the TVFRs of wireless channels measured in different propagation environments suggests that the length of the channel stationarity intervals is greatly dependent on the number of antennas at the transmitter and the receiver. Generally, the stationarity intervals are longer and occur more often for SISO communication channels compared to MIMO channels. It appears that the measured TVFR becomes more "sensitive" to the changes in the propagation environment as the number of antennas at the transmitter and receiver increases.

In the following chapters, we use the stationarity test procedure presented above to identify the intervals, over which the TVFRs of the real-world wireless can be assumed WSS.

Chapter 3

Design of Measurement-Based Stochastic Channel Simulators

3.1 Introduction

Correlation-based models are widely used for simulating wireless channels (see, e.g., [37–39]). In the simplest form these models describe only the spatial correlation properties of MIMO channels. In [40,41], the so-called Kronecker model has been combined with the tap-delay line model to represent wideband MIMO channels. Recently, a structured model, based on the eigenvalue decomposition of the channel correlation matrix, has been proposed in [42] for wideband MIMO channels. A correlation-based model for wideband MIMO Rayleigh fading channels with selectivity in space, time, and frequency has been described in [43,44]. Simulation techniques based on the orthogonal decomposition of the channel impulse response are presented in [45,46].

In this chapter, we describe a method for designing measurement-based stochastic simulation models for time-variant wireless channels [47]. The method has been developed based partly on the results published in [48–50]. The distinctive feature of the proposed design method is the capability of generating realizations of the channel TVFRs with the spatial, temporal, and frequency correlation characteristics closely approximating those of a real-world prototype channel. Note that the separability of the correlation properties in time, frequency, and space (see [16,51]) is not presumed. The usefulness of the method is illustrated by designing several stochastic channel simulators based on the TVFRs of real-world channels measured in different propagation environments.

This chapter is organized as follows. In Section 3.2, the stochastic simulation model is described for MIMO wideband channels. The problem of designing measurement-based MIMO wideband channel simulators is formulated in Section 3.3. The algorithm proposed for determining the parameters of MIMO wide-

band channel simulators is presented in Section 3.4. In Section 3.5, we validate the correctness of the parameter calculation algorithm by simulations. Examples illustrating the development of stochastic channel simulators based on real-world wideband MIMO channels are presented in Section 3.6. In Sections 3.7 and 3.8, we consider the design of stochastic simulators for MIMO narrowband channels and SISO wideband channels, respectively. The concluding remarks are given in Section 3.9.

3.2 A Stochastic Channel Simulation Model for MIMO Wideband Channels

In this section, we describe a stochastic simulation model for MIMO wideband radio channels. It is presumed that the transmitter and the receiver are equipped with N_T and N_R antennas, respectively.

3.2.1 Time-Variant Frequency Response

The simulated TVFR of a MIMO wideband wireless channel at the discrete frequencies $f'_m = -B/2 + m\triangle f' \in [-B/2, B/2]$, $m = 0, \ldots, M-1$, and at the discrete time instances $t_n = n\triangle t \in [0, T]$, $n = 0, \ldots, N-1$, is represented by the matrix sequence

$$\mathbf{H}[m,n] = \begin{pmatrix} H_{1,1}[m,n] & \ldots & H_{1,N_R}[m,n] \\ \vdots & \ddots & \vdots \\ H_{N_T,1}[m,n] & \ldots & H_{N_T,N_R}[m,n] \end{pmatrix} \tag{3.1}$$

where each element $H_{i_1,i_2}[m,n]$, $i_1 = 1, \ldots, N_T$ and $i_2 = 1, \ldots, N_R$, is a sampled TVFR of the subchannel between the i_1-th transmitting antenna and the i_2-th receiving antenna. The parameters B and T denote the frequency bandwidth and the observation time interval, respectively. In the vectorized form, the TVFR $\mathbf{H}[m,n]$ is given by

$$\mathbf{h}[m,n] = vec(\mathbf{H}[m,n]) = \begin{pmatrix} H_{1,1}[m,n] \\ H_{2,1}[m,n] \\ \vdots \\ H_{N_T,N_R}[m,n] \end{pmatrix}. \tag{3.2}$$

Before we proceed with describing the stochastic simulation model for MIMO wideband radio channels, it makes sense to sketch the line of reasoning behind the chosen modeling approach. For this purpose, we consider a general discrete-time WSS zero-mean complex random process $y(t_n)$, $t_n \in [0, T]$. The canonical

decomposition of the random process $y(t_n)$ is given by [52]

$$y(t_n) = \sum_l U_l \varphi_l(t_n) \tag{3.3}$$

where U_l are uncorrelated zero-mean complex random variables and $\varphi_l(t_n)$ are deterministic basis functions.

For the complex random process $y(t_n)$, represented by (3.3), the canonical decomposition of the correlation function $\Upsilon(t_n, t_q) = E\{y(t_n)y^*(t_q)\}$ is expressed as

$$\Upsilon(t_n, t_q) = \sum_l \sigma^2_{U_l} \varphi_l(t_n)\varphi^*_l(t_q) \tag{3.4}$$

where $\sigma^2_{U_l}$ denotes the variance of the random variable U_l.

It is well-known that the optimal choice of the basis functions $\varphi_l(t_n)$ is dictated by the Karhunen-Loève expansion (KLE) [53–55]. The drawback of the KLE is the lack of an analytical solution for the basis functions $\varphi_l(t_n)$, except for a few special cases. As a consequence, it is not possible to generate realizations of the random process $y(t_n)$ at arbitrary chosen time instances.

An alternative approach to selecting the basis functions $\varphi_l(t_n)$ in (3.3) is to employ a generic basis[1], e.g., the Fourier basis. Such 'universality' in representing radio propagation channels is provided by the Maxwellian basis. As postulated in [11, Chapter 4], any wireless channel satisfying the bounded free-space propagation conditions can be represented as a combination of plane waves, which constitute a subset of the Maxwellian basis. It seems reasonable then to choose the functions describing the plane waves as the basis functions for modeling the TVFRs of wireless communication channels.

The simulation model proposed in this chapter for generating realizations of the TVFR $\mathbf{h}[m,n] = [h_1[m,n], \ldots, h_{N_T N_R}]^T$ is based on the stochastic local area channel (SLAC) model [11]. The TVFR of each subchannel $h_i[m,n]$, $i = 1, \ldots, N_T N_R$, is a 2D complex zero-mean random process, represented in the generalized form by the sum (*cf.* (3.3))

$$h_i[m,n] = \sum_{l=1}^{L} U_l \varphi_{i_l}[m,n] \tag{3.5}$$

where $\{U_l\}_1^L$ are independent zero-mean complex random variables and $\{\varphi_{i_l}[m,n]\}_1^L$ are deterministic 2D functions defined as

$$\varphi_{i_l}[m,n] = g_{i_l} e^{j(2\pi f_{d_l} t_n - 2\pi f'_m \tau'_l)}, \quad l = 1, \ldots, L \text{ and } i = 1, \ldots, N_T N_R. \tag{3.6}$$

[1] By qualifying a basis as generic, we mean a broad applicability of the basis for representing signals under mild conditions, which are fulfilled in many practical situations.

Each function $\varphi_{i_l}[m,n]$ describes a homogeneous electromagnetic plane wave. It is characterized by the complex path gain g_{i_l}, the Doppler frequency f_{d_l}, and the propagation delay τ_l'. In contrast to the SLAC model [11], the number of terms in the sum (3.5) is necessarily finite.

As follows from (3.5) and (3.6), the TVFR $\mathbf{h}[m,n]$ is a weighted sum of L complex exponentials[2]

$$\mathbf{h}[m,n] \quad = \quad \sum_{l=1}^{L} c_l \mathbf{g}_l e^{j(2\pi f_{d_l} t_n - 2\pi f_m' \tau_l')} U_l. \tag{3.7}$$

where the vector $\mathbf{g}_l$ is defined as $\mathbf{g}_l = \left[g_{1_l}, \ldots, g_{N_T N_{Rl}}\right]^T$. In the polar coordinate system, the complex weighting coefficients $\{U_l = \Xi_l e^{j\Theta_l}\}_1^L$ are represented by the phase shifts $\{\Theta_l\}_1^L$ and the magnitudes $\{\Xi_l\}_1^L$. The phase shifts $\{\Theta_l\}_1^L$ are independent identically distributed (i.i.d.) random variables, each having a uniform distribution on the interval $[0, 2\pi)$. The magnitudes $\{\Xi_l\}_1^L$ are independent, but not necessarily identically distributed random variables. Moreover, the random variables Ξ_l and Θ_l are statistically independent for all $l = 1, \ldots, L$.

As will be shown in the next subsection, the correlation properties of the channel simulation model in (3.7) in time, frequency, and space are completely described by the set of parameters $\mathcal{P} = \left\{L, \{c_l\}_1^L, \{\mathbf{g}_l\}_1^L, \{f_{d_l}\}_1^L, \{\tau_l'\}_1^L\right\}$. Note that the number of the components L is also considered here (with some abuse of notation) as a model parameter. For a measurement-based stochastic channel simulator, the set of parameters $\mathcal{P}$ is determined from the measured TVFR of a prototype physical wireless channel.

The distributions of the random variables $\{\Xi_l\}_1^L$ can, in principle, be defined arbitrarily, but restricted to having unit variance. For example, when $\{\Xi_l\}_1^L$ are Rayleigh distributed or, equivalently, $U_l \sim \mathcal{CN}(0,1)$ $(l = 1, \ldots, L)$ [28], the TVFR $\mathbf{h}[m,n]$ in (3.7) is a complex Gaussian multivariate 2D random vector process. If the magnitudes $\{\Xi_l\}_1^L$ are constant and all are equal to 1, it can be shown that the envelope PDF $p_{|h_i|}(x)$ of the simulated TVFR $h_i[m,n]$ of the ith subchannel is given by (see [11, p.118])

$$p_{|h_i|}(x) = \int_0^\infty x J_0(x\zeta) \left(\prod_{l=1}^{L} J_0(|c_l g_{i_l}|\zeta) \right) \zeta d\zeta, \quad i = 1, \ldots, N_T N_R \tag{3.8}$$

where $J_0(\cdot)$ denotes the zero-order Bessel function of the first kind. Although the products $\{c_l g_{i_l}\}_1^L$ are in general not equal, it can be expected that the envelope PDF $p_{|h_i|}(x)$ approaches the Rayleigh distribution as $L \to \infty$ due to the central limit theorem.

[2]The reason for keeping the gain factors $\{c_l\}$ as separate parameters will become clear in Section 3.4, where the parameter computation method is considered.

3.2.2 Space-Time-Frequency Correlation Matrix

The correlation between the samples of the simulated TVFR $\mathbf{h}[m,n]$ is characterized by the space-time-frequency correlation matrix $\underline{\mathbf{R}}$ that is defined as

$$\underline{\mathbf{R}} = E\left\{\mathbf{v}[m,n]\mathbf{v}^H[m,n]\right\} =$$

$$\begin{bmatrix}
\mathbf{R}[0,0] & \cdots & \mathbf{R}[-\kappa_{\max},0] & \cdots & \mathbf{R}[0,-\iota_{\max}] & \cdots & \mathbf{R}[-\kappa_{\max},-\iota_{\max}] \\
\vdots & \ddots & \vdots & \ddots & \vdots & \ddots & \vdots \\
\mathbf{R}[\kappa_{\max},0] & \cdots & \mathbf{R}[0,0] & \cdots & \mathbf{R}[\kappa_{\max},-\iota_{\max}] & \cdots & \mathbf{R}[0,-\iota_{\max}] \\
\vdots & \ddots & \vdots & \ddots & \vdots & \ddots & \vdots \\
\mathbf{R}[0,\iota_{\max}] & \cdots & \mathbf{R}[-\kappa_{\max},\iota_{\max}] & \cdots & \mathbf{R}[0,0] & \cdots & \mathbf{R}[-\kappa_{\max},0] \\
\vdots & \ddots & \vdots & \ddots & \vdots & \ddots & \vdots \\
\mathbf{R}[\kappa_{\max},\iota_{\max}] & \cdots & \mathbf{R}[0,\iota_{\max}] & \cdots & \mathbf{R}[\kappa_{\max},0] & \cdots & \mathbf{R}[0,0]
\end{bmatrix} \tag{3.9}$$

where the operator $(\cdot)^H$ stands for a complex conjugate transpose of a matrix and the vector $\mathbf{v}[m,n]$ designates

$$\begin{aligned}
\mathbf{v}[m,n] \;=\; & [\mathbf{h}^T[m,n]\ldots\mathbf{h}^T[m-\kappa_{\max},n] \\
& \ldots\mathbf{h}^T[m,n-\iota_{\max}]\ldots\mathbf{h}^T[m-\kappa_{\max},n-\iota_{\max}]]^T.
\end{aligned} \tag{3.10}$$

After substituting (3.7) into (3.10), the space-time-frequency correlation matrix $\underline{\mathbf{R}}$ of the channel simulation model can be written as

$$\underline{\mathbf{R}} = \sum_{l=1}^{L} c_l^2 \mathbf{R}_{t_l} \otimes \mathbf{R}_{f'_l} \otimes \mathbf{R}_{g_l} \tag{3.11}$$

where the symbol $\otimes$ denotes the Kroneker product. Note that *Kroneker* structure of the correlation matrix $\underline{\mathbf{R}}$ results from absence of any combinations of the space-frequency-time cross-terms in the complex eponentials in (3.7) (*cf.* the conditions for the wave propagation in the local area [11, Chapter 4]). The Toeplitz Hermitian matrices $\mathbf{R}_{t_l}$, $\mathbf{R}_{f'_l}$ and the Hermitian matrix $\mathbf{R}_{g_l}$ are defined as

$$\mathbf{R}_{t_l} = \begin{bmatrix}
1 & \cdots & e^{-j2\pi f_{d_l}\iota_{\max}\triangle t} \\
\vdots & \ddots & \vdots \\
e^{j2\pi f_{d_l}\iota_{\max}\triangle t} & \cdots & 1
\end{bmatrix} \tag{3.12}$$

$$\mathbf{R}_{f'_l} = \begin{bmatrix}
1 & \cdots & e^{j2\pi\tau'_l\kappa_{\max}\triangle f'} \\
\vdots & \ddots & \vdots \\
e^{-j2\pi\tau'_l\kappa_{\max}\triangle f'} & \cdots & 1
\end{bmatrix} \tag{3.13}$$

and

$$\mathbf{R}_{g_l} = \mathbf{g}_l \mathbf{g}_l^H. \tag{3.14}$$

The space-time-frequency correlation matrix $\underline{\mathbf{R}}$ in (3.9) is Hermitian and doubly block-Toeplitz.

For the case of complex weighting coefficients with the constant magnitudes $\{\Xi_l = 1\}_1^L$ in (3.7), it is worth mentioning that the TVFR $\mathbf{h}[m,n]$ is correlation-ergodic w.r.t. time and frequency under the conditions $f_{d_n} \neq f_{d_l}$ and $\tau'_n \neq \tau'_l$ for all $n \neq l$.

3.3 Problem Formulation

As it has been stated in Section 3.2, the set of parameters $\mathcal{P}$ of the stochastic channel simulation model in (3.7) is to be determined from the TVFR of a prototype physical wireless channel. Our aim is to develop an algorithm that allows creating channel simulators with the correlation properties in time, frequency, and space closely approximating the corresponding correlation properties of prototype real-world channels.

Let $\tilde{\mathbf{H}}[m,n]$ denote the TVFR of a real-world wireless $N_T \times N_R$ MIMO channel measured at the discrete frequencies f'_m, $m = 0, \ldots, M-1$, and at the discrete time instances t_n, $n = 0, \ldots, N-1$. The TVFR $\tilde{\mathbf{H}}[m,n]$ in the vectorized form is given by

$$\begin{aligned}\tilde{\mathbf{h}}[m,n] &= \Big[\tilde{h}_1[m,n], \ldots, \tilde{h}_{N_T N_R}[m,n]\Big]^T \\ &= vec(\tilde{\mathbf{H}}[m,n]) = \Big[\tilde{H}_{1,1}[m,n], \ldots, \tilde{H}_{N_T,N_R}[m,n]\Big]^T.\end{aligned} \tag{3.15}$$

The TVFR of each subchannel $\tilde{h}_i[m,n]$, $i = 1, \ldots, N_T N_R$, is assumed to be a 2D zero-mean complex random process. Furthermore, we assume that the TVFR $\tilde{\mathbf{h}}[m,n]$ of a real-world channel is ergodic with respect to time and frequency, therefore, an estimate of the space-time-frequency correlation matrix $\underline{\tilde{\mathbf{R}}}$, defined similar to the correlation matrix $\underline{\mathbf{R}}$ in (3.9), can be obtained from a single realization of the TVFR $\tilde{\mathbf{h}}[m,n]$ by averaging over time and frequency. The estimation of the correlation matrix $\underline{\tilde{\mathbf{R}}}$ is considered in the next section.

The problem of designing a measurement-based stochastic channel simulator can now be formulated as follows:

Given the estimated correlation matrix $\underline{\tilde{\mathbf{R}}}$ of a real-world channel, design a channel simulation model in such a way that the correlation matrix $\underline{\mathbf{R}}$ of the channel simulator approximates closely the estimated correlation matrix $\underline{\tilde{\mathbf{R}}}$.

Taking into account the possible inaccuracy of the model in (3.7), as well

as the errors in the estimated correlation matrix $\underline{\tilde{\mathbf{R}}}$, we suggest using the following design criterion (see also [6, 56]) for determining the set of parameters $\mathcal{P} = \{L, \{c_l\}_1^L, \{\mathbf{g}_l\}_1^L, \{f_{d_l}\}_1^L, \{\tau_l'\}_1^L\}$ of the channel simulation model defined in Section 3.2

$$\hat{\mathcal{P}} = \min_{\mathcal{P}} \left\| \underline{\tilde{\mathbf{R}}} - \underline{\mathbf{R}} \right\|_F \tag{3.16}$$

where the symbol $\|\cdot\|_F$ denotes the Frobenius matrix norm. The Frobenius matrix norm, in this case, plays the role of the Euclidian vector norm in the traditional least-square fitting of a data sequence formulation. After substituting (3.11) into (3.16) we obtain

$$\hat{\mathcal{P}} = \min_{\mathcal{P}} \left\| \underline{\tilde{\mathbf{R}}} - \sum_{l=1}^{L} c_l^2 \mathbf{R}_{t_l} \otimes \mathbf{R}_{f_l'} \otimes \mathbf{R}_{g_l} \right\|_F \tag{3.17}$$

where the matrices $\mathbf{R}_{t_l}$, $\mathbf{R}_{f_l'}$, and $\mathbf{R}_{g_l}$ are defined in (3.12), (3.13), and (3.14), respectively.

In the next section, we develop an iterative algorithm for determining the parameters of the channel simulation model by minimizing the Frobenius norm in (3.17).

3.4 Computation of the Channel Simulator Parameters

3.4.1 Estimation of the Channel Correlation Matrix

By assumption, the measured TVFR $\tilde{\mathbf{h}}[m, n]$ is WSS (ergodic) with respect to time and frequency. Theoretically, this means that the matrix $\underline{\tilde{\mathbf{R}}}$ must be doubly block-Toeplitz[3]. This can hardly be observed in practical situations due to the statistical variations in the correlation matrix, estimated from a limited number of measured data samples.

Therefore, in order to ensure the doubly block-Toeplitz structure of the estimated correlation matrix $\underline{\tilde{\mathbf{R}}}$, we first obtain the estimates of the correlation matrices $\tilde{\mathbf{R}}[\kappa, \iota]$ for $\kappa = -\kappa_{\max}, \ldots, 0, \ldots, \kappa_{\max}$ and
$\iota = -\iota_{\max}, \ldots, 0, \ldots, \iota_{\max}$, as follows

$$\hat{\tilde{\mathbf{R}}}[\kappa, \iota] = \frac{1}{(M - |\kappa|)(N - |\iota|)} \sum_{m=0}^{M-1-|\kappa|} \sum_{n=0}^{N-1-|\iota|} \tilde{\mathbf{h}}[m, n] \tilde{\mathbf{h}}^H[m + \kappa, n + \iota]. \tag{3.18}$$

Note that the correlation matrix estimator (3.18) is unbiased, i.e.,

$E\{\hat{\tilde{\mathbf{R}}}[\kappa, \iota]\} \quad =$

[3]Recall that the TVFR $\tilde{\mathbf{h}}[m, n]$ is measured on the grid of equally distant frequencies $f_m' = -B/2 + m\triangle f'$, $m = 0, \ldots, M-1$, and time instances $t_n = n\triangle t$, $n = 0, \ldots, N-1$.

$$\frac{1}{(M-|\kappa|)(N-|\iota|)}\sum_{m=0}^{M-1-|\kappa|}\sum_{n=0}^{N-1-|\iota|}E\{\tilde{\mathbf{h}}[m,n]\tilde{\mathbf{h}}^H[m+\kappa,n+\iota]\}=\tilde{\mathbf{R}}[\kappa,\iota]. \tag{3.19}$$

Also for the complex random process $\tilde{\mathbf{h}}[m,n]$, which is jointly Gaussian for any set of frequencies f'_m and time instances t_n, it can be shown that the variance of the (i_1,i_2)-th element $\hat{\tilde{\mathbf{R}}}_{i_1,i_2}[\kappa,\iota]$, $i_1,i_2=1,\ldots,N_TN_R$, of the estimated correlation matrix in (3.18), given by

$$E\left\{(\hat{\tilde{\mathbf{R}}}_{i_1,i_2}[\kappa,\iota]-\tilde{\mathbf{R}}_{i_1,i_2}[\kappa,\iota])(\hat{\tilde{\mathbf{R}}}_{i_1i_2}[\kappa,\iota]-\tilde{\mathbf{R}}_{i_1,i_2}[\kappa,\iota])^*\right\}=$$

$$\begin{aligned}
&=\frac{1}{(M-|\kappa|)^2(N-|\iota|)^2}\sum_{m_1=0}^{M-1-|\kappa|}\sum_{n_1=0}^{N-1-|\iota|}\sum_{m_2=0}^{M-1-|\kappa|}\sum_{n_2=0}^{N-1-|\iota|}\\
&\qquad E\left\{\tilde{h}_{i_1}[m_1,n_1]\tilde{h}^*_{i_2}[m_1+\kappa,n_1+\iota]\tilde{h}_{i_2}[m_2+\kappa,n_2+\iota]\tilde{h}^*_{i_1}[m_2,n_2]\right\}\\
&\qquad\qquad -|\tilde{\mathbf{R}}_{i_1,i_2}[\kappa,\iota])|^2=\\
&=\frac{1}{(M-|\kappa|)^2(N-|\iota|)^2}\sum_{m_1=0}^{M-1-|\kappa|}\sum_{n_1=0}^{N-1-|\iota|}\sum_{m_2=0}^{M-1-|\kappa|}\sum_{n_2=0}^{N-1-|\iota|}\\
&\qquad\left[E\left\{\tilde{h}_{i_1}[m_1,n_1]\tilde{h}^*_{i_1}[m_2,n_2]\right\}E\left\{\tilde{h}^*_{i_2}[m_1+\kappa,n_1+\iota]\tilde{h}_{i_2}[m_2+\kappa,n_2+\iota]\right\}+\right.\\
&\qquad\left.E\left\{\tilde{h}_{i_1}[m_1,n_1]\tilde{h}_{i_2}[m_2+\kappa,n_2+\iota]\right\}E\left\{\tilde{h}^*_{i_2}[m_1+\kappa,n_1+\iota]\tilde{h}^*_{i_1}[m_2,n_2]\right\}\right]
\end{aligned} \tag{3.20}$$

asymptotically (as $N\to\infty$, $M\to\infty$) approaches zero under the condition

$$\begin{aligned}
&\sum_{\vartheta=-\infty}^{\infty}\sum_{\varsigma=-\infty}^{\infty}|\vartheta||\varsigma|\left[E\left\{\tilde{h}_{i_1}[m,n]\tilde{h}^*_{i_1}[m+\vartheta,n+\varsigma]\right\}\right.\\
&\quad\times E\left\{\tilde{h}_{i_2}[m,n]\tilde{h}^*_{i_2}[m-\vartheta,n-\varsigma]\right\}+E\left\{\tilde{h}_{i_1}[m,n]\tilde{h}_{i_2}[m+\vartheta+\kappa,n+\varsigma+\iota]\right\}\\
&\qquad\left.\times E\left\{\tilde{h}^*_{i_1}[m,n]\tilde{h}^*_{i_2}[m-\vartheta+\kappa,n-\varsigma+\iota]\right\}\right]<\infty
\end{aligned} \tag{3.21}$$

where we have defined $\vartheta=m_2-m_1$ and $\varsigma=n_2-n_1$. The condition in (3.21) is normally fulfilled in practice.

The estimated correlation matrix $\underline{\hat{\tilde{\mathbf{R}}}}$ is created by combining the estimated matrices $\hat{\tilde{\mathbf{R}}}[\kappa,\iota]$ similar to (3.9). It can be easily checked that the resulting matrix

$\hat{\underline{\mathbf{R}}}$ is Hermitian and doubly block-Toeplitz.

3.4.2 Iterative Parameter Computation Method

Observe that the minimization of the Frobenius norm in (3.17) resembles the problem of finding the optimal (in the Frobenius norm sense) decomposition of the correlation matrix $\hat{\underline{\mathbf{R}}}$ over a library $\mathcal{X}$ of the Hermitian matrices $\mathbf{X} = \mathbf{R}_t \otimes \mathbf{R}_{f'} \otimes \mathbf{R}_g$. Each member $\mathbf{X}_k = \mathbf{R}_{t_k} \otimes \mathbf{R}_{f'_k} \otimes \mathbf{R}_{g_k}$ of the matrix library $\mathcal{X}$ is constructed by substituting a set of the channel simulator parameters $\gamma_k = \{\mathbf{g}_k, f_{d_k}, \tau'_k\} \in \Gamma$ into (3.12)–(3.14). Here, Γ denotes the set of all possible sets γ_k. To find the matrices $\{\mathbf{X}_l\}_1^L$ that minimize the Frobenius norm in (3.17), we adapt the matching pursuit (MP) approach [57] often employed, e.g., for selecting the 'best' wavelet packet basis decomposition of a given signal.

The estimated correlation matrix $\hat{\underline{\mathbf{R}}}$ is decomposed as

$$\hat{\underline{\mathbf{R}}} = \frac{\langle \hat{\underline{\mathbf{R}}}, \mathbf{X}_1 \rangle}{\langle \mathbf{X}_1, \mathbf{X}_1 \rangle} \mathbf{X}_1 + \hat{\underline{\mathbf{R}}}_{res_1} \tag{3.22}$$

where $\langle \mathbf{A}, \mathbf{B} \rangle$ designates the matrix inner product and $\mathbf{X}_1 = \mathbf{R}_{t_1} \otimes \mathbf{R}_{f'_1} \otimes \mathbf{R}_{g_1}$ is a member of the matrix library $\mathcal{X}$ obtained, as mentioned above, by substituting the set of the simulation model parameters $\gamma_1 = \{\mathbf{g}_1, f_{d_1}, \tau'_1\} \in \Gamma$ into (3.12)–(3.14).

The Hermitian matrix $\hat{\underline{\mathbf{R}}}_{res_1}$ represents the residual approximation error. It can be shown that the matrices $\mathbf{X}_1$ and $\hat{\underline{\mathbf{R}}}_{res_1}$ are orthogonal, i.e., $\langle \hat{\underline{\mathbf{R}}}_{res_1}, \mathbf{X}_1 \rangle = 0$, consequently

$$\|\hat{\underline{\mathbf{R}}}\|_F^2 = \frac{|\langle \hat{\underline{\mathbf{R}}}, \mathbf{X}_1 \rangle|^2}{\langle \mathbf{X}_1, \mathbf{X}_1 \rangle} + \|\hat{\underline{\mathbf{R}}}_{res_1}\|_F^2. \tag{3.23}$$

From (3.23), it follows that $\|\hat{\underline{\mathbf{R}}}\|_F \geq \|\hat{\underline{\mathbf{R}}}_{res_1}\|_F$ and the set of parameters $\gamma_1 = \{\mathbf{g}_1, f_{d_1}, \tau'_1\}$, which minimizes the norm of the residual error $\hat{\underline{\mathbf{R}}}_{res_1}$, can be determined as

$$\gamma_1 = \{\mathbf{g}_1, f_{d_1}, \tau'_1\} = \arg \max_{\gamma_k \in \Gamma} \frac{\langle \hat{\underline{\mathbf{R}}}, \mathbf{X}_k \rangle}{\langle \mathbf{X}_k, \mathbf{X}_k \rangle}. \tag{3.24}$$

Also, from the comparison of (3.17) and (3.23), the squared gain factor c_1^2 is given by

$$c_1^2 = \frac{\langle \hat{\underline{\mathbf{R}}}, \mathbf{X}_1 \rangle}{\langle \mathbf{X}_1, \mathbf{X}_1 \rangle}. \tag{3.25}$$

Equation (3.11) implies that the gain factors c_l must be real and nonnegative. Hence, the maximizer in (3.24) has to be supplemented with the constraint $\langle \hat{\underline{\mathbf{R}}}, \mathbf{X}_1 \rangle = |\langle \hat{\underline{\mathbf{R}}}, \mathbf{X}_1 \rangle|$, i.e., the inner product $\langle \hat{\underline{\mathbf{R}}}, \mathbf{X}_1 \rangle$ must be real and greater than or equal to zero.

In turn, the residual error matrix $\hat{\underline{\hat{\mathbf{R}}}}_{res_1}$ is decomposed into the sum

$$\hat{\underline{\hat{\mathbf{R}}}}_{res_1} = \frac{\langle \hat{\underline{\hat{\mathbf{R}}}}_{res_1}, \mathbf{X}_2 \rangle}{\langle \mathbf{X}_2, \mathbf{X}_2 \rangle} \mathbf{X}_2 + \hat{\underline{\hat{\mathbf{R}}}}_{res_2}. \tag{3.26}$$

Again, it can be shown that $\langle \hat{\underline{\hat{\mathbf{R}}}}_{res_2}, \mathbf{X}_2 \rangle = 0$, and consequently

$$\|\hat{\underline{\hat{\mathbf{R}}}}_{res_1}\|_F^2 = \frac{|\langle \hat{\underline{\hat{\mathbf{R}}}}_{res_1}, \mathbf{X}_2 \rangle|^2}{\langle \mathbf{X}_2, \mathbf{X}_2 \rangle} + \|\hat{\underline{\hat{\mathbf{R}}}}_{res_2}\|_F^2 \tag{3.27}$$

where the matrix $\mathbf{X}_2$ is a member of the library $\mathcal{X}$ corresponding to the parameter set $\gamma_2 = \{\mathbf{g}_2, f_{d_2}, \tau_2'\} \in \Gamma$. Similar to (3.24) and (3.25), the parameter set γ_2 is obtained by maximizing $\langle \hat{\underline{\hat{\mathbf{R}}}}_{res_1}, \mathbf{X}_k \rangle / \langle \mathbf{X}_k, \mathbf{X}_k \rangle$ under the constraint $\langle \hat{\underline{\hat{\mathbf{R}}}}_{res_1}, \mathbf{X}_2 \rangle = |\langle \hat{\underline{\hat{\mathbf{R}}}}_{res_1}, \mathbf{X}_2 \rangle|$, and the squared gain factor $c_2^2 = \langle \hat{\underline{\hat{\mathbf{R}}}}_{res_1}, \mathbf{X}_2 \rangle / \langle \mathbf{X}_2, \mathbf{X}_2 \rangle$. Observe that according to (3.27) $\|\hat{\underline{\hat{\mathbf{R}}}}_{res_1}\|_F \geq \|\hat{\underline{\hat{\mathbf{R}}}}_{res_2}\|_F$.

Continuing in a similar way, we obtain the following decomposition of the estimated correlation matrix $\hat{\underline{\hat{\mathbf{R}}}}$

$$\hat{\underline{\hat{\mathbf{R}}}} = \sum_{l=1}^{L} \frac{\langle \hat{\underline{\hat{\mathbf{R}}}}_{res_{l-1}}, \mathbf{X}_l \rangle}{\langle \mathbf{X}_l, \mathbf{X}_l \rangle} \mathbf{X}_l + \hat{\underline{\hat{\mathbf{R}}}}_{res_L} \tag{3.28}$$

where $\hat{\underline{\hat{\mathbf{R}}}}_{res_0} = \hat{\underline{\hat{\mathbf{R}}}}$.

Accordingly, the Fobenius norm in (3.17) is given by

$$\|\hat{\underline{\hat{\mathbf{R}}}} - \sum_{l=1}^{L} \frac{\langle \hat{\underline{\hat{\mathbf{R}}}}_{res_{l-1}}, \mathbf{X}_l \rangle}{\langle \mathbf{X}_l, \mathbf{X}_l \rangle} \mathbf{X}_l\|_F = \|\hat{\underline{\hat{\mathbf{R}}}}_{res_L}\|_F. \tag{3.29}$$

Note that the inequality $\|\hat{\underline{\hat{\mathbf{R}}}}_{res_l}\|_F \geq \|\hat{\underline{\hat{\mathbf{R}}}}_{res_{l+1}}\|_F$ holds true for all $l = 0, \ldots, L-1$.

Let us now assume that the matrices $\{\mathbf{X}_l\}_1^L \in \mathcal{X}$, as well as the corresponding squared gain factors $\{c_l^2 = \langle \hat{\underline{\hat{\mathbf{R}}}}_{res_{l-1}}, \mathbf{X}_l \rangle / \langle \mathbf{X}_l, \mathbf{X}_l \rangle\}_1^L$, have been determined. In order to further reduce the residual approximation error given by (3.29), we want to find the best possible solution to the following maximization problem (see (3.24))

$$\left\{\mathbf{g}_{L+1}, f_{d_{L+1}}, \tau_{L+1}'\right\} = \underset{\mathbf{g}_k, f_{d_k}, \tau_k'}{\arg\max} \frac{\langle \hat{\underline{\hat{\mathbf{R}}}}_{res_L}, \mathbf{X}_k \rangle}{\langle \mathbf{X}_k, \mathbf{X}_k \rangle} \tag{3.30}$$

under the constraint $\langle \hat{\underline{\hat{\mathbf{R}}}}_{res_L}, \mathbf{X}_{L+1} \rangle = |\langle \hat{\underline{\hat{\mathbf{R}}}}_{res_L}, \mathbf{X}_{L+1} \rangle|$.

Using the properties of the Kronecker product and the definitions in (3.12)–

(3.14), any member $\mathbf{X}_k$ of the matrix library $\mathcal{X}$ can be written as

$$\mathbf{X}_k = \mathbf{x}_k \mathbf{x}_k^H = (\mathbf{e}_{t_k} \otimes \mathbf{e}_{f'_k} \otimes \mathbf{g}_k)(\mathbf{e}_{t_k} \otimes \mathbf{e}_{f'_k} \otimes \mathbf{g}_k)^H \tag{3.31}$$

where

$$\begin{aligned} \mathbf{e}_{t_k} &= \left[1 \; e^{j2\pi f_{d_k} \triangle t} \ldots e^{j2\pi f_{d_k} \iota_{\max} \triangle t}\right]^T \\ \mathbf{e}_{f'_k} &= \left[1 \; e^{-j2\pi \tau'_k \triangle f'} \ldots e^{-j2\pi \tau'_k \kappa_{\max} \triangle f'}\right]^T. \end{aligned} \tag{3.32}$$

It follows that the maximizer in (3.30) can be equivalently expressed as

$$\left\{\mathbf{g}_{L+1}, f_{d_{L+1}}, \tau'_{L+1}\right\} = \underset{\mathbf{g}_k, f_{d_k}, \tau'_k}{\arg\max} \frac{\mathbf{x}_k^H \hat{\underline{\mathbf{R}}}_{res_L} \mathbf{x}_k}{\mathbf{x}_k^H \mathbf{x}_k}. \tag{3.33}$$

To reduce the computational difficulties associated with the multidimensional search for the parameters $\left\{\mathbf{g}_{L+1}, f_{d_{L+1}}, \tau'_{L+1}\right\}$ in (3.33), we use the procedure developed below.

The maximum of the Rayleigh quotient in (3.33) is equal to the largest eigenvalue $\lambda_{\max_L}$ of the matrix $\hat{\underline{\mathbf{R}}}_{res_L}$ [58]. This observation suggests an idea to make the vector $\mathbf{x}_{L+1}$ as much as possible collinear with the eigenvector $\mathbf{u}_L$ associated with the eigenvalue $\lambda_{\max_L}$. Thus, the maximization problem in (3.33) can be reformulated as

$$\left\{\mathbf{g}_{L+1}, f_{d_{L+1}}, \tau'_{L+1}\right\} = \underset{\mathbf{g}_k, f_{d_k}, \tau'_k}{\arg\min} \frac{\mathbf{x}_k^H \mathbf{P}_L \mathbf{x}_k}{\mathbf{x}_k^H \mathbf{x}_k} \tag{3.34}$$

where the matrix $\mathbf{P}_L = \mathbf{I} - \mathbf{u}_L \mathbf{u}_L^H$ is the orthogonal projector on the $(N_T N_R(\kappa_{\max}+1)(\iota_{\max}+1)-1)$-dimensional subspace complementary to the subspace spanned by the vector $\mathbf{u}_L$, and $\mathbf{I}$ denotes the unity matrix of appropriate dimensions. In (3.34), the property $\mathbf{P}_L^H \mathbf{P}_L = \mathbf{P}_L$ has been used.

On substituting $\mathbf{x}_k = \mathbf{e}_{t_k} \otimes \mathbf{e}_{f'_k} \otimes \mathbf{g}_k$ into (3.34), we obtain[4]

$$\left\{\mathbf{g}_{L+1}, f_{d_{L+1}}, \tau'_{L+1}\right\} = \underset{\mathbf{g}_k, f_{d_k}, \tau'_k}{\arg\min} \frac{\langle \mathbf{R}_{f'_k} \otimes \mathbf{R}_{g_k}, \mathbf{P'}_{L_k} \rangle}{(\mathbf{e}_{t_k}^H \mathbf{e}_{t_k})(\mathbf{e}_{f'_k}^H \mathbf{e}_{f'_k})(\mathbf{g}_k^H \mathbf{g}_k)} \tag{3.35}$$

where the matrix $\mathbf{P'}_{L_k}$ is defined as

$$\mathbf{P'}_{L_k} = (\mathbf{e}_{t_k}^H \otimes \mathbf{I}) \mathbf{P}_L (\mathbf{e}_{t_k} \otimes \mathbf{I}). \tag{3.36}$$

[4]Recall that for any square matrix $\mathbf{A}$ and a vector $\mathbf{b}$, the following equalities hold $\mathbf{b}^H \mathbf{A} \mathbf{b} = trace\{\mathbf{b}\mathbf{b}^H \mathbf{A}\} = \langle \mathbf{b}\mathbf{b}^H, \mathbf{A} \rangle$.

The Couchy-Bunyakovsky-Schwarz (CBS) inequality allows us to write

$$|\langle \mathbf{R}_{f'_k} \otimes \mathbf{R}_{g_k}, \mathbf{P'}_{L_k} \rangle| \leq \|\mathbf{R}_{f'_k} \otimes \mathbf{R}_{g_k}\|_F \|\mathbf{P'}_{L_k}\|_F. \tag{3.37}$$

Thus, as a solution to (3.35), we use the Doppler frequency $f_{d_{L+1}}$ determined as

$$f_{d_{L+1}} = \arg\min_{f_{d_k}} \frac{\|\mathbf{P'}_{L_k}\|_F}{\mathbf{e}_{t_k}^H \mathbf{e}_{t_k}}. \tag{3.38}$$

After substituting the Doppler frequency $f_{d_{L+1}}$ that minimizes (3.38) into (3.36), the channel simulator parameters $\{\mathbf{g}_{L+1}, \tau'_{L+1}\}$ are found from the following equation

$$\{\mathbf{g}_{L+1}, \tau'_{L+1}\} = \arg\min_{\mathbf{g}_k, \tau'_k} \frac{\langle \mathbf{R}_{g_k}, \mathbf{P''}_{L_k} \rangle}{(\mathbf{e}_{f'_k}^H \mathbf{e}_{f'_k})(\mathbf{g}_k^H \mathbf{g}_k)} \tag{3.39}$$

where the matrix $\mathbf{P''}_{L_k}$ is defined as

$$\mathbf{P''}_{L_k} = (\mathbf{e}_{f'_k}^H \otimes \mathbf{I}) \mathbf{P'}_L (\mathbf{e}_{f'_k} \otimes \mathbf{I}). \tag{3.40}$$

Application of the CBS inequality to (3.39) results in

$$\tau'_{L+1} = \arg\min_{\tau'_k} \frac{\|\mathbf{P''}_{L_k}\|_F}{\mathbf{e}_{f'_k}^H \mathbf{e}_{f'_k}} \tag{3.41}$$

and after substituting τ'_{L+1}, which minimizes (3.41), into (3.39), we obtain

$$\mathbf{g}_{L+1} = \arg\min_{\mathbf{g}_k} \frac{\mathbf{g}_k^H \mathbf{P''}_L \mathbf{g}_k}{\mathbf{g}_k^H \mathbf{g}_k}. \tag{3.42}$$

The equation (3.42) is minimized by choosing the vector $\mathbf{g}_{L+1}$ to be equal to the eigenvector corresponding to the smallest eigenvalue of the matrix $\mathbf{P''}_L$.

In passing note that the simulation model parameters $\{\mathbf{g}_{L+1}, f_{d_{L+1}}, \tau'_{L+1}\}$ can be computed directly from the eigenvector $\mathbf{u}_L$ without generating the matrices $\mathbf{P}_L$, $\mathbf{P'}_L$, and $\mathbf{P''}_L$ as in (3.38), (3.41), and (3.42).

The squared gain factor c_{L+1}^2 is determined as

$$c_{L+1}^2 = \frac{\langle \hat{\hat{\underline{\mathbf{R}}}}_{res_L}, \mathbf{X}_{L+1} \rangle}{\langle \mathbf{X}_{L+1}, \mathbf{X}_{L+1} \rangle} \tag{3.43}$$

where the matrix $\mathbf{X}_{L+1} \in \mathcal{X}$ is obtained by substituting the computed parameters $\{\mathbf{g}_{L+1}, f_{d_{L+1}}, \tau'_{L+1}\}$ into (3.31). Since the residual error matrix $\hat{\hat{\underline{\mathbf{R}}}}_{res_L}$ is Hermitian, the parameter c_{L+1}^2 is real. However, because the matrix $\hat{\hat{\underline{\mathbf{R}}}}_{res_L}$ cannot be guaranteed to be positive definite, the parameter c_{L+1}^2 can be negative. If this is

the case, no solution to the maximization problem in (3.30) can be found using the method described above, i.e., the final approximation residual error is then given by the matrix $\hat{\hat{\underline{\mathbf{R}}}}_{res_L}$ (see (3.28)).

The empirical results of applying the proposed parameter computation method demonstrate that the residual approximation error can be significantly reduced by applying the cyclic minimization technique [59].

As before, presume that the matrices $\{\mathbf{X}_l\}_1^L \in \mathcal{X}$ and the corresponding squared gain factors $\{c_l^2\}_1^L$ have been determined. Using the computational steps described in (3.30)–(3.42), we obtain the set of parameters $\left\{\mathbf{g}_{L+1}, f_{d_{L+1}}, \tau'_{L+1}\right\} \in \Gamma$ and, consequently, the matrix $\mathbf{X}_{L+1} \in \mathcal{X}$. We assume that $c_{L+1}^2 \geq 0$. Otherwise, the minimization of the Frobenius norm (3.17) is finalized with the residual approximation error matrix $\hat{\hat{\underline{\mathbf{R}}}}_{res_L}$.

The matrices $\{\mathbf{X}_l\}_1^{L+1}$ and the squared gain factors $\{c_l^2\}_1^{L+1}$ are supplied as initial parameter values $\{\mathbf{X}_l^{(0)}\}_1^{L+1}$ and $\{c_l^{2\,(0)}\}_1^{L+1}$ into an iterative minimization procedure described below.

On every iteration q, $q = 1, 2, \ldots$, the following steps are executed:

1) For $p = 1, \ldots, L+1$, we culculate the auxiliary matrices $\mathbf{Z}_p^{(q)}$ according to

$$\mathbf{Z}_p^{(q)} = \begin{cases} \hat{\hat{\underline{\mathbf{R}}}} - \sum_{l=2}^{L+1} c_l^{2(q-1)} \mathbf{X}_l^{(q-1)}, & p = 1 \\ \hat{\hat{\underline{\mathbf{R}}}} - \sum_{l=1}^{p-1} c_l^{2(q)} \mathbf{X}_l^{(q)} - \sum_{l=p+1}^{L+1} c_l^{2(q-1)} \mathbf{X}_l^{(q-1)}, & 2 \leq p \leq L \\ \hat{\hat{\underline{\mathbf{R}}}} - \sum_{l=1}^{L} c_l^{2(q)} \mathbf{X}_l^{(q)}, & p = L+1. \end{cases} \quad (3.44)$$

   Use the matrix $\mathbf{Z}_p^{(q)}$ in lieu of $\hat{\hat{\underline{\mathbf{R}}}}_{res_L}$ in (3.30)–(3.43) to compute the parameters $\left\{\mathbf{g}_p^{(q)}, f_{d_p}^{(q)}, \tau_p'^{(q)}, c_p{}^{(q)}\right\}$.

2) Calculate the Frobenius norm of the residual approximation error matrix $\hat{\hat{\underline{\mathbf{R}}}}_{res_{L+1}}^{(q)}$ as follows

$$\|\hat{\hat{\underline{\mathbf{R}}}} - \sum_{l=1}^{L+1} c_l^{2(q)} \mathbf{X}_l^{(q)}\|_F = \|\hat{\hat{\underline{\mathbf{R}}}}_{res_{L+1}}^{(q)}\|_F. \quad (3.45)$$

3) If the condition $\|\hat{\hat{\underline{\mathbf{R}}}}_{res_{L+1}}^{(q)}\|_F < \|\hat{\hat{\underline{\mathbf{R}}}}_{res_{L+1}}^{(q-1)}\|_F$ is satisfied, begin a new iteration. Alternatively, set the channel simulator parameters $\{\mathbf{g}_l, f_{d_l}, \tau'_l, c_l\}_1^{L+1}$ equal to $\left\{\mathbf{g}_l^{(q)}, f_{d_l}^{(q)}, \tau_l'^{(q)}, c_l{}^{(q)}\right\}_1^{L+1}$ and proceed with determining the initial values for the parameters $\left\{\mathbf{g}_{L+2}, f_{d_{L+2}}, \tau'_{L+2}, c_{L+2}\right\}$ using (3.30)–(3.43).

As it has already been mentioned, the parameter computation algorithm developed above is based on the MP approach [57]. In particular, it inherits the energy conservation property of the MP method [55], which results in decrease

of the approximation error given by (3.29), as the number of components L increases. The convergence of the general MP method has been analyzed in [55,57]. Taking into account the arguments given in [55,57] and also the comments in [60], we conclude that the proposed method of determining the parameters $\mathcal{P}$ of the channel simulation model in (3.7) can be considered only as a heuristic algorithm. That means that even though the Frobenius norm of the residual approximation error matrix $\hat{\underline{\mathbf{R}}}_{res_L}$ is a strictly nonincreasing function of the number of the components L, it does not imply that the proposed algorithm necessarily produces the optimal solution to the problem stated in Section 3.3.

The iterative nature of the parameter computation algorithm described in this section impedes an assessment of its computational complexity. Furthermore, the complexity of the algorithm depends on the properties of the estimated correlation matrix $\hat{\underline{\mathbf{R}}}$ and desired (acceptable) accuracy of the correlation matrix approximation, i.e., the acceptable residual approximation error norm $\|\hat{\underline{\mathbf{R}}}_{res_L}\|_F$ (3.29).

3.5 Simulation Results

Here, we verify the correctness of the iterative parameter computation algorithm described in the previous section. Additionally, we investigate the influence of the white noise present in the measured TVFR of a wireless channel exerted on the performance of the algorithm. For these purposes, we employ the geometrical two-ring channel simulation model that has been used in Section 2.3. Note that the correlation matrix $\breve{\underline{\mathbf{R}}}$ of the geometrical two-ring channel simulation model, which is defined similarly to (3.11), can be easily obtained by substituting the known gains $\{\breve{c}_l\}_1^L$, the Doppler frequencies $\{\breve{f}_{d_l}\}_1^L$, the propagation delays $\{\breve{\tau}'_l\}_1^L$, and the vectors $\{\breve{\mathbf{g}}_l\}_1^L$ into (3.11), (3.12), (3.13), and (3.14), respectively. The vector $\breve{\mathbf{g}}_l$, $l = 1, \ldots, L$, is given by the Kroneker product of the steering vector (see Chapter 5) of a transmitting antenna, calculated for the known direction-of-departure (DOD) ψ_l, and the steering vector of a receiving antenna, calculated for the known direction-of-arrival (DOA) ϕ_l. Below, we refer to the correlation matrix $\breve{\underline{\mathbf{R}}}$ of the geometrical two-ring channel simulation model as the *sample* correlation matrix.

Some of the parameters of the geometrical two-ring channel simulation model read as (see also Section 2.3):

- Number of scatterers: $L = 50$;
- Receiving antenna: 2-element omnidirectional uniform linear array;
- Transmitting antenna: 2-element omnidirectional uniform linear array;
- Time between channel snapshots: $\triangle t = 0.07$ s;

- Maximum Doppler frequency: 7 Hz;
- SNR: 5 dB.

According to the problem formulation stated in Section 3.3, we determine the set of parameters $\mathcal{P} = \left\{L, \{c_l\}_1^L, \{\mathbf{g}_l\}_1^L, \{f_{d_l}\}_1^L, \{\tau_l'\}_1^L\right\}$ of the channel simulation model (3.7) as follows

$$\hat{\mathcal{P}} = \min_{\mathcal{P}} \left\|\underline{\check{\mathbf{R}}} - \underline{\mathbf{R}}\right\|_F \tag{3.46}$$

where the matrix $\underline{\check{\mathbf{R}}} = \underline{\check{\mathbf{R}}} + \sigma^2\mathbf{I}$ is the *sample-plus-noise* correlation matrix. The term $\sigma^2\mathbf{I}$ represents the correlation matrix of the complex zero-mean multivariate Gaussian white noise. The parameter σ^2 signifies the power of the noise component corresponding the specified SNR. The identity matrix $\mathbf{I}$ is of the same dimensions as the *sample* correlation matrix $\underline{\check{\mathbf{R}}}$.

In Fig. 3.1, several examples of the *sample-plus-noise* temporal cross-correlation functions (TCCFs) $\check{r}_{t_{i_1,i_2}}[\iota]$ and the *sample-plus-noise* frequency cross-correlation functions (FCCFs) $\check{r}_{f'_{i_1,i_2}}[\kappa]$, $i_1, i_2 = 1, \ldots, N_T N_R$, are presented together with the corresponding TCCFs $r_{t_{i_1,i_2}}[\iota]$ and FCCFs $r_{f'_{i_1,i_2}}[\kappa]$ of the channel simulation model (3.7). The TCCFs $\check{r}_{t_{i_1,i_2}}[\iota]$ and FCCFs $\check{r}_{f'_{i_1,i_2}}[\kappa]$ are extracted from the calculated *sample-plus-noise* correlation matrix[5] $\underline{\check{\mathbf{R}}}$ (see Section 3.2). Similarly, the TCCFs $r_{t_{i_1,i_2}}[\iota]$ and FCCFs $r_{f'_{i_1,i_2}}[\kappa]$ are extracted from the correlation matrix $\underline{\mathbf{R}}$. In Fig. 3.1, we also show the *sample* TCCFs $\check{r}_{f'_{i_1,i_2}}[\kappa]$ and the sample FCCFs $\check{r}_{f'_{i_1,i_2}}[\kappa]$ of the geometrical two-ring channel simulation model for the noise-free case, extracted from the *sample* correlation matrix $\underline{\check{\mathbf{R}}}$.

As can be seen from the figure, the correlation properties of the resulting channel simulation model (3.7) closely approximate the corresponding correlation properties of the geometrical two-ring channel simulation model and are not significantly effected by the presence of the noise component in the *sample-plus-noise* correlation matrix $\underline{\check{\mathbf{R}}}$. The observed resistance of the parameter computation method to the white noise present in the TVFR can be attributed to the fact that the eigenvectors of the sample correlation matrix $\underline{\check{\mathbf{R}}}$ are also the eigenvectors of the *sample-plus-noise* correlation matrix $\underline{\check{\mathbf{R}}}$. Recall that the channel simulator parameters $\left\{\{\mathbf{g}_l\}_1^L, \{f_{d_l}\}_1^L, \{\tau_l'\}_1^L\right\}$ are determined by using the eigenvectors of the correlation matrix $\underline{\check{\mathbf{R}}}$ (see Subsection 3.4.2). It should be mentioned, however, that the capability to single out the white noise component contained in the correlation matrix to a large extend depends on the range of the time lags $|\iota| \leq \iota_{\max}$ and the range of the frequency lags $|\kappa| \leq \kappa_{\max}$, at which the correlation properties of the channel TVFR are estimated. The conducted simulations sug-

[5]The *sample-plus-noise* TCCFs $\check{r}_{t_{i_1,i_2}}[\iota]$ and the *sample-plus-noise* FCCFs $\check{r}_{f'_{i_1,i_2}}[\kappa]$, $i_1, i_2 = 1, \ldots, N_T N_R$, are defined as $E\{\check{h}_{i_1}[m,n]\check{h}^*_{i_2}[m,n+\iota]\}$ and $E\{\check{h}_{i_1}[m,n]\check{h}^*_{i_2}[m+\kappa,n]\}$, respectively, where $\check{h}_i[m,n]$, $i = 1, \ldots, N_T N_R$, designates the TVFR of the i-th subchannel synthesized by using the geometrical two-ring channel simulation model and contaminated with white noise.

gest that for the chosen time interval between channel snapshots $\triangle t = 0.07$ s and the interval between the frequencies $\triangle f' = 1.957 \cdot 10^5$ Hz, the results similar to those presented in Fig. 3.1 are achieved when the values of $\kappa_{\max}$ and $\iota_{\max}$ satisfy the condition $\kappa_{\max}\iota_{\max} \geq 50$.

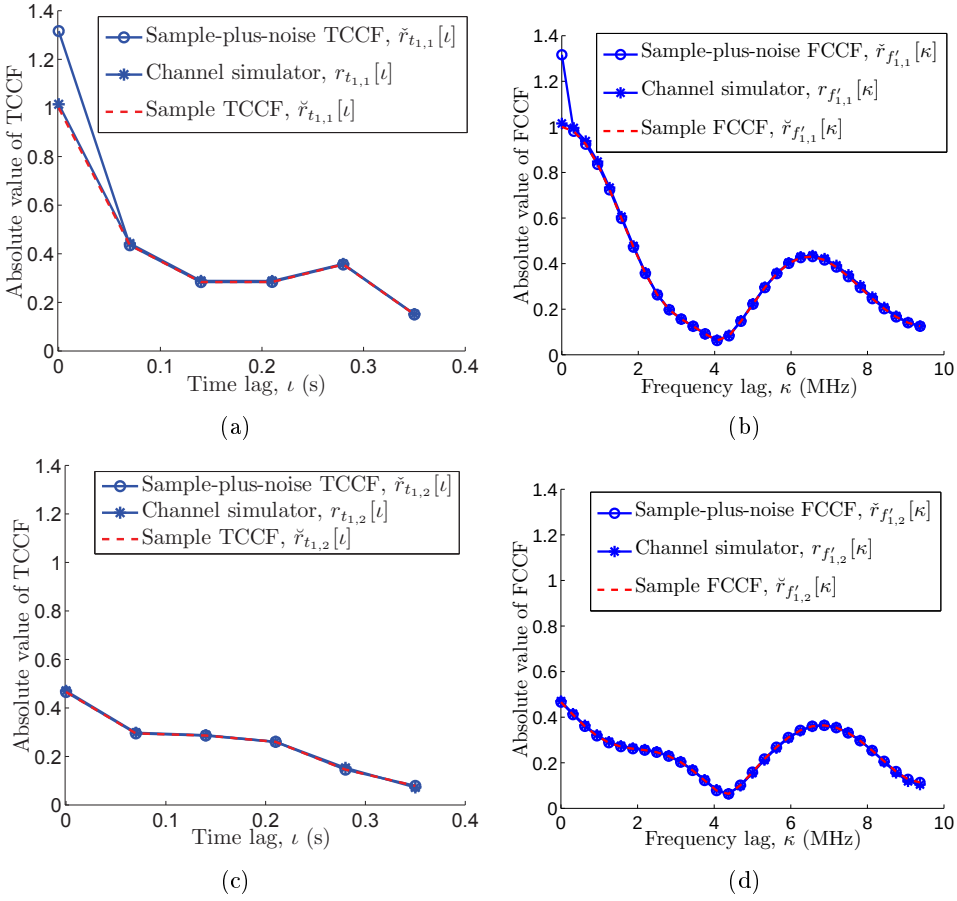

Figure 3.1: Examples of the TCCFs and FCCFs of the geometrical two-ring channel simulation model (with and without white noise) and the corresponding TCCFs and FCCFs of the designed channel simulator.

3.6 Applications to Real-World Measurement Data

The usefulness of the proposed design method is illustrated by constructing several MIMO wideband channel simulators based on the measured TVFRs of real-world channels. Our prime interest is to test the convergence of the parameter computation algorithm (see Section 3.4), as well as to assess the complexity of the channel simulators measured by the number of terms L in (3.7).

The channel simulator design method described in this chapter is based on the

assumption that the TVFR of a physical radio channel is WSS w.r.t. time and frequency. The intervals in the time-frequency plane, over which the measured TVFRs can be assumed WSS, have been identified using the stationarity test developed in Chapter 2.

The description of the measurement sites can be found in Appendix A. Additionally, Appendix A contains information about the measurement method and the equipment setup.

3.6.1 Micro Cell Site – Regular Street Geometry

The normalized residual approximation error norm $\|\hat{\underline{\mathbf{R}}}_{res_L}\|_F / \|\hat{\underline{\mathbf{R}}}\|_F$ versus the number of components L in (3.7) is depicted in Fig. 3.2 (a). As can be seen from the figure, the normalized error norm drops below 5% at $L = 63$. The resulting normalized error norm corresponding to $L = 120$ is about 3%.

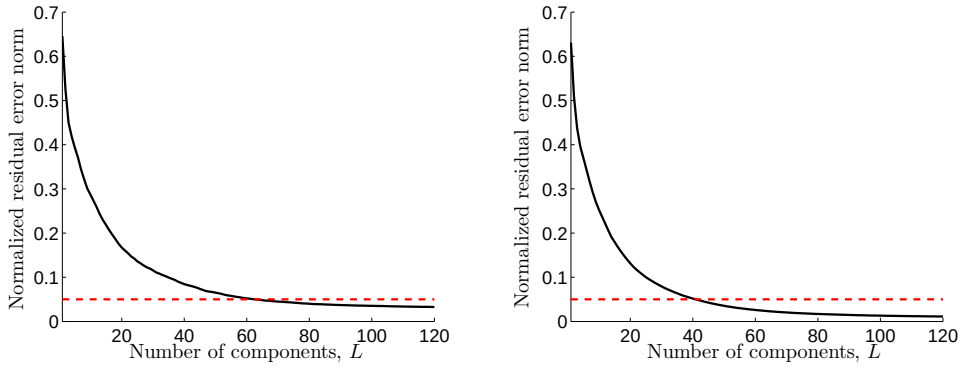

Figure 3.2: The normalized residual approximation error norm versus the number of components L for (a) the MIMO wideband channel simulator and (b) the truncated discrete KLE (micro cell site – regular street geometry).

For comparison reasons, we show in Fig. 3.2 (b) the results obtained from the truncated discrete KLE of the measured channel TVFR [61]. The normalized residual approximation error norm for the truncated discrete KLE is calculated according to the following expression

$$\|\hat{\underline{\mathbf{R}}}_{res_L}\|_F / \|\hat{\underline{\mathbf{R}}}\|_F = \sqrt{\frac{\sum_l \lambda_l^2 - \sum_{l \leq L} \lambda_l^2}{\sum_l \lambda_l^2}} \tag{3.47}$$

where $\lambda_1 \geq \lambda_2 \geq \ldots$ are the ordered eigenvalues of the matrix $\hat{\underline{\mathbf{R}}}$. The normalized error norm of 5% is achieved with $L = 41$ principal components corresponding to

the largest eigenvalues of the estimated correlation matrix $\hat{\underline{\underline{\mathbf{R}}}}$. For $L = 120$, the normalized error norm is about 1%.

It is important to note that the truncated discrete KLE provides the optimal, in the mean-square error sense, approximation of the estimated correlation matrix $\hat{\underline{\underline{\mathbf{R}}}}$ for a given L. As we have mentioned in Section 3.2, the disadvantage of the truncated discrete KLE is the lack of an analytical solution for the eigenvectors of the correlation matrix $\hat{\underline{\underline{\mathbf{R}}}}$. To illustrate this point, assume that we need to synthesize a realization of the channel TVFR on an interval of time of duration 0.7 s. Without going into details, it is sufficient to say that the size of the estimated correlation matrix $\tilde{\underline{\underline{\mathbf{R}}}}$ has to be doubled in each dimension as compared to the size of the correlation matrix enrolled in this subsection. If we applied the truncated discrete KLE to the enlarged matrix $\tilde{\underline{\underline{\mathbf{R}}}}$, the number of the principal components required to approximate the new correlation matrix with the same 5% normalized approximation error norm would be increased to $L = 62$, i.e., by 50%, and would be comparable with $L = 63$ exponential components in the channel simulation model (3.7).

In Fig. 3.3, several examples of the calculated TCCFs $r_{t_{i_1,i_2}}[\iota]$ and the FCCFs $r_{f'_{i_1,i_2}}[\kappa]$, $i_1, i_2 = 1, \ldots, N_T N_R$, are presented together with the corresponding estimated TCCFs $\hat{\tilde{r}}_{t_{i_1,i_2}}[\iota]$ and FCCFs $\hat{\tilde{r}}_{f'_{i_1,i_2}}[\kappa]$ of the measured channel. The estimated TCCFs $\hat{\tilde{r}}_{t_{i_1,i_2}}[\iota]$ and FCCFs $\hat{\tilde{r}}_{f'_{i_1,i_2}}[\kappa]$ of the measured channel are extracted from the estimated space-time-frequency correlation matrix $\hat{\underline{\underline{\mathbf{R}}}}$ (see Section 3.4). The approximate 95% confidence intervals [62] for the estimated TCCFs and FCCFs shown in Fig. 3.3 have been obtained assuming that the elements of the estimated matrices $\hat{\tilde{\mathbf{R}}}[\kappa, \iota]$ in (3.18) are complex Gaussian distributed random variables. As can be seen from Fig. 3.3, the correlation functions of the channel simulator are well fitted to the corresponding estimated correlation functions of the physical channel. A significant discrepancy exists between the TACFs $r_{t_{i,i}}[\iota]$ and the estimated TACFs $\hat{\tilde{r}}_{t_{i,i}}[\iota]$ at time lag $\iota = 0$ as well as between the FACFs $r_{f'_{i,i}}[\kappa]$ and the estimated FACFs $\hat{\tilde{r}}_{f'_{i,i}}[\kappa]$ at the frequency lag $\kappa = 0$. Taking into account the results presented in Section 3.5, a possible explanation for this discrepancy could be the presence of 'measurement' noise in the TVFR $\tilde{\mathbf{h}}[m, n]$, weakly correlated in time, frequency, and space.

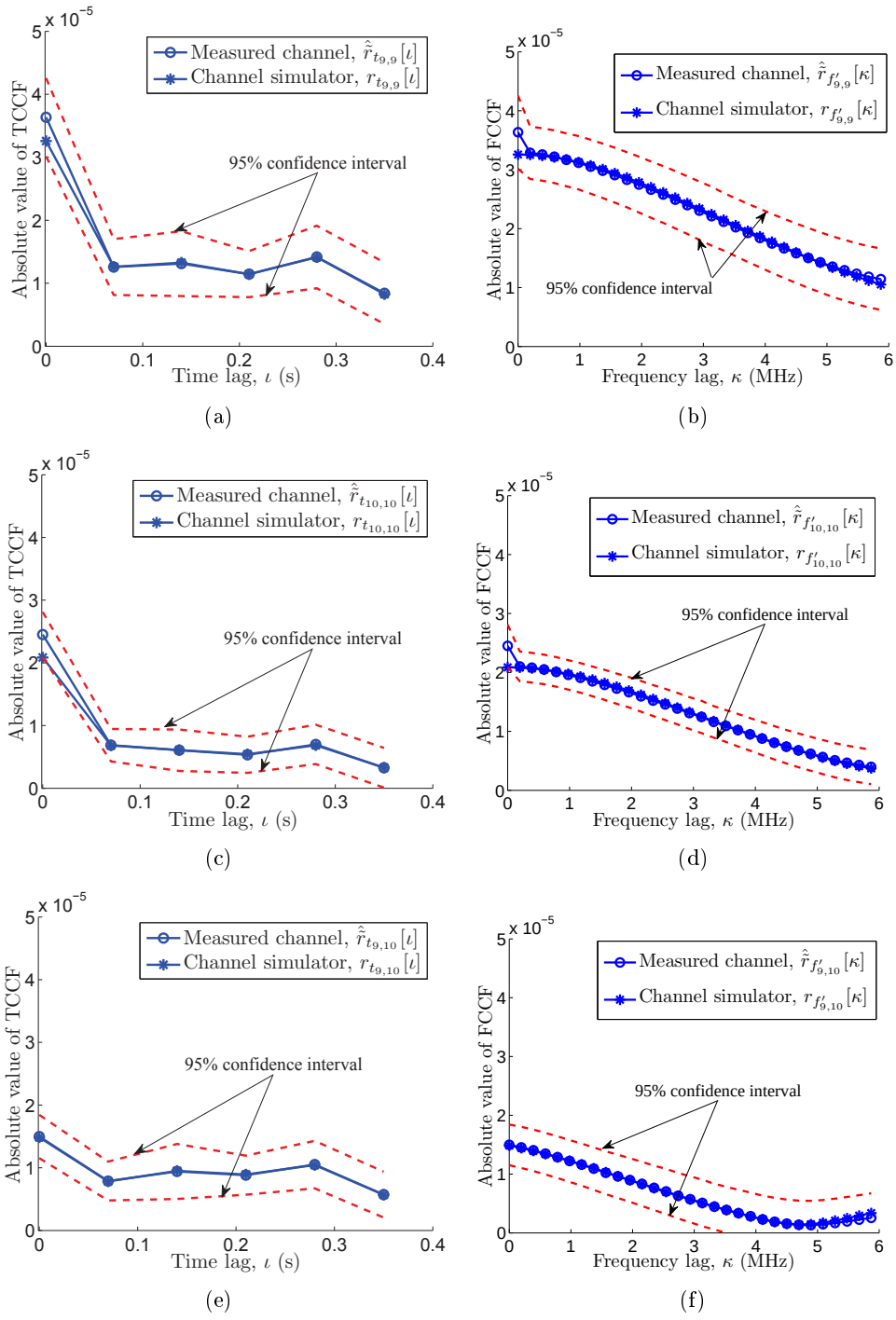

Figure 3.3: Examples of the estimated TCCFs and FCCFs of the physical channel and the corresponding TCCFs and FCCFs of the designed MIMO wideband channel simulator (micro cell site – regular street geometry).

Recall that the envelope PDFs of the subchannels $h_i[m,n]$, $i = 1,\ldots,N_TN_R$, are not directly taken into account in the design method described in Section 3.4. Nevertheless, it is of interest to consider the resulting envelope PDFs $p_{|h_i|}(x)$ given by (3.8) for a special case of the complex weighting coefficients with the constant magnitudes $\Xi_l = 1$, $l = 1,\ldots,L$, (see Section 3.2). Figure 3.4 presents the calculated envelope PDFs for two subchannels. The calculated envelope PDFs $p_{|h_i|}(x)$ in Fig. 3.4 are shown together with the estimated empirical envelope PDFs $p_{|\tilde{h}_i|}(x)$ and the Rayleigh PDFs corresponding to the complex weighting coefficients $U_l \sim \mathcal{CN}(0,1)$. Note that the envelope PDFs calculated by using (3.8) follow the Rayleigh distribution.

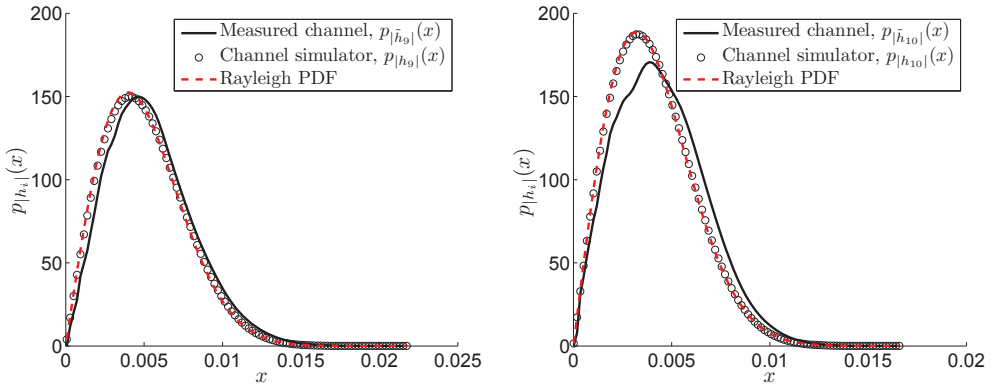

(a) (b)

Figure 3.4: Examples of the envelope PDFs for the MIMO wideband channel simulator $p_{|h_i|}(x)$ and the corresponding empirical PDFs $p_{|\tilde{h}_i|}(x)$ (micro cell site – regular street geometry).

In Fig. 3.5, the cumulative distribution functions (CDFs) of the instantaneous channel capacity (mutual information) of the measured channel and a synthesized channel are presented. The instantaneous capacity $C[n]$ for the simulated channel can be obtained for all time instances t_n, $n = 1,\ldots,N$, according to the definition [4, 41, 42]

$$C[n] = \frac{1}{M}\sum_{m=0}^{M-1} \log_2\left[\det\left(\mathbf{I} + \frac{\rho}{N_T F[n]}\mathbf{H}[m,n]\mathbf{H}^H[m,n]\right)\right] \tag{3.48}$$

where the channel matrix $\mathbf{H}[m,n]$ has been defined in (3.1), ρ denotes the signal-to-noise ratio (SNR), and $\mathbf{I}$ is the unity matrix. The normalization factor $F[n]$ at each time instance is given by

$$F[n] = \frac{1}{M}\sum_{m=0}^{M-1} \|\mathbf{H}[m,n]\|_F^2. \tag{3.49}$$

The instantaneous capacity of the measured physical channel is defined in a similar way.

Due to the fact that the number N of the available snapshots of the TVFR is limited for a real-world wireless channel, we split the available frequency bandwidth $B = 100$ MHz into smaller frequency bands of about 20 MHz. The instantaneous capacities of the measured channel and the simulated channel are calculated for each of the frequency bands according to the formulas (3.48) and (3.49).

As it can be seen from Fig. 3.5, the capacity CDF of the generated channel is biased compared to the capacity CDF of the measured channel. This result can be foreseen by inspecting the plots in Fig. 3.3. As it has already been mentioned, the TACFs $r_{t_{i,i}}[0]$ and the FACFs $r_{f'_{i,i}}[0]$, which define the variances of the generated TVFRs $h_i[m,n]$, $i = 1, \ldots, N_T N_R$, are smaller than the estimated TACFs $\hat{\tilde{r}}_{t_{i,i}}[0]$ and FACFs $\hat{\tilde{r}}_{f'_{i,i}}[0]$ of the corresponding measured TVFRs $\tilde{h}_i[m,n]$. It is of interest to investigate if the bias can be removed by adjusting the variances of the TVFRs $h_i[m,n]$, $i = 1, \ldots, N_T N_R$. For this purpose, a complex 'measurement' noise[6], uncorrelated in time, space, and frequency, is added to the generated realizations of the TVFR $\mathbf{h}[m,n]$. Indeed, as can be seen from Fig. 3.5, adding the 'measurement' noise, which follows the complex multivariate Gaussian distribution with zero means and the diagonal covariance matrix, to the TVFR $\mathbf{h}[m,n]$, eliminates the bias. The elements along the main diagonal of the 'measurement' noise covariance matrix are given by $\sigma_i^2 = \hat{\tilde{r}}_{t_{i,i}}[0] - r_{t_{i,i}}[0]$, $i = 1, \ldots, N_T N_R$.

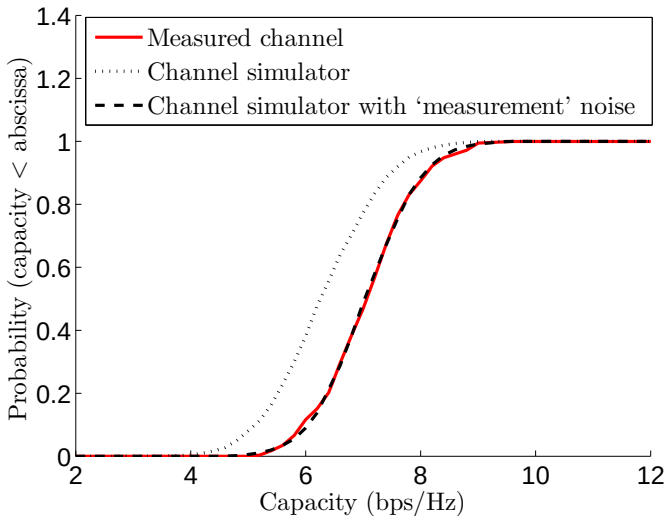

Figure 3.5: Capacity CDFs of the simulated channel and the measured channel for the SNR $\rho = 20$ dB (micro cell site – regular street geometry).

[6]The 'measurement' noise should not be confused with the noise at the input of a receiver represented by the SNR ρ in (3.48).

The estimated mean μ_C values and standard deviations σ_C of the instantaneous capacity of the measured channel and the simulated channels (with and without 'measurement' noise) are given in Table 3.1.

Table 3.1: Estimated mean and standard deviation of the capacity (micro cell site – regular street geometry).

	Measured channel	Channel simulator	Channel simulator with 'measurement' noise
Mean, μ_C (bps/Hz)	7.25	6.48	7.23
Standard deviation, σ_C (bps/Hz)	0.81	0.9	0.81

3.6.2 Micro Cell Site – Open Market Place

The normalized residual approximation error norm is shown in Fig. 3.6 (a). The 7% normalized error norm is achieved with $L = 179$ components in the channel simulation model (3.7). Compare this value with the results presented in Fig. 3.6 (b) for the truncated discrete KLE. Here, the 5% normalized error norm is achieved with $L = 104$ principal components, while for $L = 179$ components the normalized residual approximation error norm is about 2%.

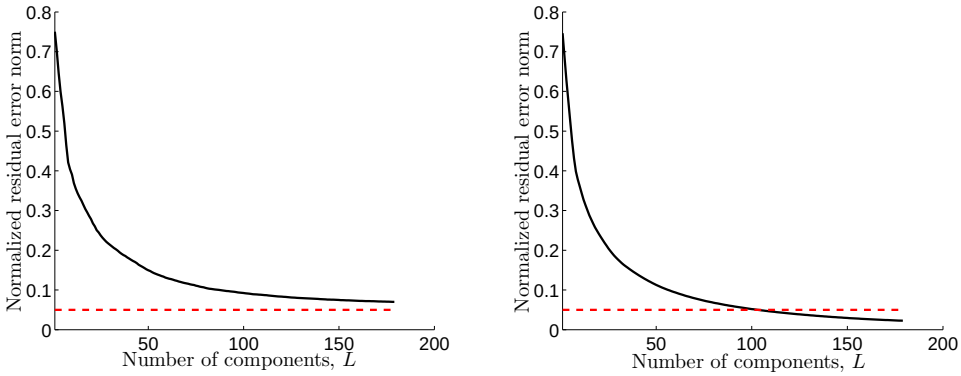

Figure 3.6: The normalized residual approximation error norm versus the number of components L for (a) the channel simulator and (b) the truncated discrete KLE (micro cell site – open market place).

Examples of the estimated TCCFs $\hat{\hat{r}}_{t_{i_1,i_2}}[\iota]$ and FCCFs $\hat{\hat{r}}_{f'_{i_1,i_2}}[\kappa]$ of the measured channel are depicted in Fig. 3.7 together with their respective counterparts $r_{t_{i_1,i_2}}[\iota]$ and $r_{f'_{i_1,i_2}}[\kappa]$ calculated for the developed channel simulator. As it can be seen from Fig 3.7, the TCCFs $r_{t_{i_1,i_2}}[\iota]$ and the FCCFs $r_{f'_{i_1,i_2}}[\kappa]$ of the designed channel simulator closely approximate the corresponding TCCFs and FCCFs estimated from the measurement data.

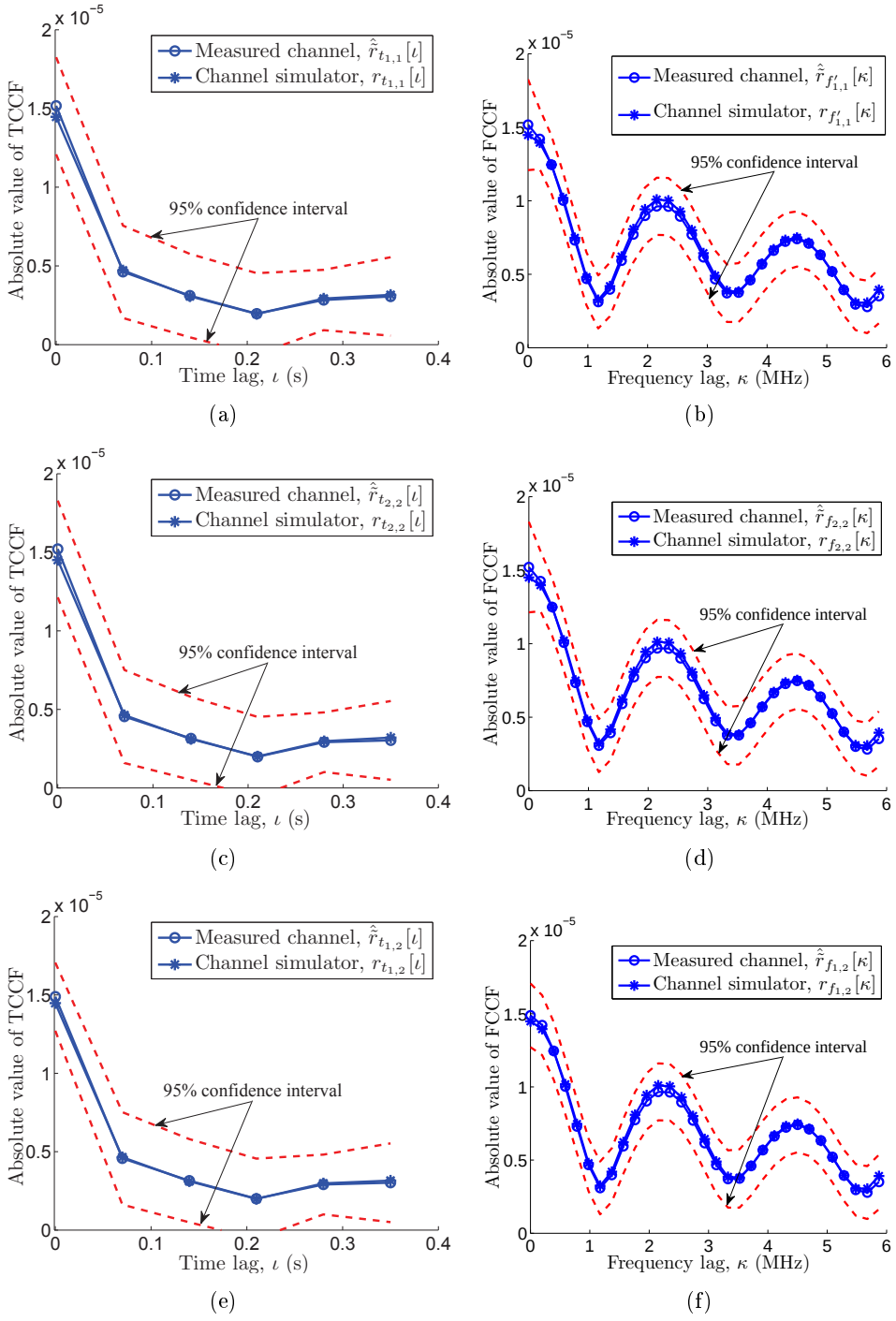

Figure 3.7: Examples of the estimated TCCFs and FCCFs of the physical channel and the corresponding TCCFs and FCCFs of the designed MIMO wideband channel simulator (micro cell site – open market place).

Examples of the envelope PDFs $p_{|h_i|}(x)$ (see (3.8)) and the empirical envelope PDFs $p_{|\tilde{h}_i|}(x)$ estimated from the measurement data are shown in Fig. 3.8. Clearly, the envelope PDFs $p_{|h_i|}(x)$ follow the Rayleigh distribution.

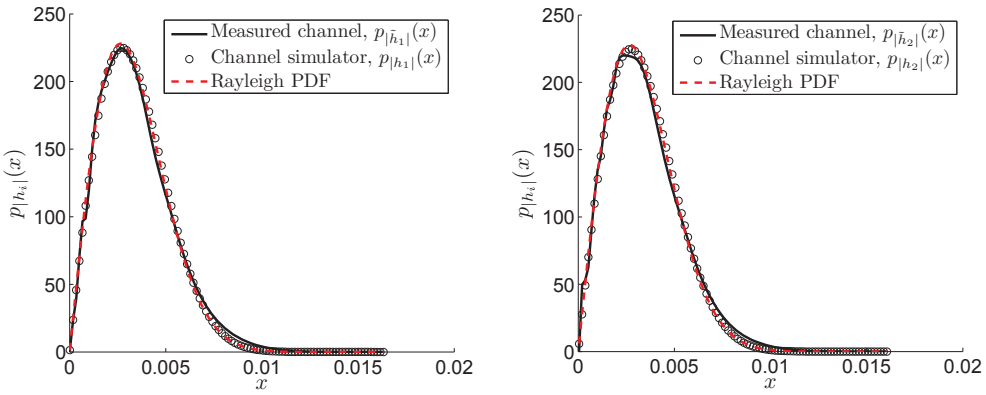

Figure 3.8: Examples of the envelope PDFs of the MIMO wideband channel simulator $p_{|h_i|}(x)$ and the corresponding empirical PDFs $p_{|\tilde{h}_i|}(x)$ (micro cell site – open market place).

The CDFs of the instantaneous channel capacity $C[n]$ of a synthesized channel and of the measured channel calculated as described in Subsection 3.6.1 are demonstrated in Fig. 3.9. Note the absence of the bias between the two CDF curves shown in the figure.

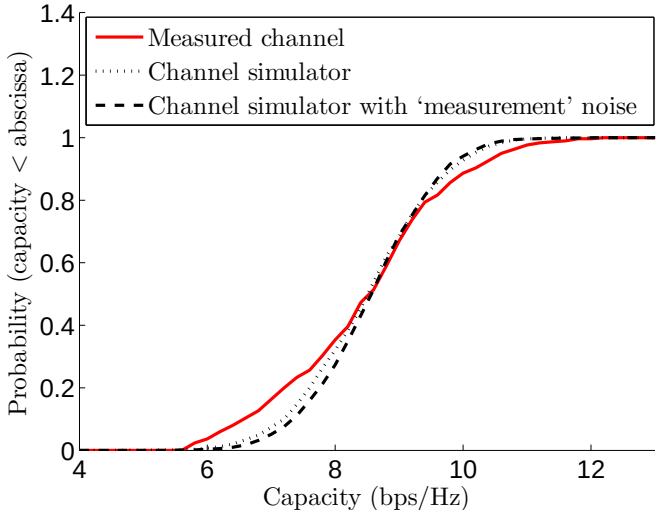

Figure 3.9: Capacity CDFs of the simulated channel and the measured channel for an SNR $\rho = 20$ dB (micro cell site – open market place).

The mean values μ_C and the standard deviations σ_C of the instantaneous capacity of the synthesized channel and the measured channel are presented in Table 3.2.

Table 3.2: Estimated mean and standard deviation of the capacity (micro cell site – open market place).

	Measured channel	Channel simulator	Channel simulator with 'measurement' noise
Mean, μ_C (bps/Hz)	8.63	8.67	8.75
Standard deviation, σ_C (bps/Hz)	1.32	1.05	0.93

3.6.3 Micro/Pico Cell Site – Passageway

In Figs. 3.10 (a)–(b), the normalized residual approximation error norm is shown for the channel simulator and the truncated discrete KLE, respectively. The 5% normalized error norm is achieved with $L = 143$ components in the channel simulator (3.7) vs. $L = 67$ principal components in case of the truncated discrete KLE (see (3.47)). Correspondingly, $L = 161$ components in (3.7) provide the normalized error norm below 4.9%, while for $L = 161$ components in the truncated discrete KLE the normalized error norm is below 3.5%.

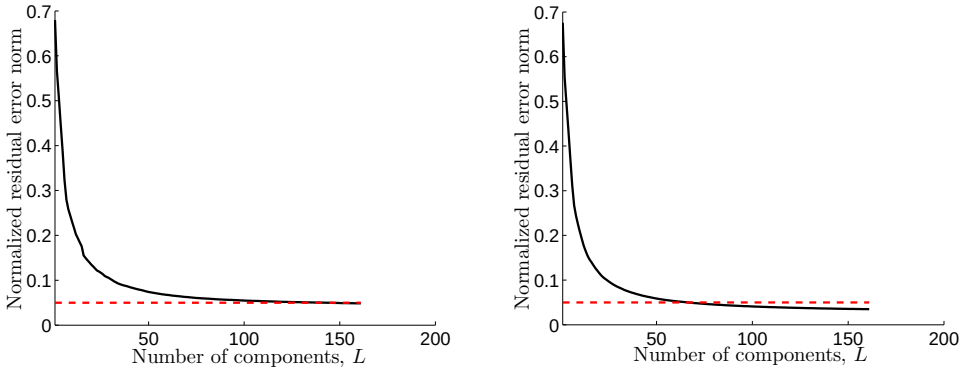

Figure 3.10: The normalized residual approximation error norm versus the number of components L for (a) the MIMO wideband channel simulator and (b) the truncated discrete KLE (micro/pico cell site – passageway).

Examples of the estimated TCCFs $\hat{\hat{r}}_{t_{i_1,i_2}}[\iota]$ and FCCFs $\hat{\hat{r}}_{f'_{i_1,i_2}}[\kappa]$ of the measured channel together with their respective counterparts $r_{t_{i_1,i_2}}[\iota]$ and $r_{f'_{i_1,i_2}}[\kappa]$ calculated for the developed channel simulator are depicted in Fig. 3.11.

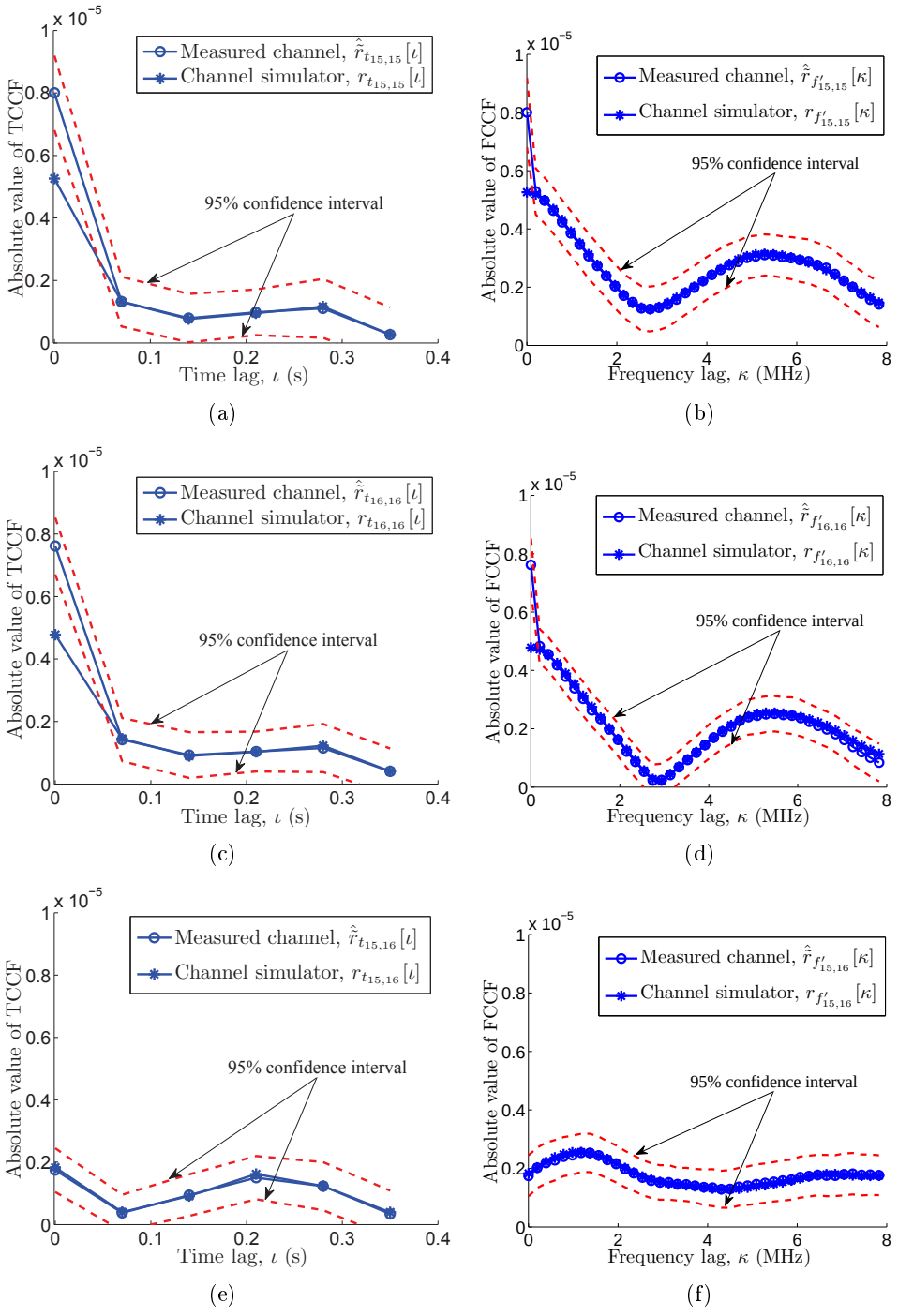

Figure 3.11: Examples of the estimated TCCFs and FCCFs of the physical channel and the corresponding TCCFs and FCCFs of the designed MIMO wideband channel simulator (micro/pico cell site – passageway).

Note the discrepancy between the TACFs $\hat{\tilde{r}}_{t_{i,i}}[\iota]$ and $r_{t_{i,i}}[\iota]$ at time lag $\iota = 0$, and between the FACFs $\hat{\tilde{r}}_{f'_{i,i}}[\kappa]$ and $r_{f'_{i,i}}[\kappa]$ at frequency lag $\kappa = 0$.

Figure 3.12, demonstrates the examples of the envelope PDFs $p_{|h_i|}(x)$ (see (3.8)). The corresponding empirical envelope PDFs $p_{|\tilde{h}_i|}(x)$ are also plotted in the same figure. It can be observed that the envelope PDFs $p_{|h_i|}(x)$ given by (3.8) follow the Rayleigh distributions. In Fig. 3.12, it is shown that the empirical envelope PDFs $p_{|\tilde{h}_i|}(x)$ also follow the Rayleigh distributions. Thus, the evident discrepancy between the envelope PDFs $p_{|h_i|}(x)$ and the empirical envelope PDFs in Fig. 3.12 is due to the difference in the variances (the TACFs $r_{t_{i,i}}[0]$ and $\hat{\tilde{r}}_{t_{i,i}}[0]$ in Fig. 3.11) of the corresponding random processes h_i and $\tilde{h}_i$.

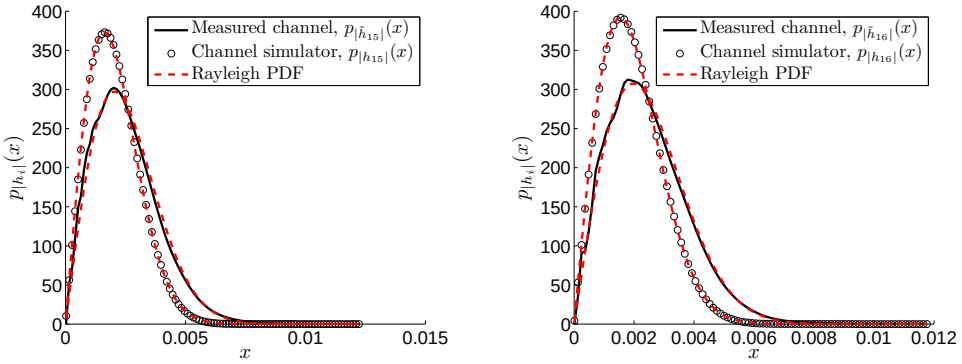

Figure 3.12: Examples of the envelope PDFs of the MIMO wideband channel simulator $p_{|h_i|}(x)$ and the corresponding empirical PDFs $p_{|\tilde{h}_i|}(x)$ (micro/pico cell site – passageway).

In Fig. 3.13, the CDFs of the instantaneous channel capacity (see Subsection 3.6.1) of the measured channel and of a simulated channel realization are depicted. Observe, that the mismatch between the capacity CDFs (bias) can be reduced by adding a white 'measurement' noise to the simulated TVFR $\mathbf{h}[m, n]$, as described in Subsection 3.6.1.

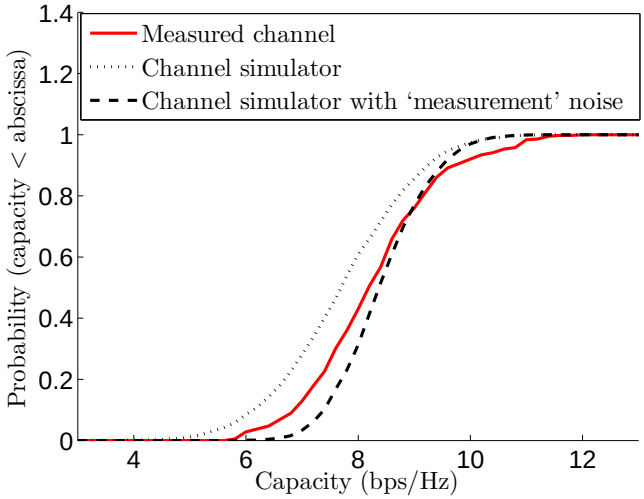

Figure 3.13: Capacity CDFs of a simulated channel and the measured channel for an SNR $\rho = 20$ dB (micro/pico cell site – passageway).

The mean values μ_C and the standard deviations σ_C of the instantaneous capacity of the simulated channels and the measured channel are presented in Table 3.3.

Table 3.3: Estimated mean and standard deviation of the capacity (micro/pico cell site – passageway).

	Measured channel	Channel simulator	Channel simulator with 'measurement' noise
Mean, μ_C (bps/Hz)	8.45	7.9	8.59
Standard deviation, σ_C (bps/Hz)	1.17	1.21	0.82

3.6.4 Indoor Cell Site

For the indoor propagation scenario, the normalized residual approximation error norm versus the number of components L is shown in Figs. 3.14 (a)–(b) for the channel simulator and the truncated discrete KLE, respectively. In this case, the normalized error norm for the designed channel simulator has converged to 10% for $L = 220$ components (see (3.7)). The truncated discrete KLE with $L = 220$ principal components provides the normalized residual approximation error norm of about 2%. For the reference, the 5% normalized error norm is achieved with $L = 139$ components in case of the truncated discrete KLE.

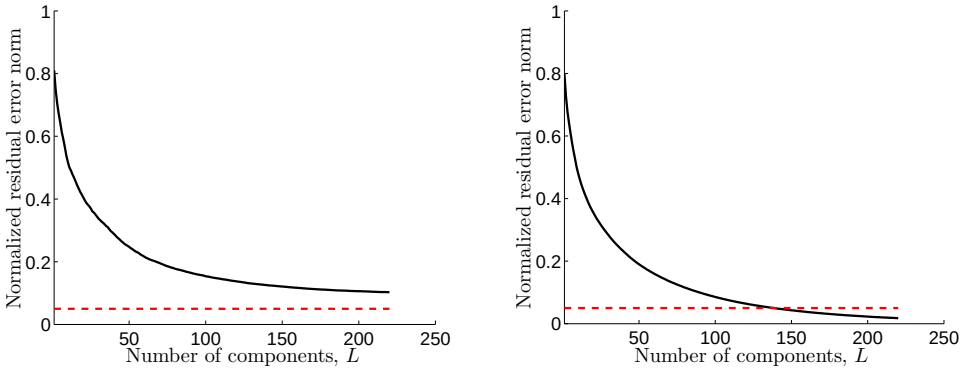

Figure 3.14: The normalized residual approximation error norm versus the number of components L for (a) the channel simulator and (b) the truncated discrete KLE (indoor cell site).

Fig. 3.15 depicts several examples of the TCCFs $\hat{\tilde{r}}_{t_{i_1,i_2}}[\iota]$ and FCCFs $\hat{\tilde{r}}_{f'_{i_1,i_2}}[\kappa]$, estimated from the measurement data, as well as the TCCFs $r_{t_{i_1,i_2}}[\iota]$ and the FCCFs $r_{f'_{i_1,i_2}}[\kappa]$, calculated for the developed channel simulator. As can be seen from Fig. 3.15, the approximation of the FCCFs is worse compared to the propagation scenarios considered in the previous subsections.

Examples of the envelope PDFs $p_{|h_i|}(x)$ obtained by using (3.8) and the corresponding empirical envelope PDFs $p_{|\tilde{h}_i|}(x)$ estimated from the measured TVFRs are shown in Fig. 3.16. We observe that the envelope PDFs $p_{|h_i|}(x)$ given by (3.8) follow the Rayleigh PDF.

The instantaneous channel capacity CDFs of the measured channel and of a generated channel realization (see Subsection 3.6.1) are demonstrated in Fig. 3.16. The mean values μ_C and the standard deviations σ_C of the instantaneous capacity are presented in Table 3.4.

Table 3.4: Estimated mean and standard deviation of the capacity (indoor cell site).

	Measured channel	Channel simulator	Channel simulator with 'measurement' noise
Mean, μ_C (bps/Hz)	8.15	7.97	8.1
Standard deviation, σ_C (bps/Hz)	1.03	0.85	0.79

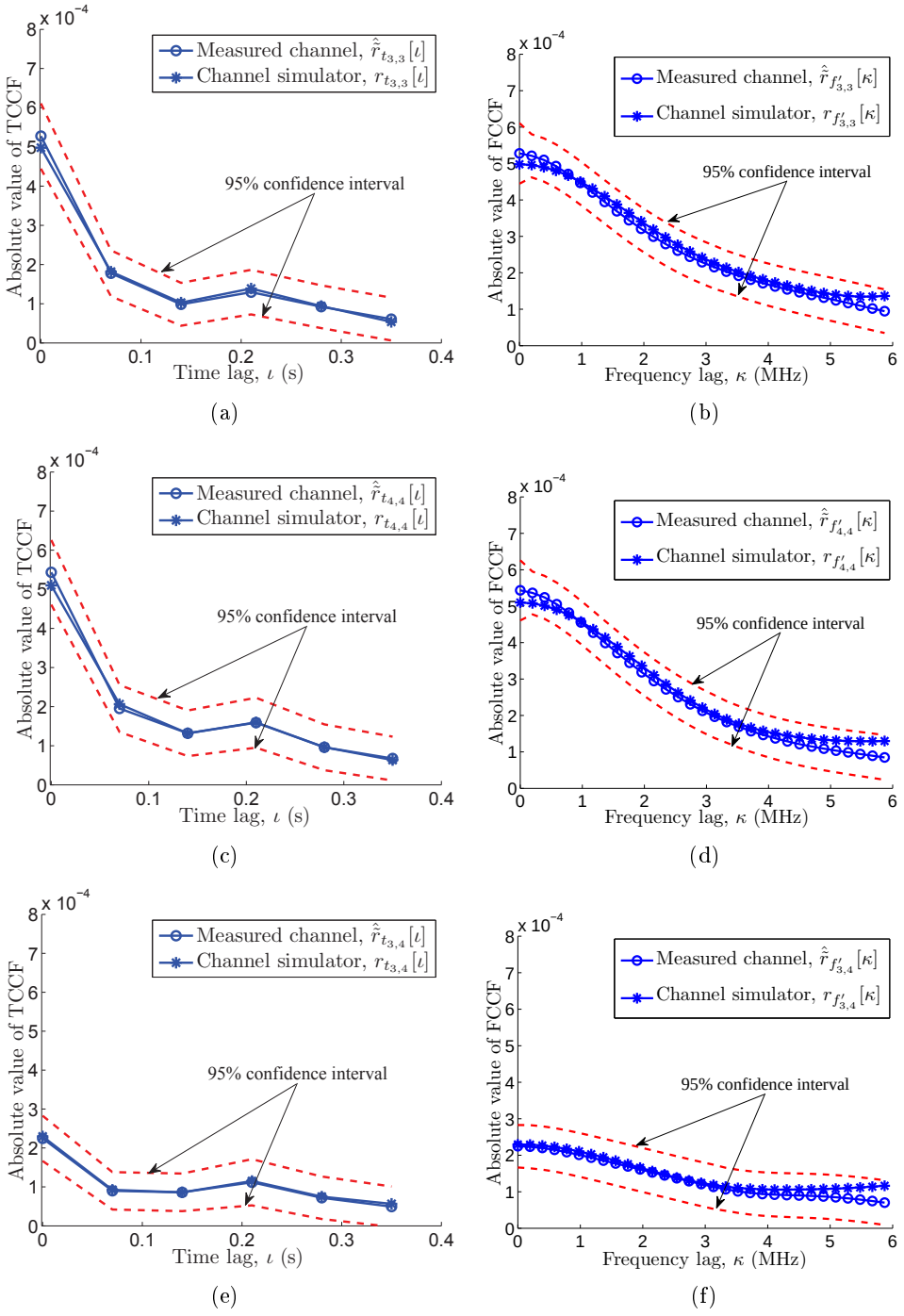

Figure 3.15: Examples of the estimated TCCFs and FCCFs of the physical channel and the corresponding TCCFs and FCCFs of the designed MIMO wideband channel simulator (indoor cell site).

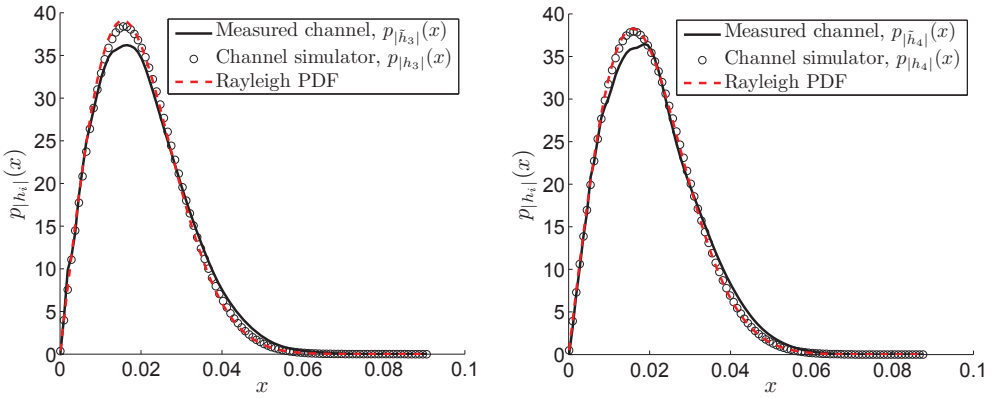

Figure 3.16: Examples of the envelope PDFs of the MIMO wideband channel simulator $p_{|h_i|}(x)$ and the corresponding empirical PDFs $p_{|\tilde{h}_i|}(x)$ (indoor cell site).

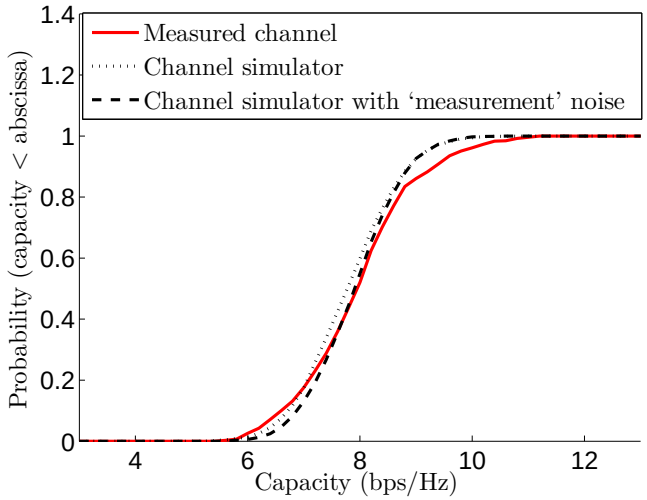

Figure 3.17: Capacity CDFs for a simulated channel and the measured channel for an SNR $\rho = 20$ dB (indoor cell site).

3.7 Design of Measurement-Based Stochastic Channel Simulators for MIMO Narrowband Channels

So far, we have been concerned with the design of stochastic channel simulators for MIMO wideband channels. In this section, we describe an adaptation of the method, proposed in the previous sections, for designing measurement-based channel simulators for MIMO narrowband channels. In agreement with the definition of a narrowband channel [3, 4], it is presumed that the TVFR $\tilde{\mathbf{H}}[m,n]$ of a real-world $N_T \times N_R$ MIMO wireless channel has a constant magnitude and a linear phase shift over the frequency interval $[-B/2, B/2]$ (flat fading).

3.7.1 Stochastic Channel Simulation Model

The synthesized TVFR of a MIMO narrowband wireless channel at discrete time instances $t_n = n\triangle t \in [0,T]$, $n = 0,\ldots,N-1$, is represented by the matrix sequence

$$\mathbf{H}[n] = \begin{pmatrix} H_{1,1}[n] & \ldots & H_{1,N_R}[n] \\ \vdots & \ddots & \vdots \\ H_{N_T,1}[n] & \ldots & H_{N_T,N_R}[n] \end{pmatrix}. \tag{3.50}$$

The TVFR $\mathbf{H}[n]$, in the vectorized form, is generated using the following simulation model

$$\mathbf{h}[n] = vec(\mathbf{H}[n]) = \sum_{l=1}^{L} c_l \mathbf{g}_l e^{j2\pi f_{d_l} t_n} U_l. \tag{3.51}$$

where the set of parameters $\mathcal{P} = \left\{L, \{c_l\}_1^L, \{\mathbf{g}_l\}_1^L, \{f_{d_l}\}_1^L\right\}$ and the complex weighting coefficients $\{U_l\}_1^L$ are specified as in Section 3.2.

The space-time correlation matrix $\underline{\mathbf{R}}$ is defined as follows

$$\underline{\mathbf{R}} = E\left\{\mathbf{v}[n]\mathbf{v}^H[n]\right\} = \begin{bmatrix} \mathbf{R}[0] & \cdots & \mathbf{R}[-\iota_{\max}] \\ \vdots & \ddots & \vdots \\ \mathbf{R}[\iota_{\max}] & \cdots & \mathbf{R}[0] \end{bmatrix}. \tag{3.52}$$

where the vector $\mathbf{v}[n]$ is defined by $\mathbf{v}[n] = [\mathbf{h}^T[n] \ldots \mathbf{h}^T[n-\iota_{\max}]]^T$. Using (3.51), the correlation matrix $\underline{\mathbf{R}}$ can be written as

$$\underline{\mathbf{R}} = \sum_{l=1}^{L} c_l^2 \mathbf{R}_{t_l} \otimes \mathbf{R}_{g_l} \tag{3.53}$$

where the matrices $\mathbf{R}_{t_l}$ and $\mathbf{R}_{g_l}$ are defined in (3.12) and (3.14), respectively.

3.7.2 Parameter Computation Method

The following criterion is proposed for determining the set of parameters $\mathcal{P}$ of the channel simulation model (3.51)

$$\hat{\mathcal{P}} = \min_{\mathcal{P}} \left\| \hat{\underline{\underline{\mathbf{R}}}} - \sum_{l=1}^{L} c_l^2 \mathbf{R}_{t_l} \otimes \mathbf{R}_{g_l} \right\|_F \tag{3.54}$$

where $\hat{\underline{\underline{\mathbf{R}}}}$ is the estimated correlation matrix, which is defined similarly to (3.52) as

$$\hat{\underline{\underline{\mathbf{R}}}} = \begin{bmatrix} \hat{\mathbf{R}}[0] & \cdots & \hat{\mathbf{R}}[-\iota_{\max}] \\ \vdots & \ddots & \vdots \\ \hat{\mathbf{R}}[\iota_{\max}] & \cdots & \hat{\mathbf{R}}[0] \end{bmatrix}. \tag{3.55}$$

The consistent estimates of the correlation matrices $\hat{\mathbf{R}}[\iota]$, $\iota = -\iota_{\max}, \ldots, 0, \ldots, \iota_{\max}$, $\iota_{\max} \in \mathbb{R}$ in (3.55) are obtained as

$$\hat{\mathbf{R}}[\iota] = \frac{1}{(N - |\iota|)} \sum_{n=0}^{N-1-|\iota|} \tilde{\mathbf{h}}[n] \tilde{\mathbf{h}}^H[n + \iota]. \tag{3.56}$$

The minimization of the Frobenius norm in (3.54) is accomplished by applying an adapted version of the iterative parameter computation method described in Subsection 3.4.2. The method is based on decomposing the estimated correlation matrix $\hat{\underline{\underline{\mathbf{R}}}}$ over a library $\mathcal{X}$ of the Hermitian matrices $\mathbf{X} = \mathbf{R}_t \otimes \mathbf{R}_g$, where each member $\mathbf{X}_k = \mathbf{R}_{t_k} \otimes \mathbf{R}_{g_k}$ of the matrix library can be written as (*cf.* (3.31))

$$\mathbf{X}_k = \mathbf{x}_k \mathbf{x}_k^H = (\mathbf{e}_{t_k} \otimes \mathbf{g}_k)(\mathbf{e}_{t_k} \otimes \mathbf{g}_k)^H. \tag{3.57}$$

The set of parameters $\mathcal{P} = \left\{L, \{c_l\}_1^L, \{\mathbf{g}_l\}_1^L, \{f_{d_l}\}_1^L\right\}$ is computed according to the procedure described in Subsection 3.4.2. However, the Equations (3.39)–(3.42) are to be dropped as they are not relevant for narrowband channels. Instead, after substituting the Doppler frequency $f_{d_{L+1}}$, which minimizes (3.38), into (3.36), the vector $\mathbf{g}_{L+1}$ is found as

$$\mathbf{g}_{L+1} = \arg\min_{\mathbf{g}_k} \frac{\mathbf{g}_k^H \mathbf{P'}_L \mathbf{g}_k}{\mathbf{g}_k^H \mathbf{g}_k}. \tag{3.58}$$

Below, we present some examples of designing channel simulators for real-world MIMO narrowband channels.

3.7.3 Applications to Real-World Measurement Data

In the considered examples, which illustrate the development of channel simulators for MIMO narrowband channels, we use the same measured TVFRs of the real-world channels that have been already employed in Section 3.6 for illustrating the design of the channel simulators for MIMO wideband channels.

First, we consider the convergence of the iterative parameter computation method of Subsection 3.7.2. The normalized residual approximation error norm $\|\hat{\underline{\mathbf{R}}}_{res_L}\|_F / \|\hat{\underline{\mathbf{R}}}\|_F$ versus the number of components L in (3.51) is shown for different propagation environments in Figs. 3.18 (a)–3.21 (a). For comparison reasons, Figs. 3.18 (b) – 3.21 (b) depict the normalized residual approximation error norms obtained according to (3.47) for the truncated discrete KLEs. For the case of MIMO narrowband channels, the ordered eigenvalues $\lambda_1 \geq \lambda_2 \geq \ldots$ of the matrix $\hat{\underline{\mathbf{R}}}$ defined in (3.55) are substituted into (3.47). As it can be seen from Figs. 3.18–3.21, the resulting normalized error norm is below 5% for all developed channel simulators.

Examples of the estimated TCCFs $\hat{\tilde{r}}_{t_{i_1,i_2}}[\iota]$ of the measured channels together with their respective counterparts $r_{t_{i_1,i_2}}[\iota]$ calculated for the developed channel simulators are depicted in Figs. 3.22–3.25. As can be seen from the plots, the TCCFs of all developed channel simulators closely approximate the corresponding TCCFs of the measured channels. Note that due to a small number of the TCCFs samples, $\kappa_{\max} = 5$, the parameter computation method of Subsection 3.7.2 is not able to single out the contribution of the 'measurement' noise in the estimated correlation matrix $\hat{\underline{\mathbf{R}}}$ (see Section 3.5).

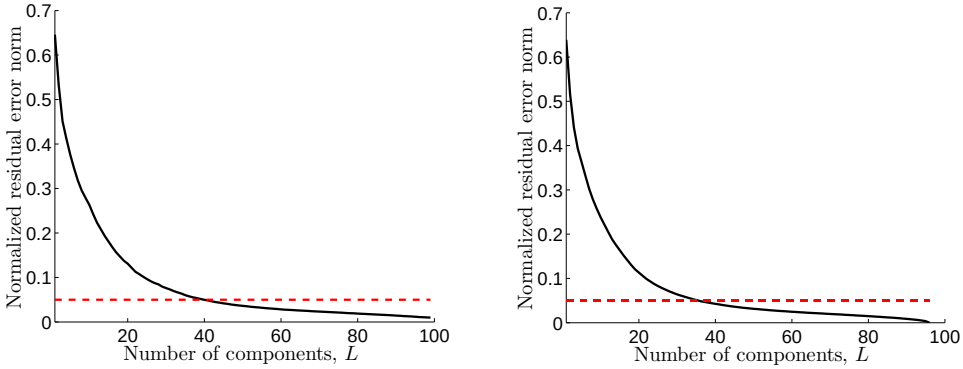

Figure 3.18: The normalized residual approximation error norm versus the number of components L for (a) the MIMO narrowband channel simulator and (b) the truncated discrete KLE (micro cell site – regular street geometry).

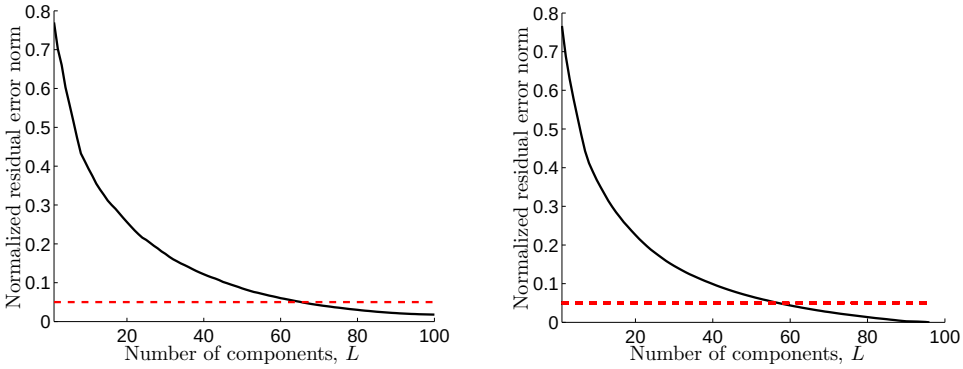

Figure 3.19: The normalized residual approximation error norm versus the number of components L for (a) the MIMO narrowband channel simulator and (b) the truncated discrete KLE (micro cell site – open market place).

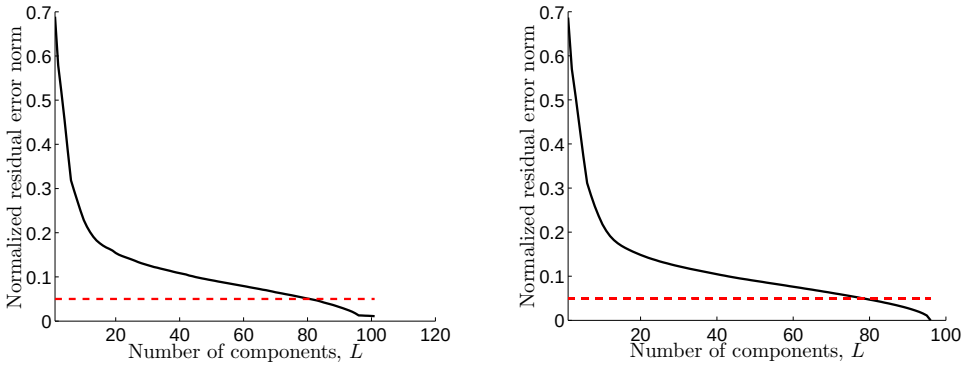

Figure 3.20: The normalized residual approximation error norm versus the number of components L for (a) the MIMO narrowband channel simulator and (b) the truncated discrete KLE (micro/pico cell site – passageway).

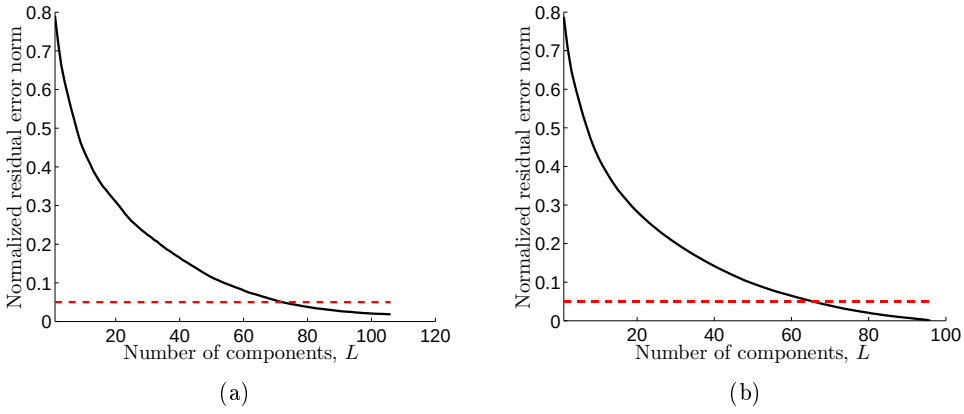

Figure 3.21: The normalized residual approximation error norm versus the number of components L for (a) the MIMO narrowband channel simulator and (b) the truncated discrete KLE (indoor cell site).

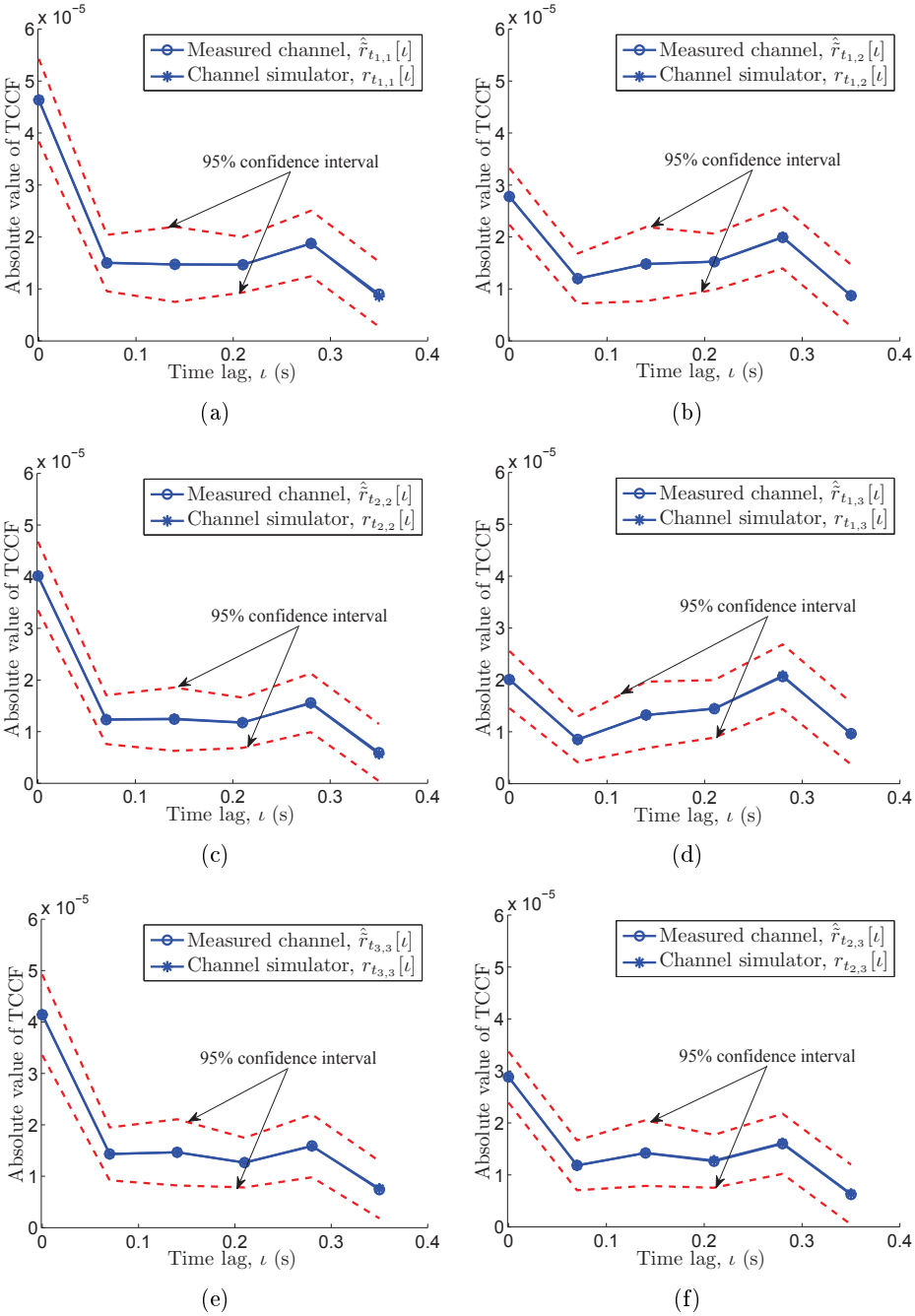

Figure 3.22: Examples of the estimated TCCFs of the physical channel and the corresponding TCCFs of the designed MIMO narrowband channel simulator (micro cell site – regular street geometry).

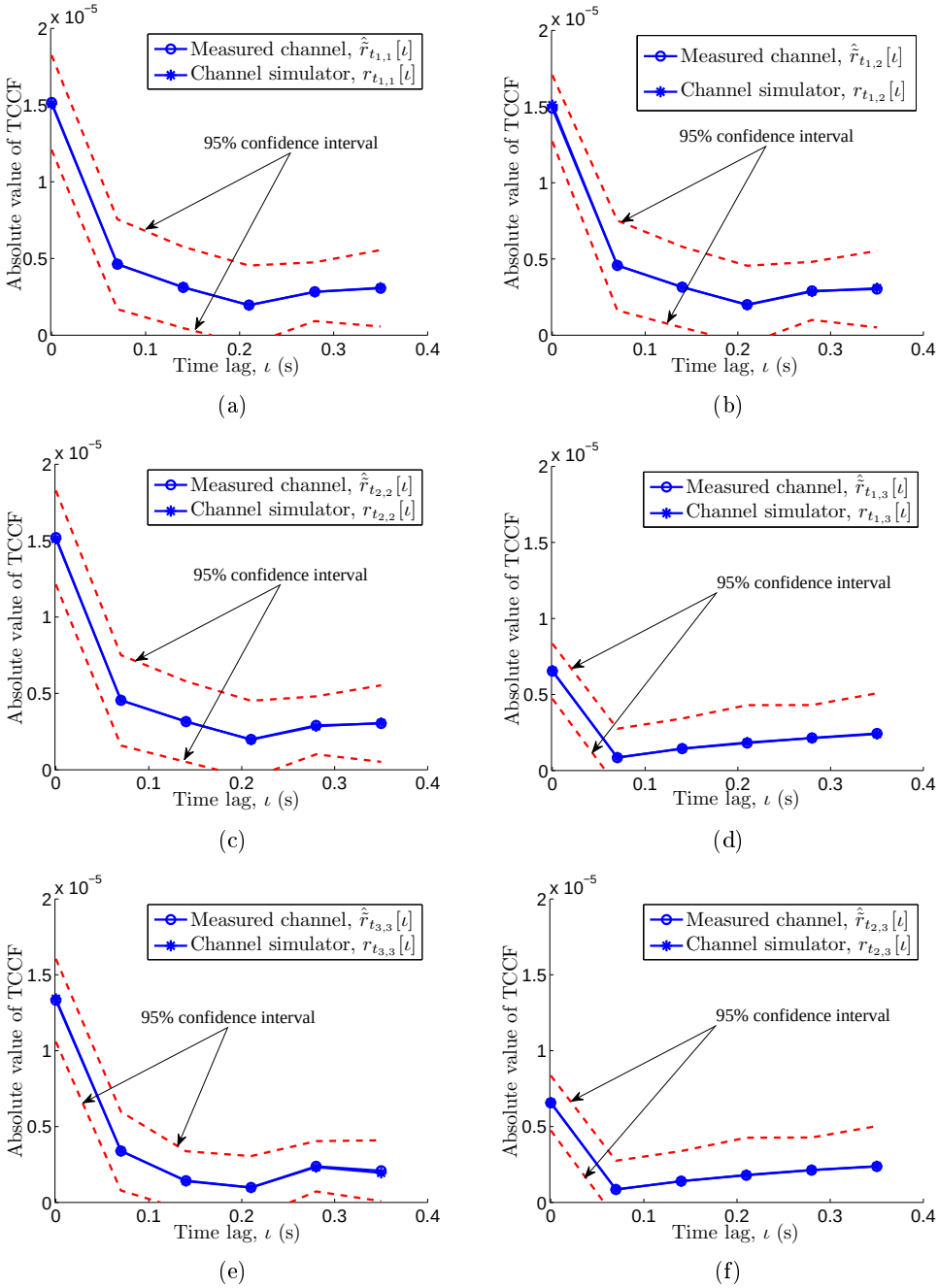

Figure 3.23: Examples of the estimated TCCFs of the physical channel and the corresponding TCCFs of the designed MIMO narrowband channel simulator (micro cell site – open market place).

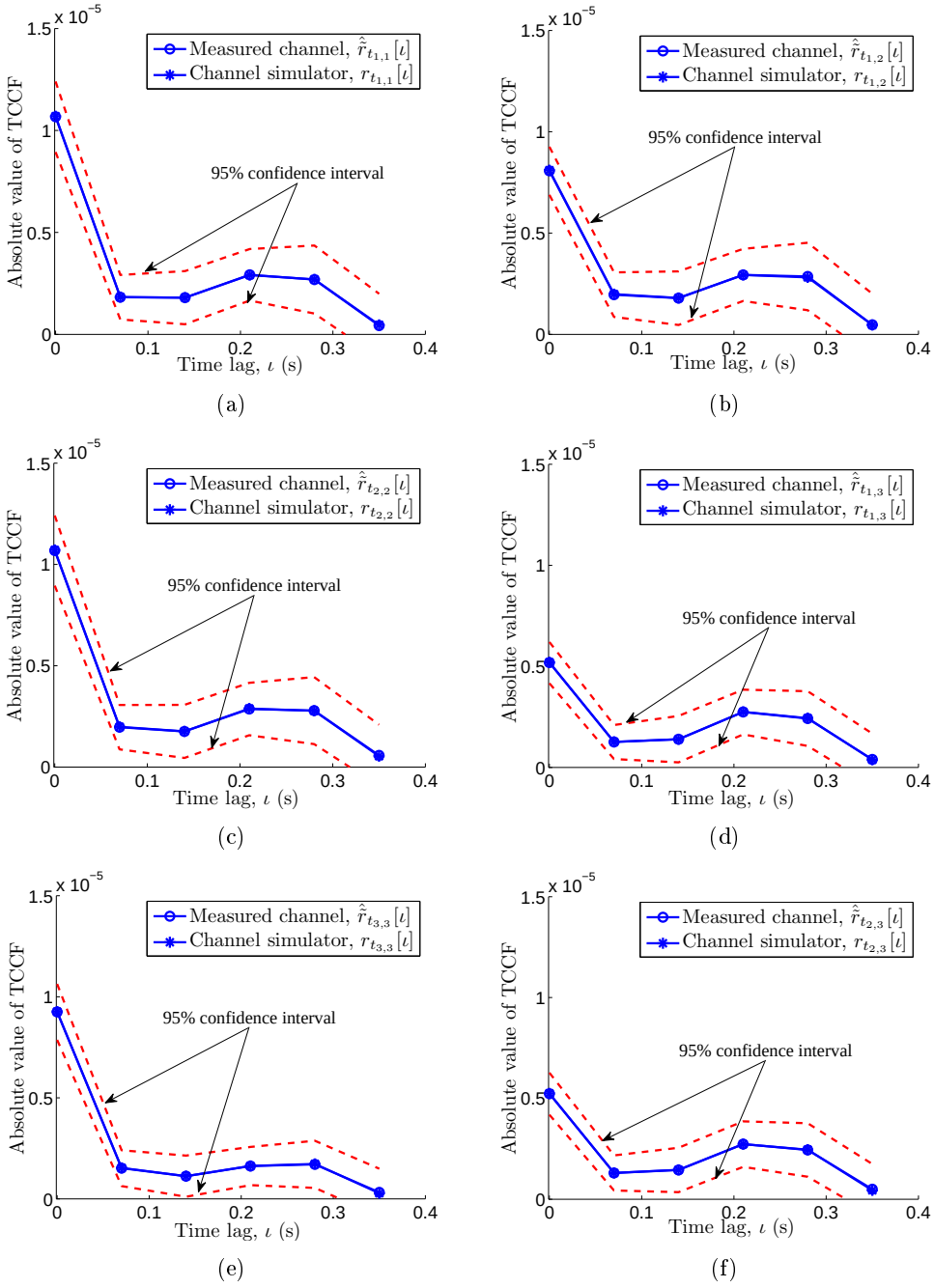

Figure 3.24: Examples of the estimated TCCFs of the physical channel and the corresponding TCCFs of the designed MIMO narrowband channel simulator (micro/pico cell site – passageway).

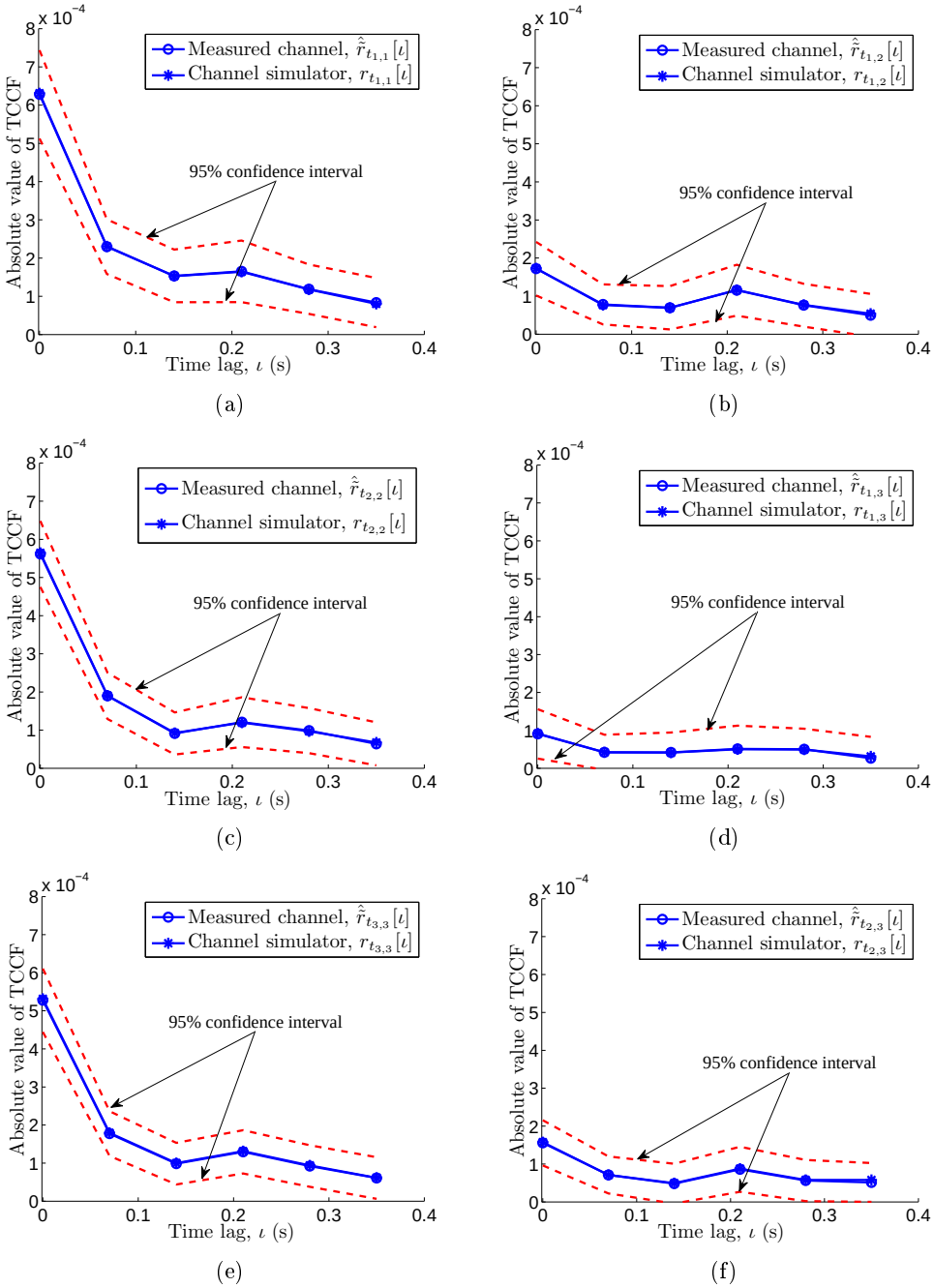

Figure 3.25: Examples of the estimated TCCFs of the physical channel and the corresponding TCCFs of the designed MIMO narrowband channel simulator (indoor cell site).

3.8 Design of Measurement-Based Stochastic Channel Simulators for SISO Wideband Channels

In this section, the channel simulation model described in Section 3.2 is adapted for synthesizing TVFRs of SISO wideband channels. Additionally, the model parameter computation method developed in Section 3.4 is modified for determining the parameters of measurement-based SISO wideband channel simulators.

It is assumed that the TVFR $\tilde{h}[m,n]$ of a real-world SISO wideband channel has been measured at discrete frequencies $f'_m = -B/2 + m\triangle f' \in [-B/2, B/2]$, $m = 0, \ldots, M-1$, and at discrete time instances $t_n = n\triangle t \in [0, T]$, $n = 0, \ldots, N-1$. We assume that the measured TVFR $\tilde{h}[m,n]$ is a 2D zero-mean complex random process, which is time- and frequency-shift invariant w.r.t. the correlation properties.

3.8.1 Stochastic Channel Simulation Model

The TVFR $h[m,n]$ of a SISO wideband wireless channel at discrete frequencies f'_m, $m = 0, \ldots, M-1$, and at discrete time instances t_n, $n = 0, \ldots, N-1$, is described as

$$h[m,n] \;=\; \sum_{l=1}^{L} c_l e^{j(2\pi f_{d_l} t_n - 2\pi f'_m \tau'_l)} U_l \tag{3.59}$$

where the simulation model parameters $\mathcal{P} = \left\{L, \{c_l\}_1^L, \{f_{d_l}\}_1^L, \{\tau'_l\}_1^L\right\}$ as well as the complex weighting coefficients U_l, $l = 1, \ldots, L$, have been defined in Section 3.2.

When the magnitudes $\{\Xi_l\}_1^L$ of the complex weighting coefficients $\{U_l\}_1^L$ are constant and all are equal to 1, the envelope PDF $p_{|h|}(x)$ of the simulated TVFR $h[m,n]$ is given by (*cf.* (3.8))

$$p_{|h|}(x) = \int_0^\infty x J_0(x\zeta) \left(\prod_{l=1}^{L} J_0(|c_l|\zeta) \right) \zeta d\zeta. \tag{3.60}$$

The correlation properties of the synthesized TVFR $h[m,n]$ are described by the temporal-frequency correlation matrix $\underline{\mathbf{R}}$ which is defined as (*cf.* (3.9))

$$\underline{\mathbf{R}} = E\left\{\mathbf{v}[m,n]\mathbf{v}^H[m,n]\right\} =$$

$$\begin{bmatrix} r[0,0] & \cdots & r[-\kappa_{\max},0] & \cdots & r[0,-\iota_{\max}] & \cdots & r[-\kappa_{\max},-\iota_{\max}] \\ \vdots & \ddots & \vdots & \ddots & \vdots & \ddots & \vdots \\ r[\kappa_{\max},0] & \cdots & r[0,0] & \cdots & r[\kappa_{\max},-\iota_{\max}] & \cdots & r[0,-\iota_{\max}] \\ \vdots & \ddots & \vdots & \ddots & \vdots & \ddots & \vdots \\ r[0,\iota_{\max}] & \cdots & r[-\kappa_{\max},\iota_{\max}] & \cdots & r[0,0] & \cdots & r[-\kappa_{\max},0] \\ \vdots & \ddots & \vdots & \ddots & \vdots & \ddots & \vdots \\ r[\kappa_{\max},\iota_{\max}] & \cdots & r[0,\iota_{\max}] & \cdots & r[\kappa_{\max},0] & \cdots & r[0,0] \end{bmatrix} \tag{3.61}$$

where the vector $\mathbf{v}[m,n]$ is defined by $\mathbf{v}[m,n] = [h[m,n] \ldots h[m-\kappa_{\max},n] \ldots h[m,n-\iota_{\max}] \ldots h[m-\kappa_{\max},n-\iota_{\max}]]^T$. By using (3.59), the correlation matrix $\underline{\mathbf{R}}$ can be written as

$$\underline{\mathbf{R}} = \sum_{l=1}^{L} c_l^2 \mathbf{R}_{t_l} \otimes \mathbf{R}_{f_l'} \tag{3.62}$$

where the matrices $\mathbf{R}_{t_l}$ and $\mathbf{R}_{f_l'}$ have been defined in (3.12) and (3.13), respectively. Note that the positive semi-definite matrix $\underline{\mathbf{R}}$ is Hermitian and block-Toeplitz.

3.8.2 Parameter Computation Method

The set of parameters $\mathcal{P}$ of the channel simulation model defined in (3.59) is determined according to the following criterion

$$\hat{\mathcal{P}} = \min_{\mathcal{P}} \left\| \hat{\underline{\mathbf{R}}} - \textstyle\sum_{l=1}^{L} c_l^2 \mathbf{R}_{t_l} \otimes \mathbf{R}_{f_l'} \right\|_F \tag{3.63}$$

where $\hat{\underline{\mathbf{R}}}$ is the estimated correlation matrix defined similarly to (3.61). The elements of the estimated matrix $\hat{\underline{\mathbf{R}}}$ are obtained as

$$\hat{\tilde{r}}[\kappa,\iota] = \frac{1}{(M-|\kappa|)(N-|\iota|)} \sum_{m=0}^{M-1-|\kappa|} \sum_{n=0}^{N-1-|\iota|} \tilde{\mathbf{h}}[m,n]\tilde{\mathbf{h}}^H[m+\kappa,n+\iota]. \tag{3.64}$$

The minimization of the Frobenius norm in (3.63) is accomplished by using a modification of the iterative algorithm proposed in Subsection 3.4.2. In particular, the matrix library $\mathcal{X}$ (see Subsection 3.4.2) consists of the matrices $\mathbf{X}_k = \mathbf{R}_{t_k} \otimes \mathbf{R}_{f_k'}$. Each member $\mathbf{X}_k$ of the matrix library is constructed by substituting the channel simulator parameters f_{d_k} and τ_k' into (3.12) and (3.13), respectively. The only required modification of the procedure described by the expressions (3.33)–(3.43) in Subsection 3.4.2, is that Equation (3.42) is to be omitted.

The performance of the modified parameter computation method is demonstrated with examples in the next subsection.

3.8.3 Applications to Real-World Measurement Data

The parameter computation method developed in Subsection 3.8.2 has been applied to the measured TVFRs of the real-world channels (see Appendix A). Since SISO wideband channels are considered in this section, only data obtained from a single pair of transmitting-receiving antennas have been used to determine the parameters of the channel simulators. The results illustrating the performance of the designed channel simulators are presented below.

The normalized residual approximation error norm $\|\hat{\underline{\mathbf{R}}}_{res_L}\|_F / \|\hat{\underline{\mathbf{R}}}\|_F$ versus the number of components L in (3.59) is shown for the designed channel simulators in Figs. 3.26–3.29. The dashed line in the figures signifies the 5% normalized error norm. Clearly, the resulting normalized error norm for all four channel simulators is below this value. For comparison reasons, Figs. 3.26–3.29 also demonstrate the corresponding normalized residual approximation error norms for the truncated discrete KLEs calculated according to (3.47).

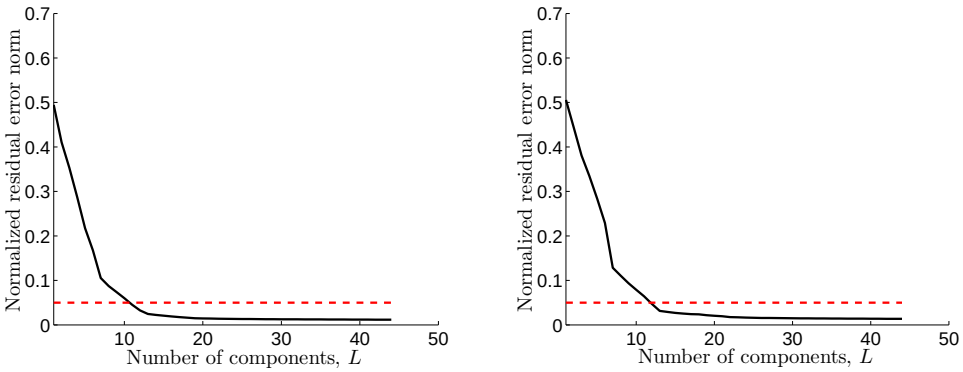

Figure 3.26: The normalized residual approximation error norm versus the number of components L for (a) the SISO wideband channel simulator and (b) the truncated discrete KLE (micro cell site – regular street geometry).

The estimated TACFs $\hat{\hat{r}}_t[\iota]$ and FACFs $\hat{\hat{r}}_{f'}[\kappa]$ of the four real-world channels and the TACFs $r_t[\iota]$ and FACFs $r_{f'}[\kappa]$ of the corresponding channel simulators are depicted in Figs. 3.30–3.33. As can be seen from the figures, noticeable discrepancies exist between the TACFs $\hat{\hat{r}}_t[\iota]$ and $r_t[\iota]$ at $\iota = 0$ as well as between the FACFs $\hat{\hat{r}}_{f'}[\kappa]$ and $r_{f'}[\kappa]$ at $\kappa = 0$ corresponding to the regular street and the passageway propagation scenarios (*cf.* the results presented in Figs. 3.3, 3.7, 3.11, 3.15).

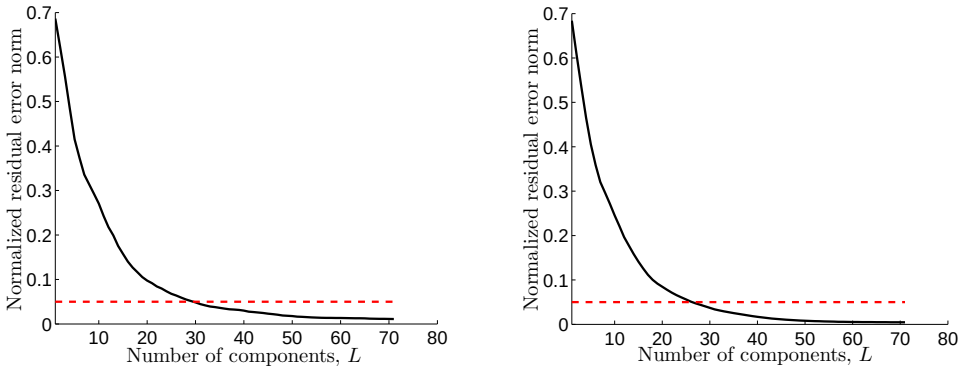

Figure 3.27: The normalized residual approximation error norm versus the number of components L for (a) the SISO wideband channel simulator and (b) the truncated discrete KLE (micro cell site – open market place).

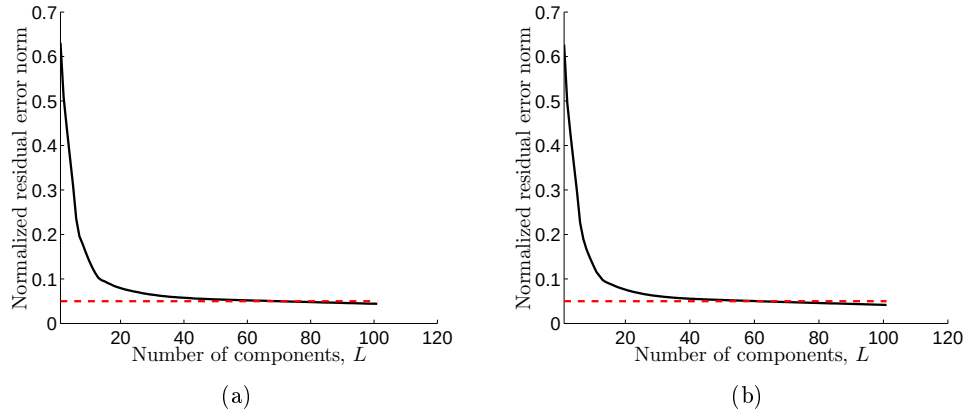

Figure 3.28: The normalized residual approximation error norm versus the number of components L for (a) the SISO wideband channel simulator and (b) the truncated discrete KLE (micro/pico cell site – passageway).

Figures 3.34–3.37 depict the envelope PDFs calculated by using (3.60) in case of the complex weighting coefficients U_l having the constant magnitudes $\Xi_l = 1$, $l = 1, \ldots, L$ (see Subsection 3.2.1). As expected, the envelope PDFs calculated by using (3.60) match the Rayleigh PDFs. Figs. 3.34–3.37 also demonstrate the empirical envelope PDFs $p_{|\tilde{h}|}(x)$ of the real-world channels.

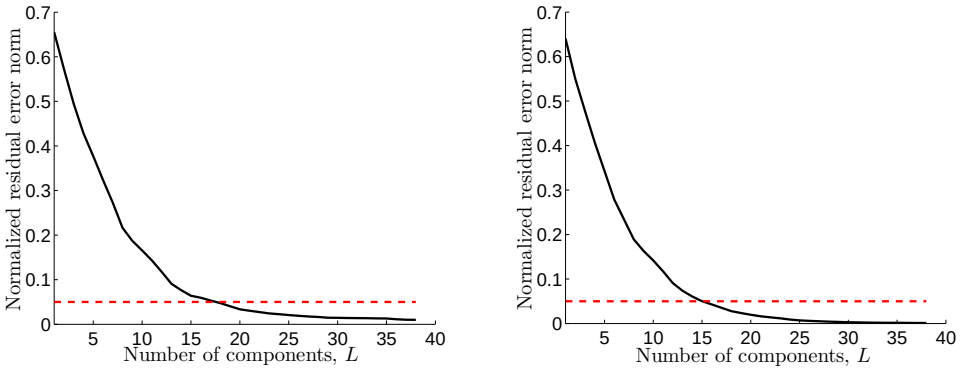

Figure 3.29: The normalized residual approximation error norm versus the number of components L for (a) the SISO wideband channel simulator and (b) the truncated discrete KLE (indoor cell site).

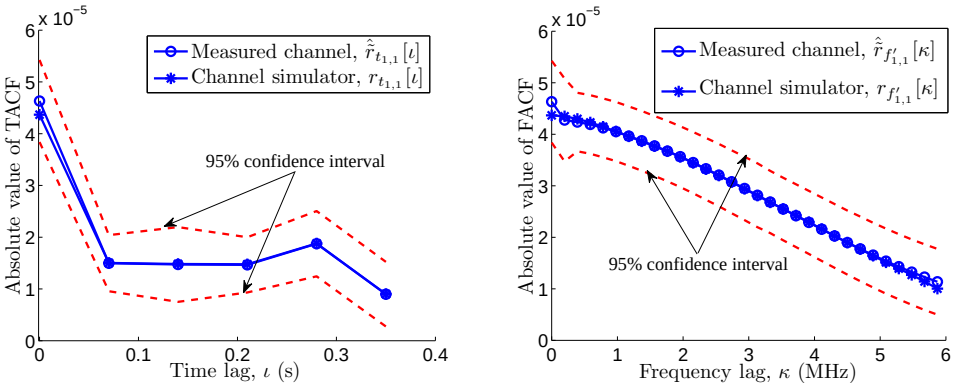

Figure 3.30: (a) The TACFs and (b) the FACFs of the real-world channel and the SISO wideband channel simulator (micro cell site – regular street geometry).

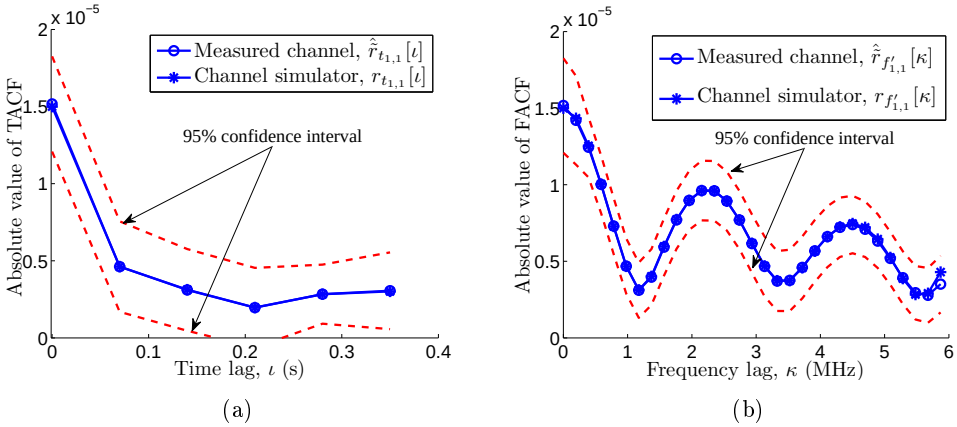

Figure 3.31: (a) The TACFs and (b) the FACFs of the real-world channel and the SISO wideband channel simulator (micro cell site – open market place).

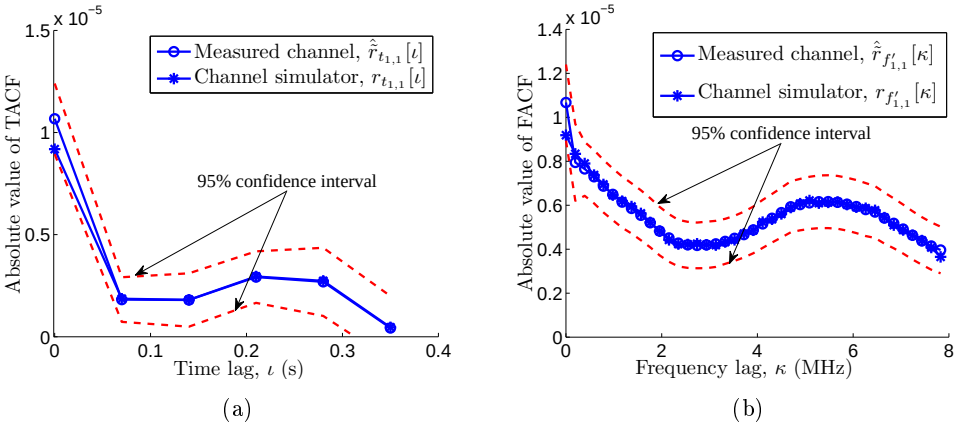

Figure 3.32: (a) The TACFs and (b) the FACFs of the real-world channel and the SISO wideband channel simulator (micro/pico cell site – passageway).

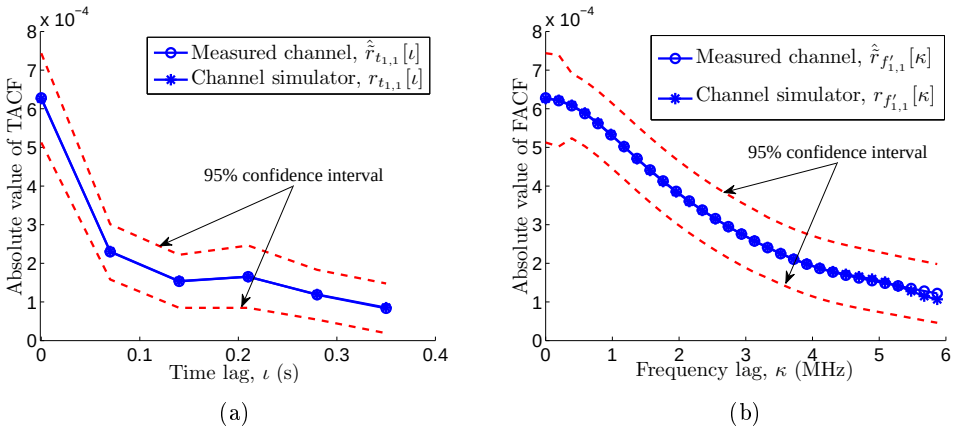

Figure 3.33: (a) The TACFs and (b) the FACFs of the real-world channel and the SISO wideband channel simulator (indoor cell site).

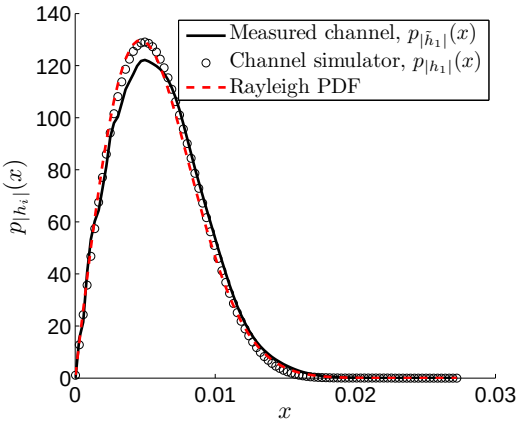

Figure 3.34: The envelope PDF $p_{|h|}(x)$ of the SISO wideband channel simulator and the empirical PDF $p_{|\tilde{h}|}(x)$ of the real-world channel (micro cell site – regular street geometry).

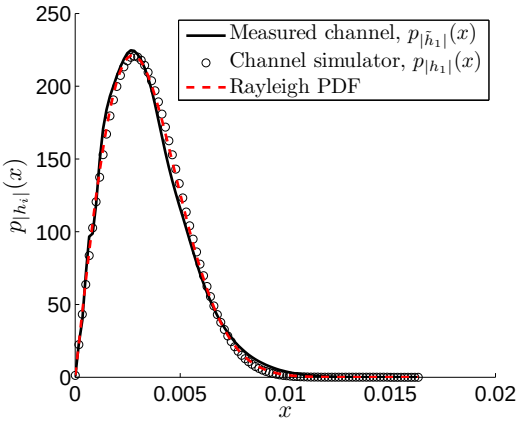

Figure 3.35: The envelope PDF $p_{|h|}(x)$ of the SISO wideband channel simulator and the empirical PDF $p_{|\tilde{h}|}(x)$ of the real-world channel (micro cell site – open market place).

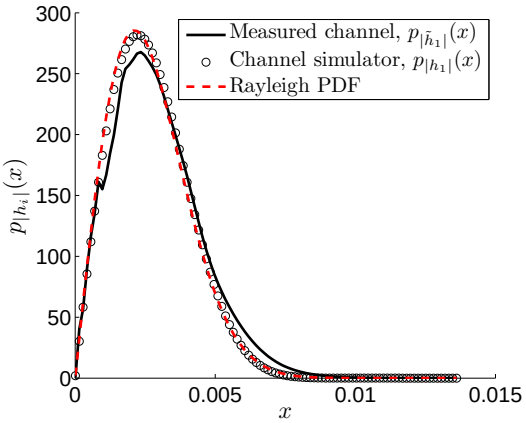

Figure 3.36: The envelope PDF $p_{|h|}(x)$ of the SISO wideband channel simulator and the empirical PDF $p_{|\tilde{h}|}(x)$ of the real-world channel (micro/pico cell site – passageway).

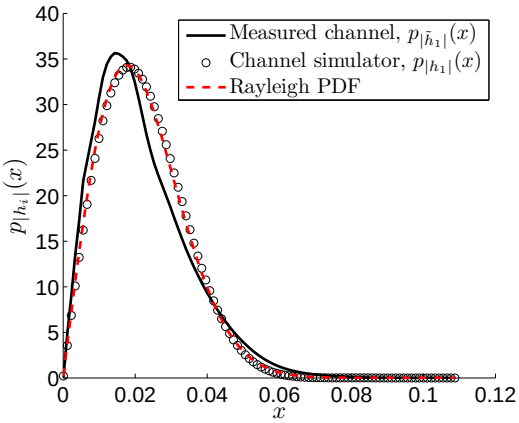

Figure 3.37: The envelope PDF $p_{|h|}(x)$ of the SISO wideband channel simulator and the empirical PDF $p_{|\tilde{h}|}(x)$ of the real-world channel (indoor cell site).

3.9 Chapter Summary

In this chapter, we have presented a method for designing measurement-based stochastic channel simulators for wireless time-variant communication channels. The method is grounded on fitting the correlation properties of a channel simulation model to the corresponding correlation properties of a prototype real-world channel. Depending on whether a channel simulator is to be designed for a MIMO/SISO or narrowband/wideband radio channel, a combination of the temporal, frequency, and spatial correlation properties is taken into consideration. It should be mentioned that the separability of the correlation properties in time, frequency, and space is not presumed.

The parameters of channel simulators are determined by using an iterative algorithm developed in this chapter. As it has been demonstrated by various examples, the proposed algorithm is able to produce acceptable results for wireless channels in different propagation environments. Additionally, the algorithm exhibits resistance to the white 'measurement' noise component possibly present in the estimated correlation matrix of a real-world channel. However, a serious drawback of the proposed parameter computation algorithm is its rather high computational complexity, especially for the case of MIMO wideband channels.

In the next chapter, we will consider a different approach to the development of measurement-based channel simulation models for time-variant wireless communication channels.

Chapter 4

Two-Dimensional Autoregressive Model for MIMO Wideband Mobile Radio Channels

4.1 Introduction

In the previous chapter, we have considered a method for designing stochastic simulation models for wireless channels, which is based on approximating the correlation properties of a real-world channel. It has been demonstrated that the method provides a close fitting between the space-time-frequency correlation matrix $\underline{\mathbf{R}}$ (3.11) of the simulation model (3.7) and the estimated space-time-frequency correlation matrix $\underline{\tilde{\mathbf{R}}}$ of a physical channel (see Subsection 3.4.1).

Due to the 'quasi-stationary' behavior of real-world channels [10], the number of samples of the measured TVFR, which are available for estimating the space-time-frequency correlation matrix $\underline{\tilde{\mathbf{R}}}$, is always confined. It means that in all practical situations, the correlation properties of a real-world channel can be reliably estimated only in a finite range of the time shifts ι and the frequency shifts κ, i.e., $|\iota| \leq \iota_{\max}$ and $|\kappa| \leq \kappa_{\max}$. Under these circumstances, it is then reasonable to question if a channel simulator developed by using the method of Chapter 3 is adequate in representing the important spectral characteristics of a real-world channel, such as the delay and the Doppler spectrum spreads. The answer to this question depends on several factors, which vary from one particular scenario to another. For example, a channel simulator developed by approximating the space-time-frequency correlation matrix $\underline{\tilde{\mathbf{R}}}$ can be adequate if the temporal and the frequency correlation functions of a prototyping physical channel decay sufficiently fast w.r.t. time shift ι and frequency shift κ, respectively. However, if this assumption is not valid, other methods for designing channel simulation models, which, perhaps, do not require estimation of the correlation properties of

a real-world channel from the measurement data, might be preferable.

In this chapter, we describe the multichannel 2D AR model for MIMO wideband mobile wireless channels [63]. In this model, radio channels between each of the transmitting and the receiving antennas are represented by 2D rational transfer functions. Our interest in the multichannel 2D AR model is motivated by the high level of flexibility intrinsic to the AR models, which has been extensively used in spectrum estimation and system identification, see, e.g. [34,64,65] and the multiple references therein. It is also important to emphasize that the multichannel 2D AR model does not presume separability of the correlation properties of a radio channel in time, frequency, and space. Some of the previous works related to the AR modeling and simulation of wireless communication channels can be found, for example, in [66–68]. Spectral estimation for multiple 2D signals using the multichannel 2D AR model is discussed in [69].

As it is shown in the following, the parameters of the multichannel 2D AR model can be estimated from the real-world measurement data by using the well-known Yule-Walker algorithm or, alternatively, by employing the prediction error minimization (PEM) algorithm. None of these methods, however, guarantees the stability of the resulting multichannel 2D AR model. Therefore, special attention is paid to the problem of the model stability, which arises when the multichannel 2D AR model is used for synthesizing the TVFRs of wireless channels.

The utility of the multichannel 2D AR model is verified by designing channel simulators based on the TVFRs of the real-world channels.

This chapter is organized as follows. In Section 4.2, we describe the multichannel 2D AR model. The model parameter estimation methods are presented in Section 4.3. In Section 4.4, we consider the stability of the multichannel 2D AR model. The method for synthesizing the TVFR of a channel in the delay-Doppler domain is presented in Section 4.5. The performance of the multichannel 2D AR model has been assessed based on the simulated MIMO channels as described in Section 4.6. The multichannel 2D AR models developed based on the measured TVFRs of the physical radio channels are presented in Section 4.7. Finally, the concluding remarks are given in Section 4.8.

4.2 The Multichannel 2D Autoregressive Model

We consider a MIMO wideband wireless channel, which contains N_T antennas at the transmitter side and N_R antennas at the receiver side. Let the matrices $\mathbf{H}[m,n]$, $m = 0,\ldots,M-1$ and $n = 0,\ldots,N-1$, be the channel TVFRs generated at discrete frequencies $f'_m = -B/2 + m\triangle f' \in [-B/2, B/2]$ and at discrete time instances $t_n = n\triangle t \in [0,T]$, $n = 0,\ldots,N-1$. As in the previous chapters, we denote the frequency bandwidth and the observation time interval as B and T,

respectively. As before, the matrices

$$\mathbf{H}[m,n] = \begin{pmatrix} H_{11}[m,n] & \dots & H_{1N_R}[m,n] \\ \vdots & \ddots & \vdots \\ H_{N_T1}[m,n] & \dots & H_{N_TN_R}[m,n] \end{pmatrix} \tag{4.1}$$

can be equivalently represented in the vectorized form as

$$\mathbf{h}[m,n] = vec(\mathbf{H}[m,n]) = \begin{pmatrix} H_{11}[m,n] \\ H_{21}[m,n] \\ \vdots \\ H_{N_TN_R}[m,n] \end{pmatrix} \tag{4.2}$$

where $\mathbf{h}[m,n] = [h_1[m,n], h_2[m,n], \dots, h_{N_TN_R}[m,n]]^T$ and $h_i[m,n]$, $i = 1, \dots, N_TN_R$, is the TVFR of the i-th subchannel.

The TVFR $h_i[m,n]$ of each subchannel is a complex zero mean 2D WSS random process (random field). Furthermore, the TVFR $\mathbf{h}[m,n]$ corresponds to the multichannel 2D AR process of the form

$$\mathbf{h}[m,n] = -\sum_{\substack{[i_1,i_2]\in\mathcal{S} \\ [i_1,i_2]\neq[0,0]}}\sum \mathbf{A}^T[i_1,i_2]\mathbf{h}[m-i_1,n-i_2] + \mathbf{u}[m,n] \tag{4.3}$$

where $\mathbf{A}[i_1,i_2]$ are complex matrix coefficients of dimensions $N_TN_R \times N_TN_R$. The vector sequence $\mathbf{u}[m,n]$ is a complex multichannel 2D white noise with the cross-correlation matrix $\mathbf{R}_u[k,l]$ defined as

$$\mathbf{R}_u[k,l] = E\{\mathbf{u}[m,n]\mathbf{u}^H[m+k,n+l]\} = \mathbf{P}_u\delta[k,l] \tag{4.4}$$

where $\delta[k,l]$ is the 2D Dirac delta function and $\mathbf{P}_u$ denotes the noise delay-Doppler PSD matrix[1], which is constant.

We assume that the channel model (4.3) is recursively computable (causal) [70]. The two most commonly used support regions $\mathcal{S}$ that guarantee the recursive computability of the TVFR $\mathbf{h}[m,n]$ are the finite nonsymmetric half-plane (NSHP) and the finite quarter plane (QP) supports [64]. In the following, we focus our attention on the multichannel 2D AR models (4.3) with the finite QP support region $\mathcal{S}_{QP}$ defined as

$$\mathcal{S}_{QP} = \{[i_1,i_2] : 0 \le i_1 \le p_1, 0 \le i_2 \le p_2\}. \tag{4.5}$$

[1]The diagonal elements of the delay-Doppler PSD matrix are the delay-Doppler spectra of the individual sub-channels $h_i[m,n]$ (4.2) at the certain delay and Doppler frequency. The off-diagonal elements correspond to the samples of the cross-subchannel delay-Doppler spectra.

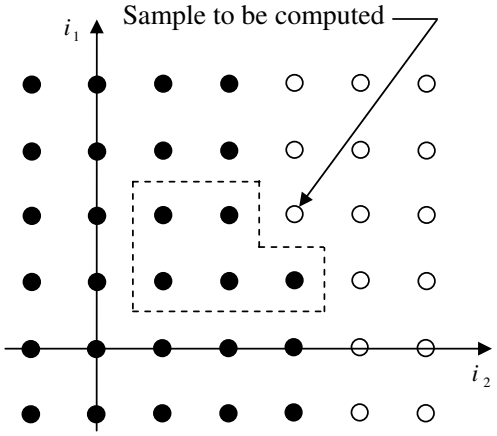

Figure 4.1: The support region $\mathcal{S}_{QP}$ for a multichannel 2D AR(1,2) model.

where (p_1,p_2) is the order of the multichannel 2D AR model, henceforth designated AR(p_1,p_2). As an illustrative example, the support region $\mathcal{S}_{QP}$ for a multichannel 2D AR(1,2) model is shown in Fig. 4.1.

Using the relationship between the input PSD and the output PSD of a linear shift-invariant (LSI) multichannel 2D filter (see, e.g., [34,69]), we define the delay-Doppler PSD $\mathbf{P}_h(\tau', f_d)$ of the multichannel 2D AR model as

$$\mathbf{P}_h(\tau', f_d) = \mathcal{H}(\tau', f_d)\mathbf{P}_u\mathcal{H}^H(\tau', f_d)\triangle f'\triangle t \tag{4.6}$$

where

$$\mathcal{H}(\tau', f_d) = \left(\mathbf{I} + \sum_{\substack{i_1=0 \\ [i_1,i_2]\neq[0,0]}}^{p_1}\sum_{i_2=0}^{p_2} \mathbf{A}[i_1, i_2]e^{-j2\pi(\tau' i_1\triangle f' + f_d i_2\triangle t)}\right)^{-1} \tag{4.7}$$

and τ' and f_d are the propagation delay and the Doppler frequency, respectively. The matrix $\mathbf{I}$ is the identity matrix.

4.3 Estimation of the Model Parameters

Suppose that the sampled TVFR $\tilde{\mathbf{H}}[m, n]$ of a real-world MIMO channel, obtained from a channel sounder during a measurement campaign, is a multichannel 2D AR process.

Assume that the order (p_1,p_2) of the multichannel 2D AR(p_1,p_2) model (4.3) has been determined (see Subsection 4.7.1). The parameters of the model, i.e., the matrix coefficients $\mathbf{A}[i_1, i_2]$ and the noise PSD matrix $\mathbf{P}_u$, are to be estimated from the measured TVFR $\tilde{\mathbf{h}}[m, n]$, which is a vectorized representation of the sampled TVFR $\tilde{\mathbf{H}}[m, n]$ defined similar to (4.2).

$$\underbrace{\begin{bmatrix} \tilde{\mathbf{R}}_h[0,0] & \cdots & \tilde{\mathbf{R}}_h[-p_1,0] & \cdots & \tilde{\mathbf{R}}_h[0,-p_2] & \cdots & \tilde{\mathbf{R}}_h[-p_1,-p_2] \\ \vdots & \ddots & \vdots & \ddots & \vdots & \ddots & \vdots \\ \tilde{\mathbf{R}}_h[p_1,0] & \cdots & \tilde{\mathbf{R}}_h[0,0] & \cdots & \tilde{\mathbf{R}}_h[p_1,-p_2] & \cdots & \tilde{\mathbf{R}}_h[0,-p_2] \\ \vdots & \ddots & \vdots & \ddots & \vdots & \ddots & \vdots \\ \tilde{\mathbf{R}}_h[0,p_2] & \cdots & \tilde{\mathbf{R}}_h[-p_1,p_2] & \cdots & \tilde{\mathbf{R}}_h[0,0] & \cdots & \tilde{\mathbf{R}}_h[-p_1,0] \\ \vdots & \ddots & \vdots & \ddots & \vdots & \ddots & \vdots \\ \tilde{\mathbf{R}}_h[p_1,p_2] & \cdots & \tilde{\mathbf{R}}_h[0,p_2] & \cdots & \tilde{\mathbf{R}}_h[p_1,0] & \cdots & \tilde{\mathbf{R}}_h[0,0] \end{bmatrix}}_{\underline{\tilde{\mathbf{R}}}_h} \times$$

$$\times \begin{bmatrix} \mathbf{I} \\ \vdots \\ \mathbf{A}^T[p_1,0] \\ \vdots \\ \mathbf{A}^T[0,p_2] \\ \vdots \\ \mathbf{A}^T[p_1,p_2] \end{bmatrix} = \begin{bmatrix} \mathbf{P}_u \\ \vdots \\ \mathbf{0} \\ \vdots \\ \mathbf{0} \\ \vdots \\ \mathbf{0} \end{bmatrix} \quad (4.9)$$

4.3.1 Yule-Walker Normal Equations

The cross-correlation matrix $\tilde{\mathbf{R}}_h[\kappa,\iota]$ of the TVFR $\tilde{\mathbf{h}}[m,n]$ can be defined as follows

$$\tilde{\mathbf{R}}_h[\kappa,\iota] = E\{\tilde{\mathbf{h}}[m,n]\tilde{\mathbf{h}}^H[m+\kappa,n+\iota]\}. \quad (4.8)$$

Substituting (4.3), (4.4) into (4.8) and noting that the multichannel 2D AR(p_1,p_2) model (4.3) is casual we obtain a system of the Yule-Walker normal equations (4.9). The matrix coefficients $\mathbf{A}[i_1,i_2]$ and the noise delay-Doppler PSD matrix $\mathbf{P}_u$ that solve the normal equations (4.9) can be efficiently determined by the method described, e.g., in [71].

In practice, the matrix $\underline{\tilde{\mathbf{R}}}_h$ in (4.9) has to be estimated from the finite-sample vector sequence $\tilde{\mathbf{h}}[m,n]$ implying the latter is ergodic. The suitable estimator of the matrix $\underline{\tilde{\mathbf{R}}}_h$ is given by

$$\hat{\underline{\tilde{\mathbf{R}}}}_h = \frac{1}{NM}\sum_{m=0}^{M-1}\sum_{n=0}^{N-1}\tilde{\mathbf{v}}[m,n]\tilde{\mathbf{v}}^H[m,n] \quad (4.10)$$

where

$$\tilde{\mathbf{v}}[m,n] = \begin{bmatrix} \tilde{\mathbf{h}}[m,n] \\ \vdots \\ \tilde{\mathbf{h}}[m-p_1,n] \\ \vdots \\ \tilde{\mathbf{h}}[m,n-p_2] \\ \vdots \\ \tilde{\mathbf{h}}[m-p_1,n-p_2] \end{bmatrix}. \tag{4.11}$$

Note that the components of the vector $\tilde{\mathbf{v}}[m,n]$ in (4.11) with the negative indices have to be set to zero, i.e., $\tilde{\mathbf{h}}[m-p_1,n-p_2]=0$ for $m<p_1$ and/or $n<p_2$.

The matrix $\hat{\underline{\underline{\mathbf{R}}}}_h$ (4.10) is Hermitian and positive semidefinite. In general, the matrix coefficients $\mathbf{A}[i_1,i_2]$ and the noise delay-Doppler PSD matrix $\mathbf{P}_u$ cannot be determined uniquely even if all the eigenvalues of the matrix $\hat{\underline{\underline{\mathbf{R}}}}_h$ are greater than zero. The reason is that the number of the unknown complex parameters in (4.9) is equal to $(p_1p_2+p_1+p_2)N_T^2N_R^2$ and is greater than the number of the known independent complex elements of the matrix $\hat{\underline{\underline{\mathbf{R}}}}_h$, which is $(2p_1p_2+p_1+p_2+1)N_TN_R$ (see also [65]).

4.3.2 Prediction Error Minimization

The PEM method is based on the strong relationship existing between the AR modeling and the linear prediction problem [65].

The linear forward predictor of $\tilde{\mathbf{h}}[m,n]$ is defined as

$$\hat{\tilde{\mathbf{h}}}[m,n] = -\sum_{\substack{[i_1,i_2]\in\mathcal{S}_{QP} \\ [i_1,i_2]\neq[0,0]}}\sum \mathbf{A}^T[i_1,i_2]\tilde{\mathbf{h}}[m-i_1,n-i_2] \tag{4.12}$$

with the prediction error given by

$$\tilde{\mathbf{e}}[m,n] = \tilde{\mathbf{h}}[m,n] - \hat{\tilde{\mathbf{h}}}[m,n]. \tag{4.13}$$

Consequently, the prediction error power matrix can be written as

$$\tilde{\mathbf{\Sigma}} = E\{\tilde{\mathbf{e}}[m,n]\tilde{\mathbf{e}}^H[m,n]\}. \tag{4.14}$$

For the finite-sample vector sequence $\tilde{\mathbf{h}}[m,n]$ the estimator of the matrix $\tilde{\mathbf{\Sigma}}$ takes the form

$$\hat{\tilde{\mathbf{\Sigma}}} = \frac{1}{(M-p_1)(N-p_2)}(\tilde{\mathbf{Z}}+\tilde{\mathbf{Y}}\mathbf{X})^H(\tilde{\mathbf{Z}}+\tilde{\mathbf{Y}}\mathbf{X}) \tag{4.15}$$

where the matrices $\tilde{\mathbf{Z}}$, $\tilde{\mathbf{Y}}$, and $\mathbf{X}$ are defined below

$$\tilde{\mathbf{Z}} = \begin{bmatrix} \tilde{\mathbf{h}}^T[M-1, N-1] \\ \tilde{\mathbf{h}}^T[M-2, N-1] \\ \vdots \\ \tilde{\mathbf{h}}^T[p_1, p_2] \end{bmatrix} \tag{4.16}$$

$$\tilde{\mathbf{Y}} = \begin{bmatrix} \tilde{\mathbf{h}}^T[M-2, N-1] & \cdots & \tilde{\mathbf{h}}^T[M-p_1-1, N-p_2-1] \\ \tilde{\mathbf{h}}^T[M-3, N-1] & \cdots & \tilde{\mathbf{h}}^T[M-p_1-2, N-p_2-1] \\ \vdots & \ddots & \vdots \\ \tilde{\mathbf{h}}^T[p_1-1, p_2] & \cdots & \tilde{\mathbf{h}}^T[0,0] \end{bmatrix} \tag{4.17}$$

$$\mathbf{X} = \begin{bmatrix} \mathbf{A}^T[1,0] \\ \mathbf{A}^T[2,0] \\ \vdots \\ \mathbf{A}^T[p_1, p_2] \end{bmatrix}. \tag{4.18}$$

The matrix coefficients $\mathbf{A}[i_1, i_2]$ of the multichannel 2D AR(p_1,p_2) model can be estimated by minimizing the sum of the estimated prediction error powers, i.e.,

$$\left\{\hat{\mathbf{A}}[i_1, i_2]\right\}_{\substack{[i_1,i_2]\in\mathcal{S}_{QP}, \\ [i_1,i_2]\neq[0,0]}} = \min_{\{\mathbf{A}[i_1,i_2]\}} \left\{ trace\left(\hat{\tilde{\mathbf{\Sigma}}}\right)\right\}. \tag{4.19}$$

This is a linear least-squares estimation problem. The estimate of the matrix $\mathbf{X}$ (4.18) that minimizes (4.19) can be written as

$$\hat{\mathbf{X}} = -\tilde{\mathbf{Y}}^{\dagger}\tilde{\mathbf{Z}} \tag{4.20}$$

where $\tilde{\mathbf{Y}}^{\dagger}$ is the Moore-Penrose pseudoinverse of the matrix $\tilde{\mathbf{Y}}$ [58].

The estimated noise delay-Doppler PSD matrix $\hat{\mathbf{P}}_u$ is equal to the residual prediction error power matrix $\hat{\tilde{\mathbf{\Sigma}}}_{\min}$, obtained by substituting the solution $\hat{\mathbf{X}}$ (4.20) into (4.15).

4.4 Model Stability

The channel model (4.3) is stable when the following condition is fulfilled [64]

$$\det\left(\mathbf{I}+\sum_{\substack{i_1=0\\[i_1,i_2]\neq[0,0]}}^{p_1}\sum_{i_2=0}^{p_2}\mathbf{A}[i_1,i_2]z_1^{i_1}z_2^{i_2}\right)\neq 0, \quad \text{for all } \{(z_1,z_2):|z_1|\leq 1,|z_2|\leq 1\} \tag{4.21}$$

where z_1 and z_2 are complex variables.

Both, the Yule-Walker and the PEM methods, described in Section 4.3, do not guarantee the stability of the resulting multichannel 2D AR(p_1,p_2) model. Additionally, the stability test (4.22) is almost useless in practice due to the heavy computational load.

4.4.1 State-Space Representation of the Multichannel 2D AR Model

In the past years, a number of stability tests has been proposed for 2D recursive filters in state-space form [72, 73]. An attractive feature of the state-space representation is that it can be extended to *multichannel* 2D recursive filters, i.e., to the multichannel 2D AR(p_1,p_2) model (4.3).

In this section, we consider the 2D state-space model representation developed by Roesser [74]. The Roesser's state-space model can be formulated as follows [70]

$$\begin{aligned}\begin{bmatrix}\mathbf{x}_h[m+1,n]\\ \mathbf{x}_v[m,n+1]\end{bmatrix} &= \begin{bmatrix}\mathbf{A}_{11} & \mathbf{A}_{12}\\ \mathbf{A}_{21} & \mathbf{A}_{22}\end{bmatrix}\begin{bmatrix}\mathbf{x}_h[m,n]\\ \mathbf{x}_v[m,n]\end{bmatrix}+\begin{bmatrix}\mathbf{B}_1\\ \mathbf{B}_2\end{bmatrix}\mathbf{u}[m,n]\\ \mathbf{h}[m,n] &= \begin{bmatrix}\mathbf{C}_1 & \mathbf{C}_2\end{bmatrix}\begin{bmatrix}\mathbf{x}_h[m,n]\\ \mathbf{x}_v[m,n]\end{bmatrix}+\mathbf{D}\mathbf{u}[m,n]\end{aligned} \tag{4.22}$$

where $\mathbf{x}_h$ and $\mathbf{x}_v$ are the model state variable vectors. The model input $\mathbf{u}[m,n]$ and the model output $\mathbf{h}[m,n]$ in (4.22) are the same processes $\mathbf{u}[m,n]$ and $\mathbf{h}[m,n]$ as in (4.3).

The two possible candidates for the model stability test of the Roesser's state-space model are presented below [73].

The Roesser's state-space model (4.22) is bounded input bounded output (BIBO) stable if

$$\begin{cases}\mathbf{A}_{11} & \text{is stable}\\ \mathbf{A}_{22}+\mathbf{A}_{21}(z_1\mathbf{I}-\mathbf{A}_{11})^{-1}\mathbf{A}_{12},|z_1|=1 & \text{is stable}\end{cases} \tag{4.23}$$

where a square matrix, e.g., $\mathbf{A}_{11}$, is stable if the maximum magnitude of its eigenvalues is less than 1. The second possible group of stability criteria is defined as

$$\begin{cases} \|\mathbf{A}_{11}\|_2 < 1 \\ \|\mathbf{A}_{22}\|_2 + \|\mathbf{A}_{21}\|_2(1 - \|\mathbf{A}_{11}\|_2)^{-1}\|\mathbf{A}_{12}\|_2 < 1 \end{cases} \tag{4.24}$$

where $\|\cdot\|_2$ is equal to the largest singular value of the matrix.

The criteria in (4.23) are sufficient and necessary conditions for the BIBO stability of the model (4.22). On the other hand, the criteria in (4.24) are sufficient but not necessary [73]. The experimental results show that the BIBO stability conditions (4.23) are more suitable for the stabilization procedure presented below, in spite of the obvious computational advantages associated with the stability test implemented according to the criteria in (4.24).

To be able to apply the stability test (4.23), the multichannel 2D AR(p_1,p_2) model (4.3) has to be *converted* to the Roesser's state-space representation (4.22). The conversion between the model representations can be done in at least two ways. As an example, the two possible realizations of a simple multichannel 2D AR(1,1) model are presented in Fig. 4.2. The shift operators are indicated in the flowgraphs as z_1^{-1} and z_2^{-1}. The state variables in $\mathbf{x}_h$ and $\mathbf{x}_v$ are assigned to the outputs of the shift operators. The matrix coefficients $\mathbf{A}[i_1, i_2]$, $i_1, i_2 = \{0, 1\}$, are shown in Fig. 4.2 along the appropriate branches.

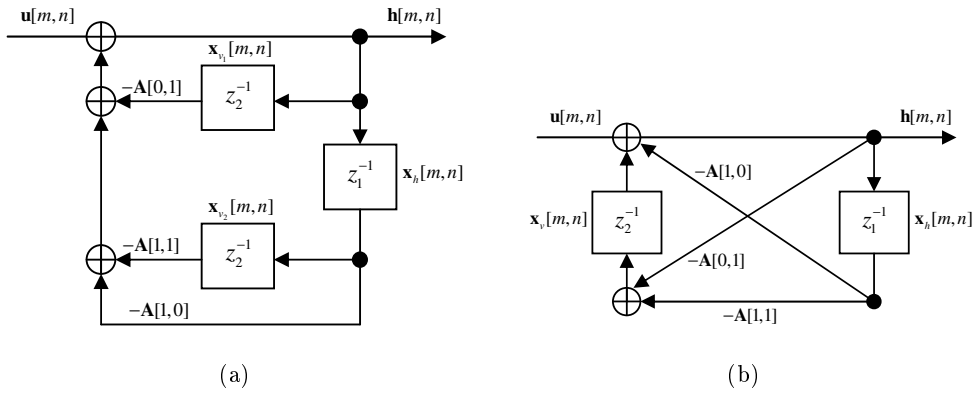

Figure 4.2: Two possible flowgraphs representing the multichannel 2D AR(1,1) model.

Considering the computational load required to test the stability of the model, it is desirable to minimize the number of state variables, i.e., the number of the shift operators in a flowgraph. For example, the minimal state-space realization of the model (4.22) corresponding to the multichannel 2D AR(1,1) model is shown in Fig. 4.2 (b).

4.4.2 Stabilization Procedure

In this subsection, we describe a procedure that can be applied to resolve the possible instability of the multichannel 2D AR(p_1,p_2) model (4.3).

Step 1. Estimate the matrix coefficients $\hat{\mathbf{A}}^{(0)}[i_1, i_2]$ and the noise delay-Doppler PSD matrix $\hat{\mathbf{P}}_u^{(0)}$ either by solving the Yule-Walker normal equations of Subsection 4.3.1 or by minimizing the sum of the estimated prediction error powers in (4.19) (see Subsection 4.3.2).

Step 2. Calculate the matrices $\mathbf{A}_{11}$, $\mathbf{A}_{12}$, $\mathbf{A}_{21}$, and $\mathbf{A}_{22}$ of the Roesser's state-space representation (4.22). If the BIBO stability conditions in (4.23) are satisfied, skip the next steps.

Step 3. Formulate the minimization problem (4.19) under constrains (4.23) as a multi-objective optimization problem that can be solved by the goal-attainment method [75], i.e.,

$$\min_{\gamma \in \mathcal{R}} \gamma \tag{4.25}$$

subject to

$$\begin{aligned} &trace\left(\hat{\hat{\mathbf{\Sigma}}}\right) - w_1\gamma \leq trace\left(\hat{\mathbf{P}}_{uu}^{(0)}\right) \\ &\rho(\mathbf{A}_{11}) - w_2\gamma \leq 1 \\ &\rho(\mathbf{A}_{22} + \mathbf{A}_{21}(z_1\mathbf{I} - \mathbf{A}_{11})^{-1}\mathbf{A}_{12}) - w_3\gamma \leq 1, |z_1| = 1 \end{aligned}$$

where $\rho(\cdot)$ denotes the spectral radius of a square matrix [58], $\{w_1, w_2, w_3\}$ are the weighting coefficients that signify the relative trade-off between the objectives, and γ is a scalar parameter (see, e.g, [75, 76]). Note that the matrices $\hat{\mathbf{\Sigma}}$, $\mathbf{A}_{11}$, $\mathbf{A}_{12}$, $\mathbf{A}_{21}$, and $\mathbf{A}_{22}$ in (4.25) are functions of the matrix coefficients $\mathbf{A}[i_1, i_2]$, $[i_1, i_2] \in \mathcal{S}_{QP}, [i_1, i_2] \neq [0, 0]$. The solution to the multi-objective minimization problem formulated in (4.25) can be found by applying the `fgoalattain` function implemented in MATLAB. The estimates $\hat{\mathbf{A}}^{(0)}[i_1, i_2]$ obtained at Step 1 can be used as the initial parameter values.

Step 4. The matrix coefficients $\hat{\mathbf{A}}[i_1, i_2]$ obtained in Step 3 are substituted into (4.19) to get the estimate of the matrix $\hat{\mathbf{X}}$. Finally, the estimate of the noise delay-Doppler PSD matrix $\hat{\mathbf{P}}_u$ is equal to the residual prediction error power matrix $\hat{\hat{\mathbf{\Sigma}}}_{\min}$ calculated by substituting the matrix $\hat{\mathbf{X}}$ into (4.15) (see Section 4.3).

A note regarding Step 2 and Step 3 of the algorithm described above is required. For the second stability criterion in (4.23) the largest magnitude eigenvalue of the corresponding matrix has to be calculated at the infinite number of points z_1 along the unit circle, $|z_1| = 1$. The conducted simulations suggest that a limited number of points z_1 is sufficient to check the stability of the multichannel 2D AR(p_1,p_2) model.

4.5 Synthesis of the Time-Variant Frequency Response in the Delay-Doppler Domain

Channel simulators based on the 2D AR(p_1,p_2) model represented in the form of (4.3) or in the state-space form (4.22) allow recursive computation of the TVFR $\mathbf{h}[m,n]$. Although computationally efficient, the model representations (4.3) and (4.22) require stability of the multichannel 2D AR(p_1,p_2) model. If the multichannel 2D AR(p_1,p_2) model is unstable, the stabilization procedure presented in Subsection 4.4.2 can be applied. However, the computational load associated with Step 3 of the stabilization algorithm quickly increases as the order (p_1,p_2) of the model grows.

On the other hand, the lack of guaranteed stability of the multichannel 2D AR(p_1,p_2) is not a serious drawback for estimating the delay-Doppler PSD $\mathbf{P}_h(\tau', f_d)$ of a radio channel (see, e.g., the discussions in [65, Chapter 3] and [64, Chapter 15]). This observation underlies the method for generating the TVFR $\mathbf{h}[m,n]$ in the delay-Doppler domain presented below.

Let a complex zero-mean multichannel 2D white noise $\mathbf{w}[m,n]$, with the constant delay-Doppler PSD $\mathbf{P}_w(\tau', f_d) = \mathbf{I}$, be an input to the LSI shaping filter represented by its delay-Doppler transfer function $\mathbf{\Psi}(\tau', f_d)$, which is a matrix of dimensions $N_T N_R \times N_T N_R$ at every propagation delay τ' and Doppler frequency f_d.

The delay-Doppler PSD $\mathbf{P}_y(\tau', f_d)$ of the signal $\mathbf{y}[m,n]$ at the output of the filter is given by (*cf.* (4.6))

$$\mathbf{P}_y(\tau', f_d) = \mathbf{\Psi}(\tau', f_d)\mathbf{P}_w\mathbf{\Psi}^H(\tau', f_d) = \mathbf{\Psi}(\tau', f_d)\mathbf{\Psi}^H(\tau', f_d). \tag{4.26}$$

Assuming that $\mathbf{\Psi}(\tau', f_d) = \mathbf{P}_h^{1/2}(\tau', f_d)$, where the square root of the delay-Doppler PSD matrix $\mathbf{P}_h(\tau', f_d)$ (4.6) is obtained by applying the singular value decomposition[2] (SVD) [58], the delay-Doppler PSD of the signal at the output of the filter $\mathbf{P}_y(\tau', f_d)$ (4.26) is equal to $\mathbf{P}_h(\tau', f_d)$.

A practical approach to generating the TVFR $\mathbf{h}[m,n]$ of a wireless channel is by implementing the shaping filter in the delay-Doppler domain as follows

$$\begin{aligned}\mathbf{h}[m,n] &= \sum_{k=0}^{M-1}\sum_{l=-N/2}^{N/2}\left[\frac{1}{M\triangle f' N\triangle t}\mathbf{P}_h\left(\frac{k}{M\triangle f'}, \frac{l}{N\triangle t}\right)\right]^{1/2} \\ &\quad\times\ \mathbf{W}\left(\frac{k}{M\triangle f'}, \frac{l}{N\triangle t}\right) e^{j2\pi(\frac{km}{M}+\frac{ln}{N})}\end{aligned} \tag{4.27}$$

where the discrete Fourier transform (DFT) $\mathbf{W}\left(\frac{k}{M\triangle f'}, \frac{l}{N\triangle t}\right)$ of the noise signal

[2]Recall that the delay-Doppler PSD matrix $\mathbf{P}_h(\tau', f_d)$ (4.6) is Hermitian.

$\mathbf{w}[m,n]$ at the discrete delays $\frac{k}{M\triangle f'}$, $k=0,\ldots,M-1$, and at the discrete Doppler frequencies $\frac{l}{N\triangle t}$, $l=-N/2,\ldots,N/2$, is given by

$$\mathbf{W}\left(\frac{k}{M\triangle f'},\frac{l}{N\triangle t}\right)=\frac{1}{\sqrt{MN}}\sum_{m=0}^{M-1}\sum_{n=0}^{N-1}\mathbf{w}[m,n]e^{-j2\pi(\frac{km}{M}+\frac{ln}{N})}. \tag{4.28}$$

By construction, the TVFR $\mathbf{h}[m,n]$ in (4.27) is a complex multichannel 2D random process with the delay-Doppler PSD approximating the desired $\mathbf{P}_h(\tau',f_d)$ given by (4.6). Note that the TVFR $\mathbf{h}[m,n]$ generated according to (4.27) is periodic w.r.t. frequency f' and time t with the periods $M\triangle f'$ and $N\triangle t$, respectively.

The agreement between the delay-Doppler PSD of the random process $\mathbf{h}[m,n]$ (4.27) and the desired delay-Doppler PSD $\mathbf{P}_h(\tau',f_d)$ can be improved by substituting $\mathbf{W}\left(\frac{k}{M\triangle f'},\frac{l}{N\triangle t}\right)=e^{j\boldsymbol{\theta}[k,l]}$ into (4.27) instead of (4.28). The vectors $\boldsymbol{\theta}[k,l]$, $k=0,\ldots,M-1$ and $l=-N/2,\ldots,N/2$, consist of realizations of the i.i.d. random variables, each having the uniform distribution on the interval $[0,2\pi)$. If M and N are sufficiently large, then the distribution of the TVFR $\mathbf{h}[m,n]$ approaches the complex Gaussian multivariate distribution due to the central limit theorem (CLT) [28].

In practice, the delay-Doppler PSD $\mathbf{P}_h(\tau',f_d)$ is unknown. Therefore, an estimate $\hat{\mathbf{P}}_h(\tau',f_d)$, obtained by substituting the estimated matrix coefficients $\left\{\hat{\mathbf{A}}[i_1,i_2]\right\}_{\substack{[i_1,i_2]\in\mathcal{S}_{QP},\\ [i_1,i_2]\neq[0,0]}}$ and the noise delay-Doppler PSD $\hat{\mathbf{P}}_u$ (see Section 4.3) into (4.6), is used in lieu of the delay-Doppler PSD $\mathbf{P}_h(\tau',f_d)$ in (4.27).

4.6 Simulation Results

In this section, we present two examples that illustrate the performance of the multichannel 2D AR models employed as channel simulators. In each of the examples, the role of the measured 2×2 MIMO channel is played by a channel simulator with known parameter values, in the following referred to as the *prototype* model. The task is to estimate the parameters of the multichannel 2D AR(p_1,p_2) model (4.3), the *target* model, from the TVFR $\tilde{\mathbf{h}}[m,n]$ synthesized by using the *prototype* model.

In the first example, the *prototype* model is the multichannel 2D AR(2,2) model. The parameters of the *target* multichannel 2D AR(2,2) model, i.e., the matrix coefficients $\mathbf{A}[i_1,i_2]$ and the noise delay-Doppler PSD matrix $\mathbf{P}_u$, have been estimated from a *training* TVFR sequence $\tilde{\mathbf{h}}[m,n]$, $1\leq m\leq 193$, $1\leq n\leq 100$, by employing the PEM and the YW methods (see Section 4.3). The BIBO stability test (4.23) shows that both *target* multichannel 2D AR(2,2) models resulting from applying the PEM and the YW parameter estimation methods are stable.

To evaluate the performance of the *target* multichannel 2D AR(2,2) models, the *test* TVFRs $\mathbf{h}[m,n]$ have been generated using the resulting *target* models. Another *test* TVFR $\tilde{\mathbf{h}}[m,n]$, of the same length as $\mathbf{h}[m,n]$, has been obtained using the *prototype* model. The TCCFs $\hat{r}_{t_{i_1,i_2}}[\iota]$, $i_1, i_2 = 1, \ldots, N_T N_R$, and the FCCFs $\hat{r}_{f'_{i_1,i_2}}[\kappa]$, of the *target* multichannel 2D AR(2,2) models are estimated from the *test* TVFRs $\mathbf{h}[m,n]$. Similarly, the TCCFs $\hat{\tilde{r}}_{t_{i_1,i_2}}[\iota]$ and the FCCFs $\hat{\tilde{r}}_{f'_{i_1,i_2}}[\kappa]$ of the *prototype* model are estimated from the *test* TVFR $\tilde{\mathbf{h}}[m,n]$. Some estimated TCCFs and FCCFs of the *target* models and of the *prototype* model are shown in Fig. 4.3.

As can be seen in Fig. 4.3, the selected TCCFs and the FCCFs of the *target* multichannel 2D AR(2,2) models approximate well their respective counterparts of the *prototype* model. Similar results are observed for other estimated temporal and frequency cross-correlation functions. Additionally, the results presented for the *target* model obtained by applying the PEM parameter estimation method are very close to those corresponding to the *target* model obtained by using the YW algorithm.

The *prototype* model in the second example, is a channel simulator based on the double-directional channel model [5]. In the double-directional model the wireless propagation channel is represented by a set of L complex exponents (multipath components). Each of these complex exponents is characterized by the complex amplitude, Doppler frequency, propagation delay, direction-of-arrival, direction-of-departure, and, possibly, polarization matrix. In our double-directional model, the transmitter is stationary and the receiver is moving. The transmitter and the receiver are equipped with linear antenna arrays. Each of the antenna arrays consists of two ($N_T = N_R = 2$) omnidirectional single-polarization antenna elements separated by a half wavelength distance. The radio waves propagate in the azimuthal plane. Several other parameters are specified below:

- Number of multipath components: $L = 530$;
- Time interval between snapshots: $\triangle t = 10$ ms;
- Signal carrier frequency: $f'_c = 5.2$ GHz;
- Interval between frequencies: $\triangle f' = 3.125 \cdot 10^5$ Hz;
- Frequency bandwidth: $B = 60$ MHz;
- Measurement noise SNR: 20 dB.

The multipath components of the *prototype* model in the delay-Doppler plane are shown in Fig. 4.4. Note that this example represents an extreme case in a sense that the delay-Doppler PSD of the TVFR synthesized using the *prototype*

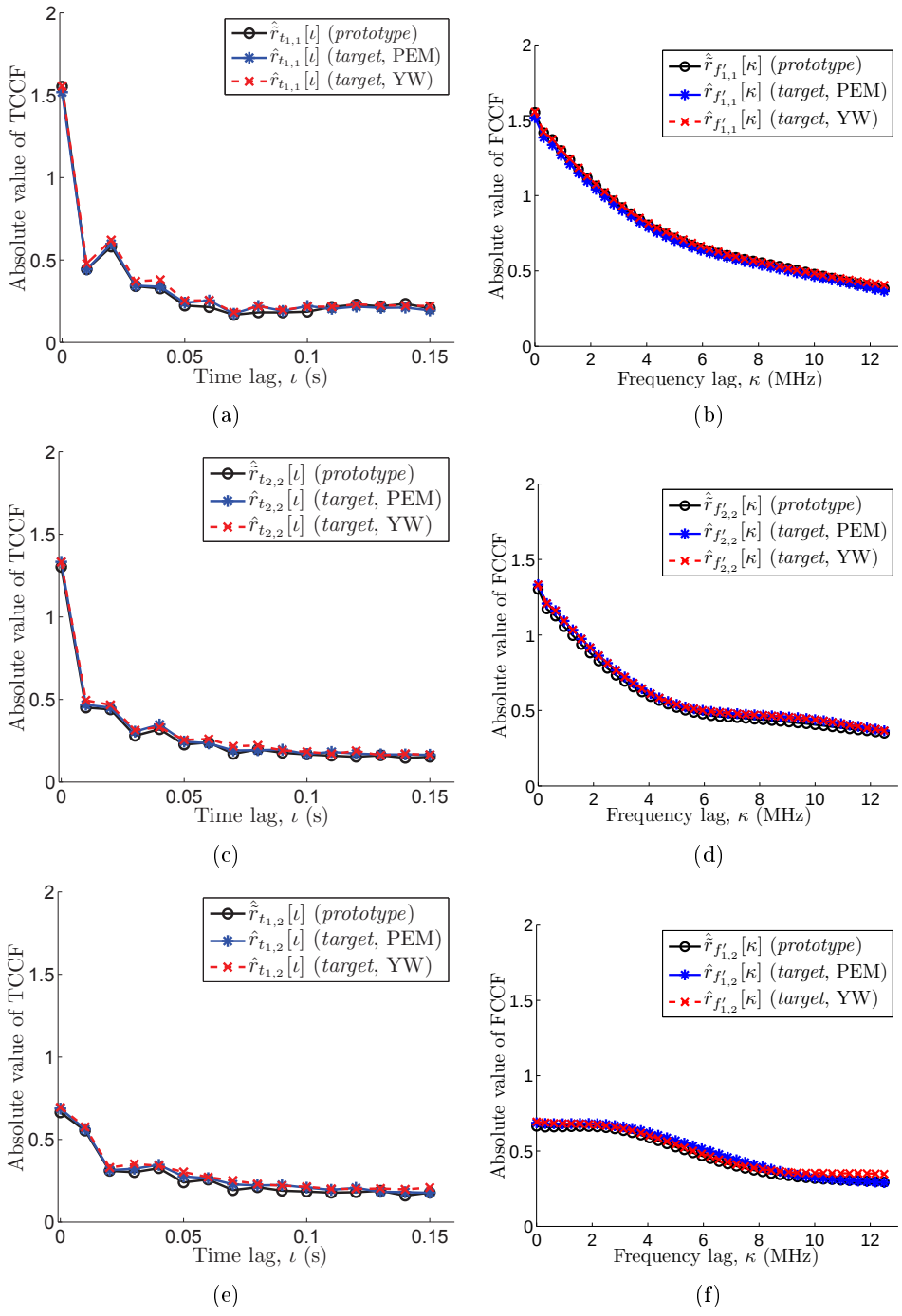

Figure 4.3: The TCCFs and FCCFs of the *prototype* multichannel 2D AR(2,2) model and of the *target* multichannel 2D AR(2,2) model (example 1).

model is discrete, while the *target* multichannel 2D AR(p_1,p_2) model implies a continuous delay-Doppler PSD.

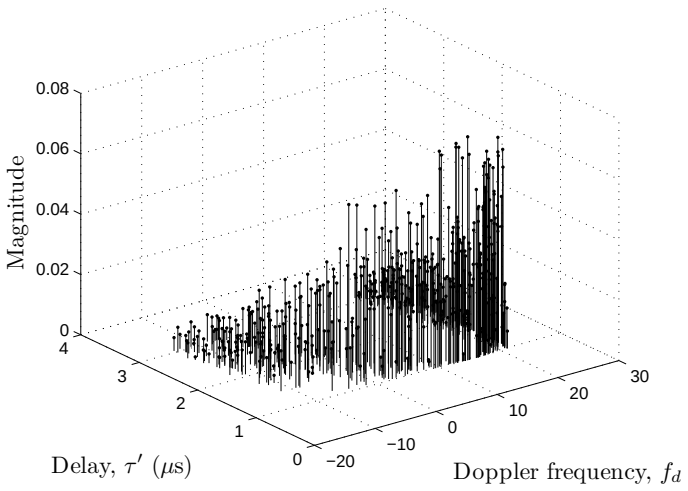

Figure 4.4: The multipath components (example 2).

Again, as in the first example, the *training* TVFR $\tilde{\mathbf{h}}[m,n]$, $1 \leq m \leq 193, 1 \leq n \leq 100$, has been generated using the *prototype* model and supplied to the PEM to estimate the parameters $\mathbf{A}[i_1,i_2]$ and $\mathbf{P}_u$ of the *target* multichannel 2D AR(p_1,p_2) model. In this case, the parameters of the multichannel 2D AR(1,1), AR(3,3), AR(5,5), and AR(10,10) models have been estimated. All of the *target* models have been stabilized using the procedure described in Subsection 4.4.2.

The TCCFs $\hat{r}_{t_{i_1,i_2}}[\iota]$, $i_1,i_2 = 1,\ldots,N_TN_R$, of the resulting *target* models and the TCCFs $\hat{\tilde{r}}_{t_{i_1,i_2}}[\iota]$ of the *prototype* model have been estimated from the generated *test* sequences $\mathbf{h}[m,n]$ and $\tilde{\mathbf{h}}[m,n]$, respectively. Similarly, the FCCFs $\hat{r}_{f'_{i_1,i_2}}[\kappa]$ of the resulting *target* models and the FCCFs $\hat{\tilde{r}}_{f'_{i_1,i_2}}[\kappa]$ of the *original* model have been estimated from the corresponding *test* sequences. In Fig. 4.5, we demonstrate the estimated TCCFs and FCCFs for several subchannels of the resulting (stabilized) *target* models and of the *prototype* model. The TCCFs and FCCFs of the *target* models rather poorly approximate the corresponding correlation functions of the *prototype* model as compared to the results presented in Fig. 4.3.

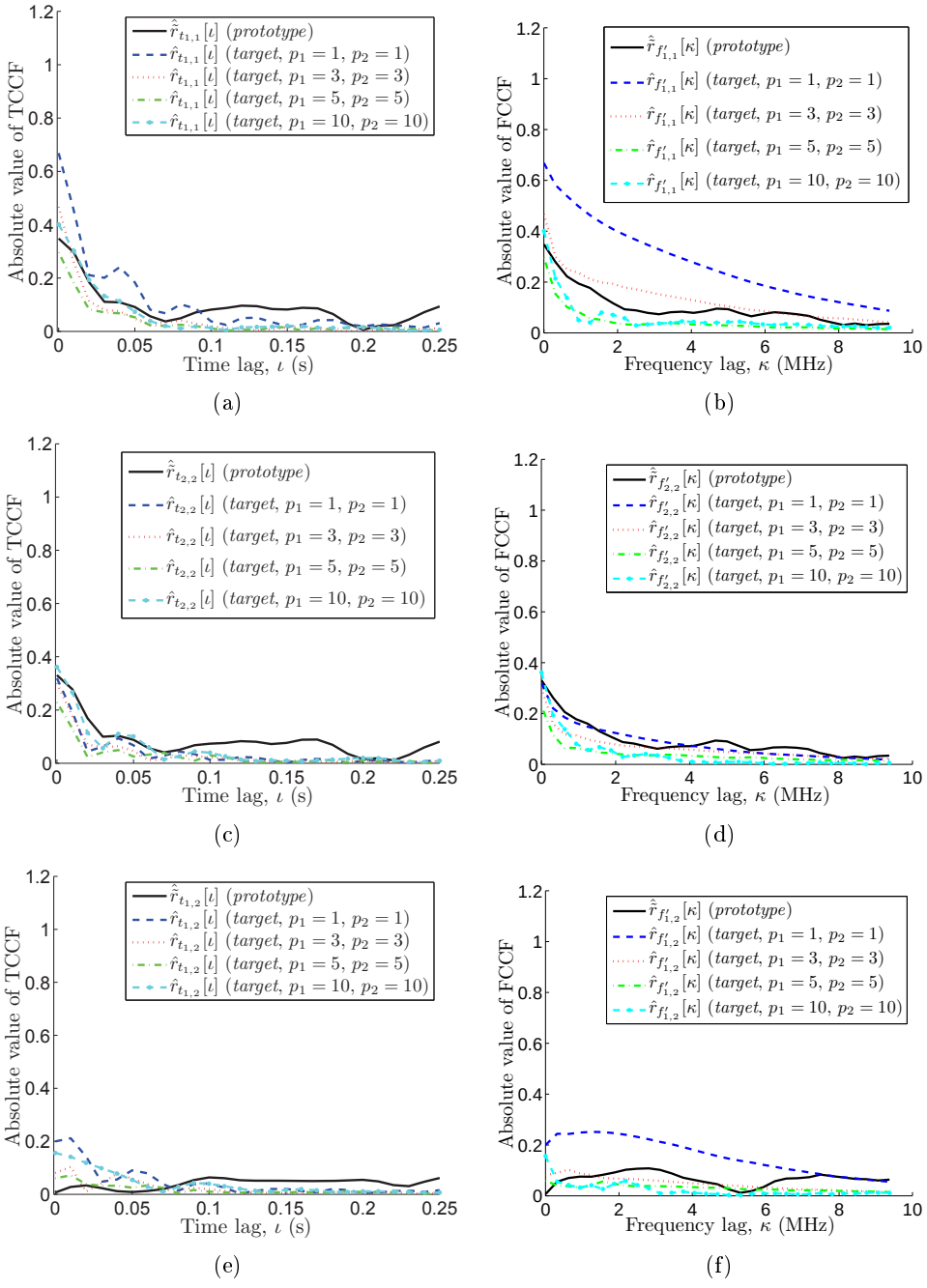

Figure 4.5: The TCCFs and FCCFs of the *prototype* model and of the *target* models (example 2).

The effect of applying the stabilization procedure to the *target* multichannel 2D AR(10,10) model can be observed in Fig. 4.6 where we depict the delay-Doppler PSD (for the first subchannel) before and after stabilization. The delay-Doppler PSDs of the *target* models have been calculated using (4.6). Note the presence of multiple spurious peaks in the delay-Doppler PSD, which are particularly noticeable in Fig. 4.6 (b).

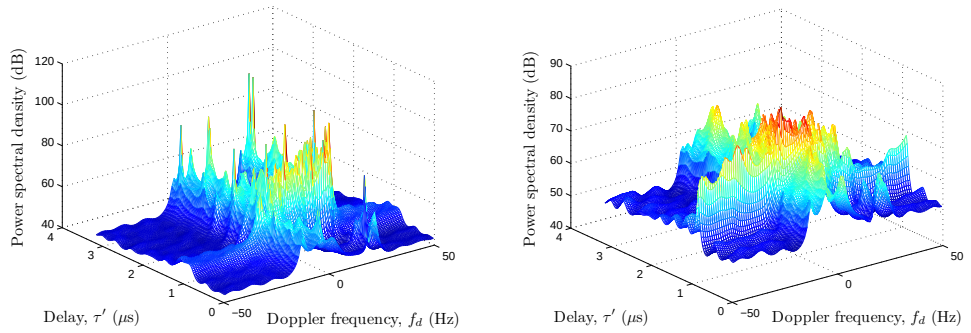

(a) (b)

Figure 4.6: The delay-Doppler PSD of the *target* multichannel 2D AR(10,10) model (a) before stabilization and (b) after stabilization (example 2).

4.7 Application to Measurement Data

In this section, we develop several multichannel 2D AR(p_1,p_2) models based on real-world measurement data. The description of the measurement sites and the measurement equipment can be found in Appendix A.

The parameters of all multichannel 2D AR(p_1,p_2) models presented below have been estimated from the measurement data by using the PEM algorithm described in Subsection 4.3.2. Empirically, it has been observed that the PEM algorithm is preferable for estimating the parameters of the multichannel 2D AR(p_1,p_2) models as compared to the YW method (see Subsection 4.3.1). As this observation is in a agreement with the results available in the literature for the case of 1D AR models (see, e.g., [64]), we do not provide the details related to the performance of the multichannel 2D AR(p_1,p_2) models developed by using the YW parameter estimation method.

4.7.1 Model Order Selection

The development of the multichannel 2D AR(p_1,p_2) model starts with selecting an appropriate order (p_1,p_2) of the model. A number of methods for model order selection has been proposed in the literature (see, e.g., [34, 36, 77, 78]). In this work, we use the well-known cross-validation method [36, 77]. This choice is motivated by the fact that the cross-validation method does not rely on any *a priory* information or analytical analysis of the measurement data.

For comparison reasons, we also assess the order of the multichannel 2D AR(p_1,p_2) model by using the following rule. A realization of the channel TVFR $\mathbf{h}[m,n]$ is generated by using a candidate multichannel 2D AR(p_1,p_2) model. The parameters $\hat{\mathbf{P}}_u$ and $\hat{\mathbf{A}}[i_1,i_2]$, $0 \leq i_1 \leq p_1, 0 \leq i_2 \leq p_2$, of the candidate model are estimated from the measured TVFR $\tilde{\mathbf{h}}[m,n]$ of a real-world channel by employing the PEM algorithm. The correlation matrix $\underline{\hat{\mathbf{R}}}$, estimated from the synthesized TVFR $\mathbf{h}[m,n]$ as described in Subsection 3.4.1, is compared to the correlation matrix $\underline{\hat{\tilde{\mathbf{R}}}}$ estimated similarly from the measured TVFR $\tilde{\mathbf{h}}[m,n]$. The comparison is done in terms of the normalized approximation error norm defined as $\|\underline{\hat{\tilde{\mathbf{R}}}} - \underline{\hat{\mathbf{R}}}\|_F / \|\underline{\hat{\tilde{\mathbf{R}}}}\|_F$. Finally, a candidate model, which provides the smallest normalized error norm, is chosen. In the following, this rule will be referred to as the correlation matrix fitting (CMF) rule. Note that the CMF rule represents an intuitive way of choosing the order of the multichannel 2D AR(p_1,p_2) model, according to the problem formulation given in Section 3.3.

It should be mentioned that in all examples presented below, we have considered the candidate multichannel 2D AR(p_1,p_2) models in the range $1 \leq p_1 \leq 15$, $1 \leq p_2 \leq 6$.

4.7.2 Micro Cell Site – Regular Street Geometry

For the measured TVFR of the channel considered in this subsection, the cross-validation method and the CMF rule yield as the best candidate, respectively, the multichannel 2D AR(6,1) and AR(9,5) models. The stability test (4.23) shows that the multichannel 2D AR(9,5) model is unstable. Hence, the four-step procedure described in Subsection 4.4.2 has been applied to stabilize the model.

In Fig. 4.7, several estimated TCCFs $\hat{\tilde{r}}_{t_{i_1,i_2}}[\iota]$ and FCCFs $\hat{\tilde{r}}_{f'_{i_1,i_2}}[\kappa]$, extracted from the correlation matrix $\underline{\hat{\tilde{\mathbf{R}}}}$ of the measured channel (see Subsection 3.4.1), are presented. In the same figure, we also show the corresponding estimates of the TCCFs $\hat{r}_{t_{i_1,i_2}}[\iota]$ and the FCCFs $\hat{r}_{f'_{i_1,i_2}}[\kappa]$, $i_1, i_2 = 1, \ldots, N_T N_R$, for the multichannel 2D AR(6,1) and AR(9,5) models. Note that the approximate 95% confidence intervals depicted in Fig. 4.7 are related to the TCCFs $\hat{\tilde{r}}_{t_{i_1,i_2}}[\iota]$ and FCCFs $\hat{\tilde{r}}_{f'_{i_1,i_2}}[\kappa]$ estimated from the real-world measurement data. The results presented in Fig. 4.7 can be compared to the results in Fig. 3.3.

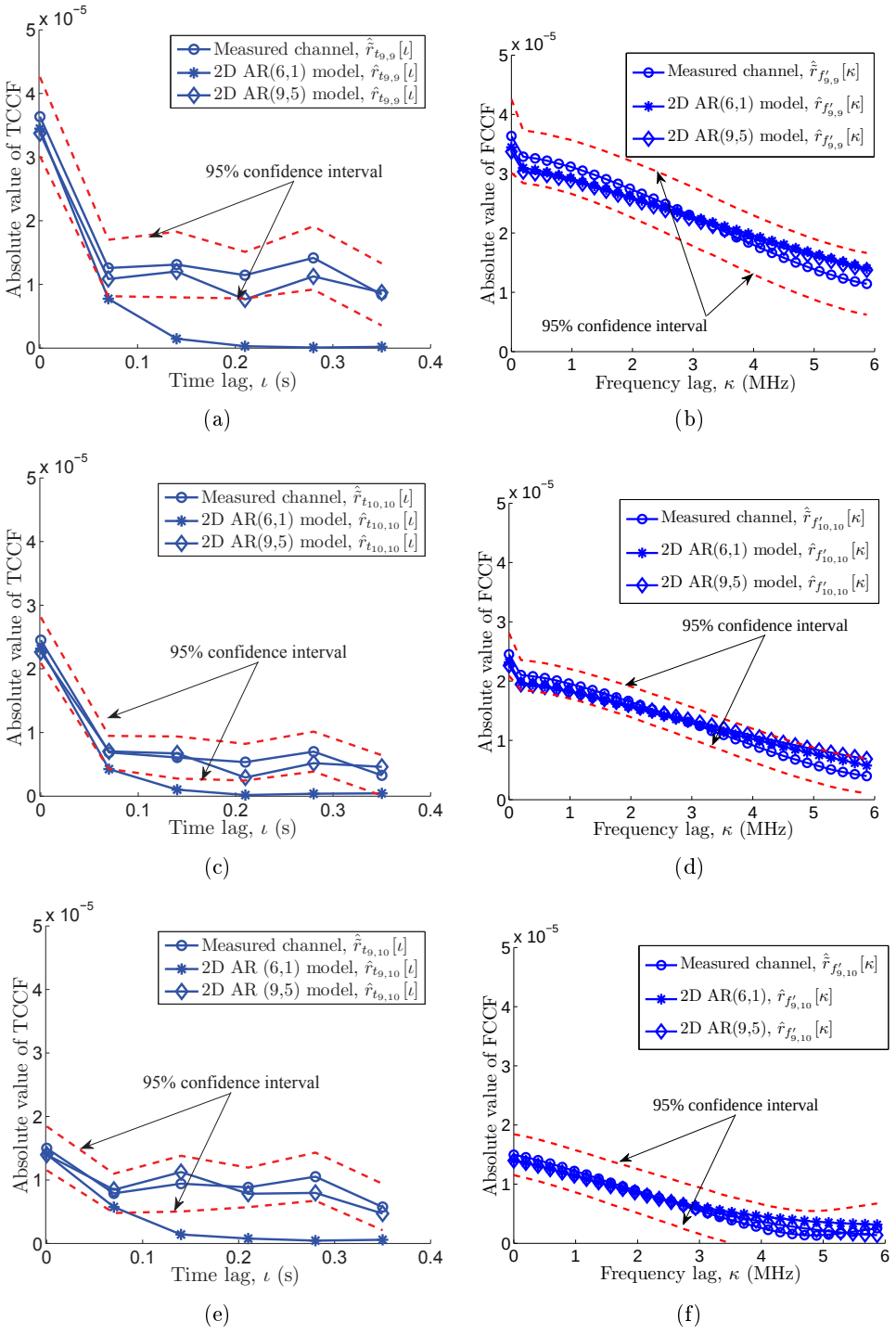

Figure 4.7: Examples of the estimated TCCFs and FCCFs of the physical channel and the corresponding TCCFs and FCCFs of the multichannel 2D AR(p_1,p_2) models (micro cell site – regular street geometry).

It follows from Fig. 4.7 that the multichannel 2D AR(9,5) model better approximates the temporal correlation characteristics of the real-world prototype channel than the 2D AR(6,1) model.

The estimated delay-Doppler PSDs $\hat{P}_h(\tau', f_d)$ of the 2D AR(6,1) and the 2D AR(9,5) models are depicted in Fig. 4.8.

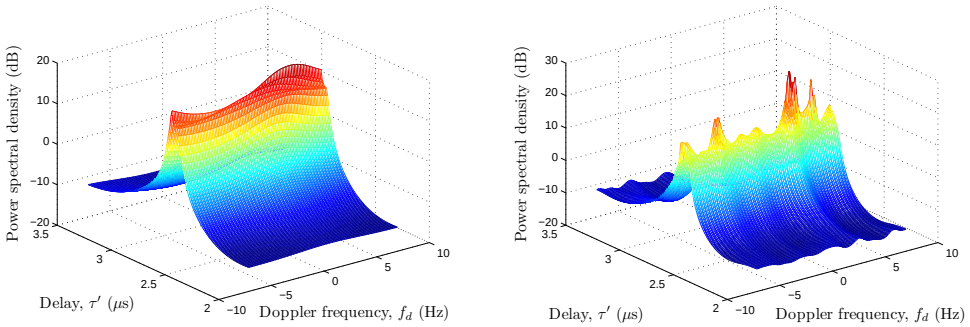

(a) (b)

Figure 4.8: The delay-Doppler PSD $\hat{P}_h(\tau', f_d)$ of the (a) 2D AR(6,1) model; (b) 2D AR(9,5) (micro cell site – regular street geometry).

The estimated Doppler PSDs $\hat{P}_{h_{f_d}}(f_d)$ of the multichannel 2D AR(6,1) and AR(9,5) models are shown in Fig. 4.9 together with the Doppler PSD $\hat{\hat{P}}_{h_{f_d}}(f_d)$ estimated from the measured TVFR $\tilde{h}_{1,1}[m,n]$. The estimate of the Doppler PSD $\hat{\hat{P}}_{h_{f_d}}(f_d)$ has been obtained by using the averaged periodogram method (see, e.g., [64]). To reduce the bias in the estimated Doppler PSD, we have tapered the measured TVFR $\tilde{h}_{1,1}[m,n]$ in the time domain with the Hanning window [79]. Similarly, the estimated delay PSDs $\hat{P}_{h_{\tau'}}(\tau')$ of the multichannel 2D AR(6,1) and AR(9,5) models as well as the delay PSD $\hat{\hat{P}}_{h_{\tau'}}(\tau')$ estimated from the measured TVFR $\tilde{h}_{1,1}[m,n]$ are presented in Fig. 4.10. Since the variances of the estimated Doppler PSD $\hat{\hat{P}}_{h_{f_d}}(f_d)$ and the delay PSD $\hat{\hat{P}}_{h_{\tau'}}(\tau')$ are rather small, the corresponding confidence intervals are not shown in Figs. 4.9 and 4.10.

From Fig. 4.9, it appears that the order of the AR(6,1) model w.r.t. time is underestimated, which results in the oversmoothed Doppler PSD. As the main reason for an underestimated order of the multichannel 2D AR model selected by the cross-validation method (see Subsection 4.7.1), we consider a small number N of the available channel TVFR snapshots ($N < 20$ for the examples presented in this and the following two subsections).

It is of interest to analyze the results presented in Fig. 4.9 in terms of the first two spectral moments, i.e., the estimated average Doppler shift and the estimated Doppler spread. The estimated average Doppler shift $\hat{\hat{\mu}}_{f_d}$ and the estimated

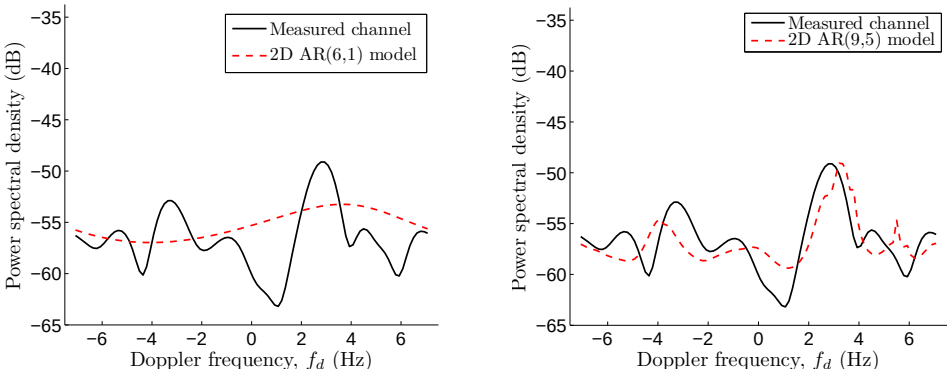

Figure 4.9: The Doppler PSDs for the multichannel 2D AR(p_1,p_2) models and the measured channel (micro cell site – regular street geometry).

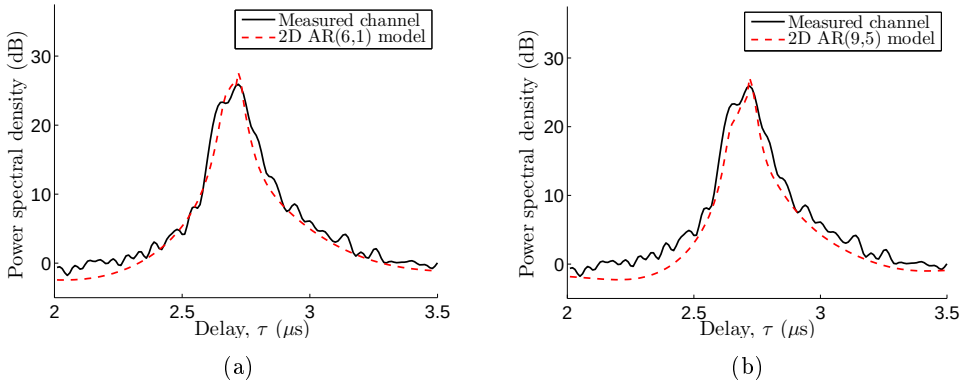

Figure 4.10: The delay PSDs for the multichannel 2D AR(p_1,p_2) models and the measured channel (micro cell site – regular street geometry).

Doppler spread $\hat{\tilde{\sigma}}_{f_d}$ of a measured channel are defined, respectively, as

$$\hat{\tilde{\mu}}_{f_d} = \frac{\int_{-f_{d\max}}^{f_{d\max}} f_d \hat{\tilde{P}}_{f_d}(f_d) df_d}{\int_{-f_{d\max}}^{f_{d\max}} \hat{\tilde{P}}_{f_d}(f_d) df_d} \tag{4.29}$$

and

$$\hat{\tilde{\sigma}}_{f_d} = \sqrt{\frac{\int_{-f_{d\max}}^{f_{d\max}} f_d^2 \hat{\tilde{P}}_{f_d}(f_d) df_d}{\int_{-f_{d\max}}^{f_{d\max}} \hat{\tilde{P}}_{f_d}(f_d) df_d} - (\hat{\tilde{\mu}}_{f_d})^2}. \tag{4.30}$$

where $f_{d\max}$ is given by $f_{d\max} = 1/(2\triangle t)$ and $\triangle t$ denotes the interval between the channel snapshots. Of cause in practice, the integrals in (4.29),(4.30) have

to be approximated with the finite sums. The average Doppler shift $\hat{\mu}_{f_d}$ and the Doppler spread $\hat{\sigma}_{f_d}$ of the estimated Doppler PSD $\hat{P}_{h_{f_d}}(f_d)$ of the multichannel 2D AR(p_1,p_2) model are defined in a similar way.

By analogy, the results presented in Fig. 4.10 can be analyzed in terms of the estimated average delay shift and the estimated delay spread. The estimated average delay shift $\hat{\tilde{\mu}}_{\tau'}$ and the estimated delay spread $\hat{\tilde{\sigma}}_{\tau'}$ of a measured real-world channel are given by

$$\hat{\tilde{\mu}}_{\tau'} = \frac{\int_{\tau'_{\rm lb}}^{\tau'_{\rm ub}} \tau' \hat{\tilde{P}}_{\tau'}(\tau') d\tau'}{\int_{\tau'_{\rm lb}}^{\tau'_{\rm ub}} \hat{\tilde{P}}_{\tau'}(\tau') d\tau'} \tag{4.31}$$

and

$$\hat{\tilde{\sigma}}_{\tau'} = \sqrt{\frac{\int_{\tau'_{\rm lb}}^{\tau'_{\rm ub}} \tau'^2 \hat{\tilde{P}}_{\tau'}(\tau') d\tau'}{\int_{-\tau'_{\rm lb}}^{\tau'_{\rm ub}} \hat{\tilde{P}}_{\tau'}(\tau') d\tau'} - (\hat{\tilde{\mu}}_{\tau'})^2} \tag{4.32}$$

respectively. The average delay shift $\hat{\mu}_{\tau'}$ and the delay spread $\hat{\sigma}_{\tau'}$ of the estimated delay PSD $\hat{\tilde{P}}_{h_{\tau'}}(\tau')$ of the multichannel 2D AR(p_1,p_2) model are defined similarly. The limits of the integrals $\tau'_{\rm lb}$ and $\tau'_{\rm ub}$ in (4.31),(4.32) correspond to the -20 dB noise threshold as referred to the maximum of the estimated delay PSD $\hat{\tilde{P}}_{h_{\tau'}}(\tau')$ [2]. The integrals in (4.31),(4.32) are approximated with the finite sums.

The estimated spectral moments of the multichannel 2D AR(6,1) and AR(9,5) models as well as the spectral moments obtained from the estimated single-dimensional PSDs $\hat{\tilde{P}}_{h_{f_d}}(f_d)$ and $\hat{\tilde{P}}_{h_{\tau'}}(\tau')$ of the measured channel are collected in Table 4.1. Additionally, we have also included in Table 4.1 the results obtained for the channel simulator based on the model (3.7), which has been developed in Subsection 3.6.1 by using the design method of Subsection 3.4.2. The confidence intervals for the spectral moments estimated from the measurement data are specified in brackets.

Table 4.1: Spectral moments (micro cell site – regular street geometry).

	Measured channel	2D AR(6,1)	2D AR(9,5)	Channel simulator (3.7)
Doppler shift, μ_{f_d} (Hz)	0.51 [0.47, 0.54]	0.95	0.85	0.66
Squared Doppler spread, $\sigma^2_{f_d}$ (Hz^2)	14.72 [14.58, 14.85]	15.52	14.76	14.55
Delay shift, $\mu_{\tau'}$ (μs)	2.709 [2.707, 2.710]	2.708	2.714	2.705
Squared delay spread, $\sigma^2_{\tau'}$ (μs^2)	0.0037 [0.0035, 0.0039]	0.0027	0.0029	0.0022

The (squared) Doppler and delay spreads represent the main interest for us. As it follows from Table 4.1, the squared delay and Doppler spreads of the multi-

channel 2D AR(9,5) model are somewhat closer, as compared to other considered channel simulators, to the squared delay and Doppler spreads of the measured channel.

Note that the specified confidence intervals for the estimated spectral moments of the measured channel, although useful for indicating the variability of the corresponding parameters, are not sufficient for determining if the differences between the spectral moments of the channel simulation models and the spectral moments of the measured channel are significant. For example, the estimated squared delay spread is equal to 0.0042 μs^2 or 0.0035 μs^2 when the Blackman or Hamming window [79], respectively, is used for estimating the delay spectral moments from the measurement data. Both these values are outside the confidence interval $[0.0035, 0.0039]$ μs given in Table 4.1.

In Fig. 4.11, the CDFs of the instantaneous channel capacity (mutual information) $C[n]$ (3.48) of the measured channel and of the channels generated by using the multichannel 2D AR(6,1) and 2D AR(9,5) models[3] are presented. Clearly, the capacity CDFs of the multichannel 2D AR models are slightly biased towards the higher capacity values. The estimated mean μ_C values and standard deviations σ_C of the capacity for the multichannel 2D AR(6,1) model, 2D AR(6,1) model, and the measured channel are given in Table 4.2.

Table 4.2: Estimated mean and standard deviation of the capacity (micro cell site – regular street geometry).

	Measured channel	2D AR(6,1)	2D AR(9,5)
Mean, μ_C (bps/Hz)	7.25	7.58	7.7
Standard deviation, σ_C (bps/Hz)	0.81	0.8	0.82

The capacity CDFs in Fig. 4.11 can be compared to the capacity CDF for the channel simulator (3.7) demonstrated in Fig. 3.5

[3] In the following, we refer to the instantaneous capacity of channels synthesized by a multichannel 2D AR(p_1,p_2) model simply as the capacity of the multichannel 2D AR(p_1,p_2) model.

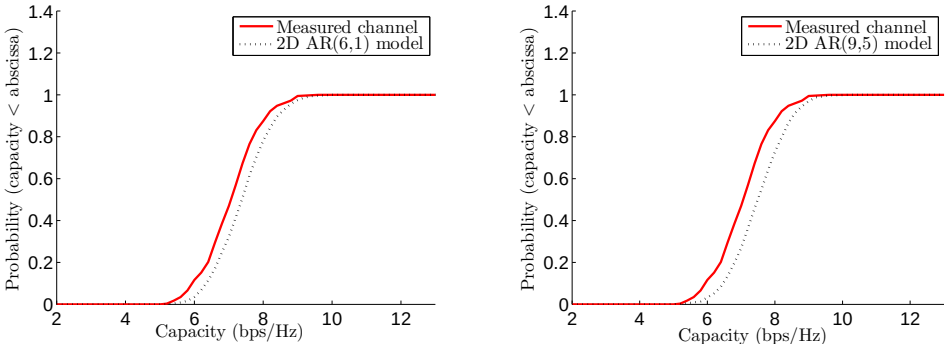

Figure 4.11: Capacity CDFs of the multichannel 2D AR(p_1,p_2) models and of the measured channel for an SNR $\rho = 20$ dB (micro cell site – regular street geometry).

4.7.3 Micro Cell Site – Open Market Place

The results of applying the cross-validation method and the CMF rule (see Subsection 4.7.1) suggest that the multichannel 2D AR(6,1) model (the cross-validation method) and the AR(6,2) model (the CMF rule) are the best candidates. The stability test (4.23) demonstrates that both the multichannel 2D AR(6,1) and AR(6,2) models are BIBO stable.

Examples of the estimated TCCFs $\hat{r}_{t_{i_1,i_2}}[\iota]$ and FCCFs $\hat{r}_{f'_{i_1,i_2}}[\kappa]$ of the multichannel 2D AR(6,1) and AR(6,2) models are depicted in Fig 4.12 together with their respective counterparts $\hat{\hat{r}}_{t_{i_1,i_2}}[\iota]$ and $\hat{\hat{r}}_{f'_{i_1,i_2}}[\kappa]$ of the measured channel. As can be seen from the graphs presented in Fig 4.12, some improvement in the approximation of the TCCFs $\hat{\hat{r}}_{t_{i_1,i_2}}[\iota]$ can be observed for the multichannel 2D AR(6,2) model compared to the AR(6,1) model, although, at the expense of worsening the agreement between the estimated FCCFs. Figure 4.12 can be compared with the corresponding results presented in Figure 3.7.

The estimated delay-Doppler PSDs $\hat{P}_h(\tau', f_d)$ of the 2D AR(6,1) and 2D AR(6,2) models are depicted in Fig 4.13. The spectral characteristics of the multichannel 2D AR(6,1) and 2D AR(6,2) models are further compared in Figs. 4.14 and 4.15, where the estimated Doppler and delay PSDs are shown, respectively.

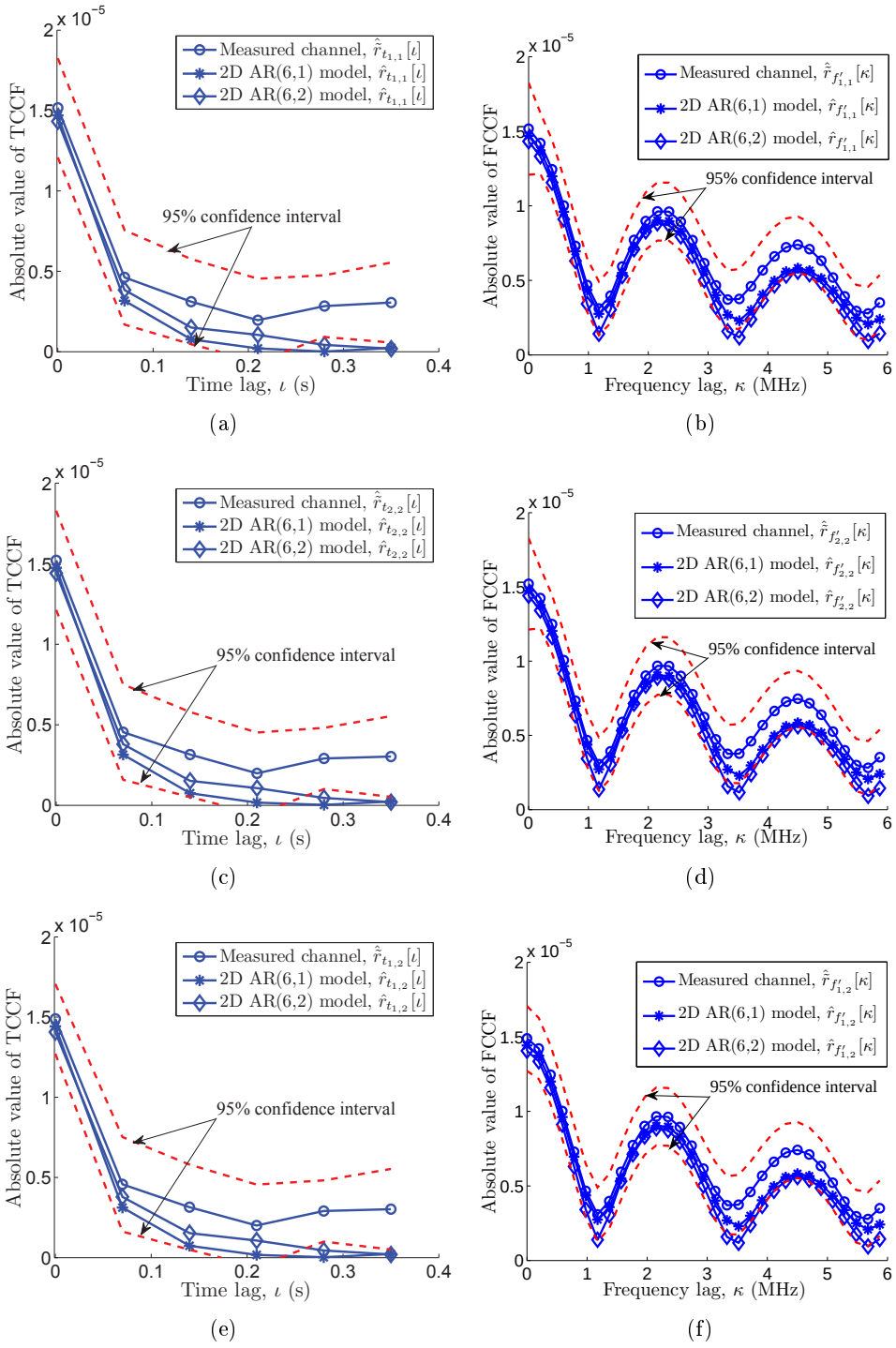

Figure 4.12: Examples of the estimated TCCFs and FCCFs of the physical channel and the corresponding TCCFs and FCCFs of the multichannel 2D AR(p_1,p_2) models (micro cell site – open market place).

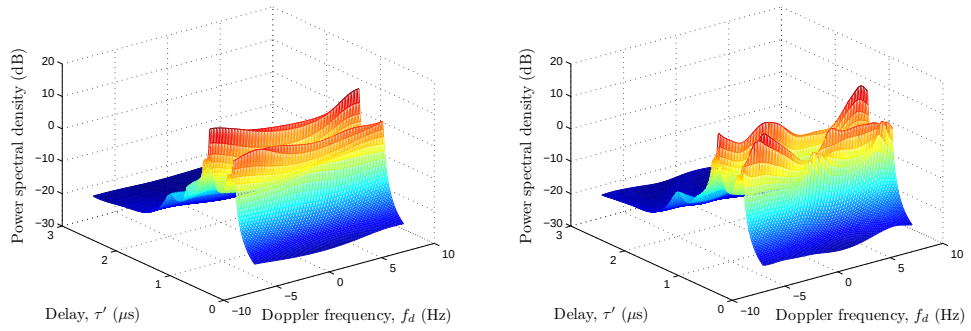

(a) (b)

Figure 4.13: The delay-Doppler PSD $\hat{P}_h(\tau', f_d)$ of the (a) 2D AR(6,1) model and (b) 2D AR(6,2) (micro cell site – open market place).

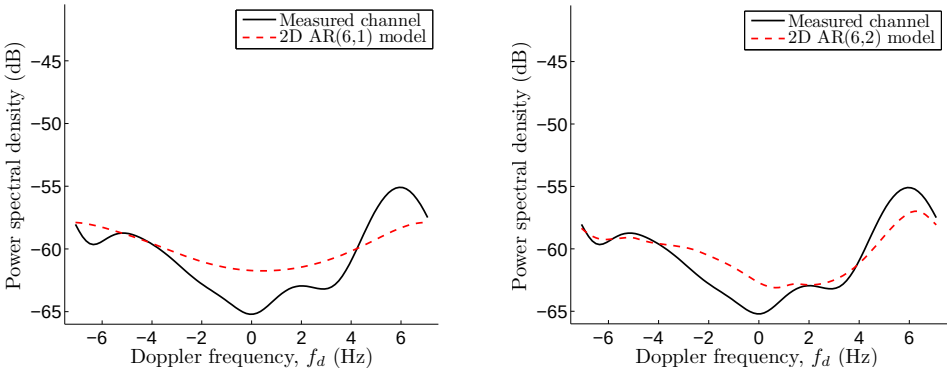

(a) (b)

Figure 4.14: The Doppler PSDs for the multichannel 2D AR(p_1,p_2) models and the measured channel (micro cell site – open market place).

As in the previous subsection, we have collected the estimated first and second order spectral moments for the measured channel and the 2D AR models in Table 4.3. As it can be seen from Table 4.3, the squared Doppler spread of the channel simulator based on the model (3.7), which has been developed in Subsection 3.6.2, is a bit closer to the squared Doppler spread of the measured channel as compared to the results provided by the multichannel 2D AR models. However, the squared delay spread of the multichannel 2D AR models is closer to the squared delay spread of the estimated delay PSD $\hat{\hat{P}}_{h_{\tau'}}(\tau')$. Consistent with Figs. 4.14 and 4.15, the differences between the estimated spectral moments of the multichannel 2D AR(6,1) and 2D AR(6,2) models are rather small.

The CDFs of the instantaneous channel capacity $C[n]$ (3.48) of the measured

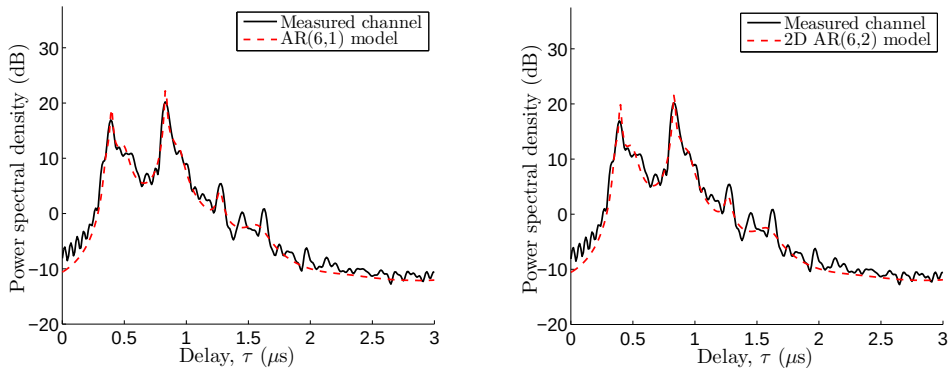

Figure 4.15: The delay PSDs for the multichannel 2D AR(p_1,p_2) models and the measured channel (micro cell site – open market place).

Table 4.3: Spectral moments (micro cell site – open market place).

	Measured channel	2D AR(6,1)	2D AR(6,2)	Channel simulator (3.7)
Doppler shift, μ_{f_d} (Hz)	1.106 $[1.05, 1.16]$	-0.11	0.19	0.02
Squared Doppler spread, $\sigma^2_{f_d}$ (Hz^2)	24.5 $[24.36, 24.64]$	21.7	22.47	23.87
Delay shift, $\mu_{\tau'}$ (μs)	0.71 $[0.706, 0.722]$	0.707	0.68	0.704
Squared delay spread, $\sigma^2_{\tau'}$ (μs^2)	0.053 $[0.051, 0.055]$	0.051	0.054	0.048

channel and of the multichannel 2D AR(6,1) and 2D AR(6,2) models are demonstrated in Fig. 4.16. Clearly, the CDF curves are in good agreement. The mean values μ_C and the standard deviations σ_C of the capacity for the multichannel 2D AR models and the measured channel are presented in Table 4.4.

Table 4.4: Estimated mean and standard deviation of the capacity (micro cell site – open market place).

	Measured channel	2D AR(6,1)	2D AR(9,5)
Mean, μ_C (bps/Hz)	8.63	8.73	8.75
Standard deviation, σ_C (bps/Hz)	1.32	1	1.03

The capacity CDFs of the multichannel 2D AR(6,1) and 2D AR(6,2) models in Fig. 4.16 can be compared with the capacity CDF of the channel simulator based on the model (3.7) presented in Fig. 3.9.

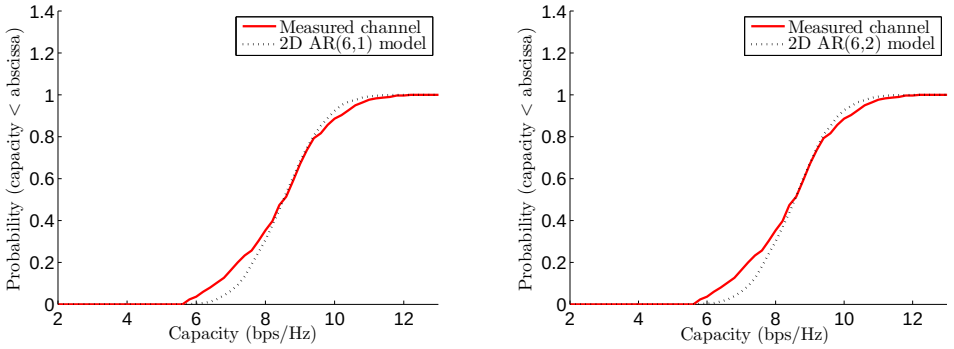

Figure 4.16: Capacity CDFs for the multichannel 2D AR(p_1,p_2) models and the measured channel for an SNR $\rho = 20$ dB (micro cell site – open market place).

4.7.4 Micro/Pico Cell Site – Passageway

As before, we start with selecting an appropriate order of the multichannel 2D AR(p_1,p_2) model. Again, for this purpose we employ two approaches: the cross-validation method and the CMF rule described in Subsection 4.7.1. The two methods yield two different best candidate models, which are the multichannel 2D AR(5,1) model (according to the cross-validation method) and the multichannel 2D AR(10,4) model (the CNF rule). Both these models are BIBO stable according to the results obtained by using the stability test (4.23).

In Fig. 4.17, the examples of the TCCFs $\hat{\tilde{r}}_{t_{i_1,i_2}}[\iota]$ and FCCFs $\hat{\tilde{r}}_{f'_{i_1,i_2}}[\kappa]$, estimated from the measured TVFR of the real-world channel, are depicted together with the estimated TCCFs $\hat{r}_{t_{i_1,i_2}}[\iota]$ and FCCFs $\hat{r}_{f'_{i_1,i_2}}[\kappa]$ of the multichannel 2D AR(5,1) and AR(10,4) models. The estimated TCCFs $\hat{r}_{t_{i_1,i_2}}[\iota]$ of the multichannel 2D AR(5,1) model decay faster than the corresponding estimated TCCFs $\hat{\tilde{r}}_{t_{i_1,i_2}}[\iota]$ of the measured channel and the estimated TCCFs $\hat{r}_{t_{i_1,i_2}}[\iota]$ of the multichannel 2D AR(10,4) model.

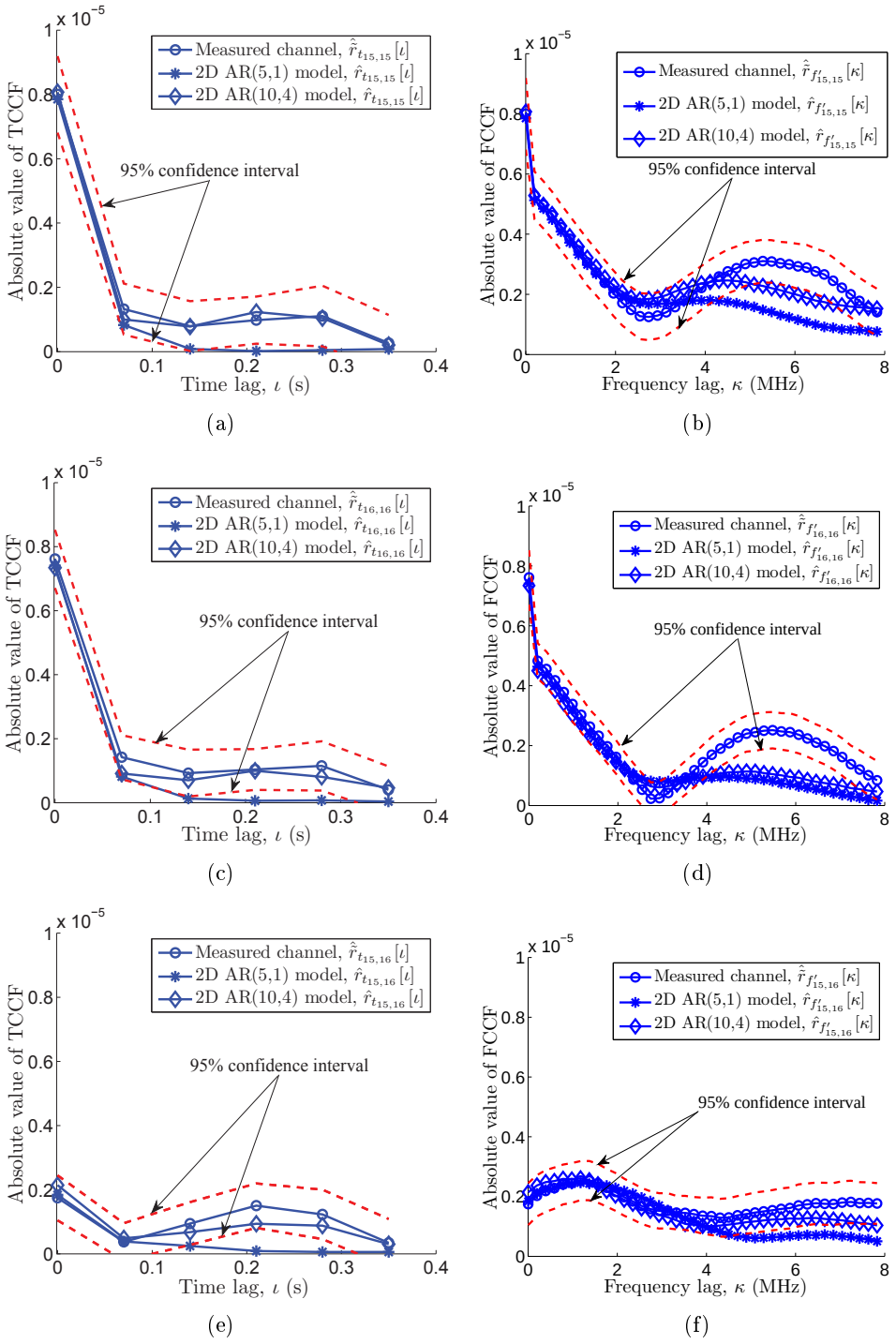

Figure 4.17: Examples of the estimated TCCFs and FCCFs of the physical channel and the corresponding TCCFs and FCCFs of the multichannel 2D AR(p_1,p_2) models (micro/pico cell site – passageway).

As it can also be seen from Fig. 4.17, increasing the order of the model from (5,1) to (10,4) does not remove the discrepancy between the estimated FCCFs $\hat{\hat{r}}_{f'_{i_1,i_2}}[\kappa]$ of the measured channel and the estimated FCCFs $\hat{r}_{f'_{i_1,i_2}}[\kappa]$ of the multichannel 2D AR models. The estimated TCCFs $\hat{r}_{t_{i_1,i_2}}[\iota]$ and FCCFs $\hat{r}_{f'_{i_1,i_2}}[\kappa]$ of the multichannel 2D AR(5,1) and AR(10,4) models presented in Fig. 4.17 can be compared to the corresponding correlation functions in Fig. 3.11.

The estimated 2D delay-Doppler PSDs $\hat{P}_h(\tau', f_d)$ of the 2D AR(5,1) and 2D AR(10,4) models are depicted in Fig 4.18. Correspondingly, the estimated Doppler PSDs $\hat{P}_{h_{f_d}}(f_d)$ and the delay PSDs $\hat{P}_{h_{\tau'}}(\tau')$ of the multichannel 2D AR models are shown together with the Doppler PSD $\hat{\hat{P}}_{h_{f_d}}(f_d)$ and the delay PSD $\hat{\hat{P}}_{h_{\tau'}}(\tau')$ of the measured channel, estimated from the TVFR $\tilde{h}_{1,1}[m,n]$, in Figs. 4.19 and 4.20, respectively. Clearly, the order of the multichannel 2D AR(5,1) model is underestimated w.r.t. time (see the comment in Subsection 4.7.2 regarding the results presented in Fig. 4.9).

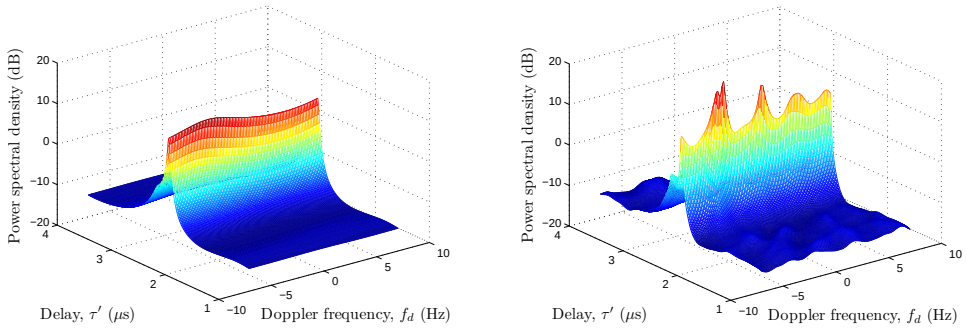

(a) (b)

Figure 4.18: The delay-Doppler PSD $\hat{P}_h(\tau', f_d)$ of the (a) 2D AR(5,1) model and (b) 2D AR(10,4) (micro/pico cell site – passageway).

We further analyze the results depicted in Figs. 4.19 and 4.20 in terms of the first and second order spectral moments presented in Table 4.5. Clearly, the estimated spectral moments of the multichannel 2D AR(10,4) model are closer to the corresponding spectral moments of the measured channel, compared to the spectral moments obtained for the 2D AR(5,1) model and the channel simulator based on the model (3.7). As in the previous subsections, the squared delay spread of the channel simulation model (3.7) is smaller than the analogues characteristic of the measured channel and the multichannel 2D AR models. Also note that in spite of the poor agreement between the Doppler PSD $\hat{P}_{h_{f_d}}(f_d)$ of the 2D AR(5,1) model and the estimated Doppler PSD $\hat{\hat{P}}_{h_{f_d}}(f_d)$ of the measured channel in Fig. 4.19, the Doppler spectrum moments of the AR(5,1) model are rather close

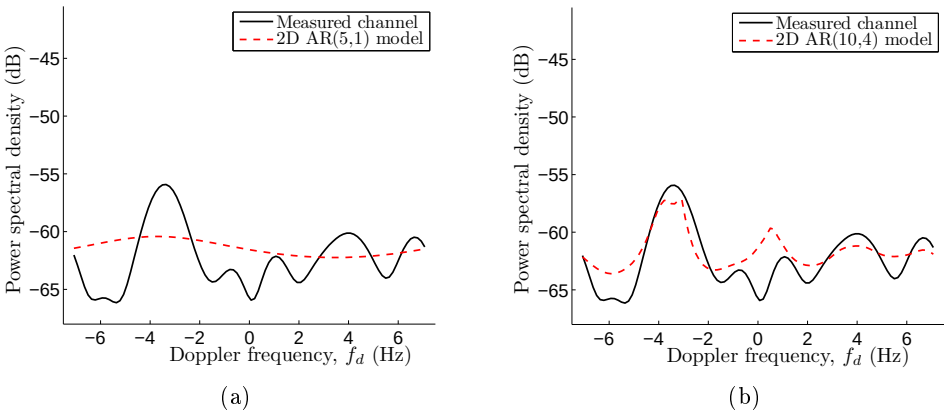

Figure 4.19: The Doppler PSDs for the multichannel 2D AR(p_1,p_2) models and the measured channel (micro/pico cell site – passageway).

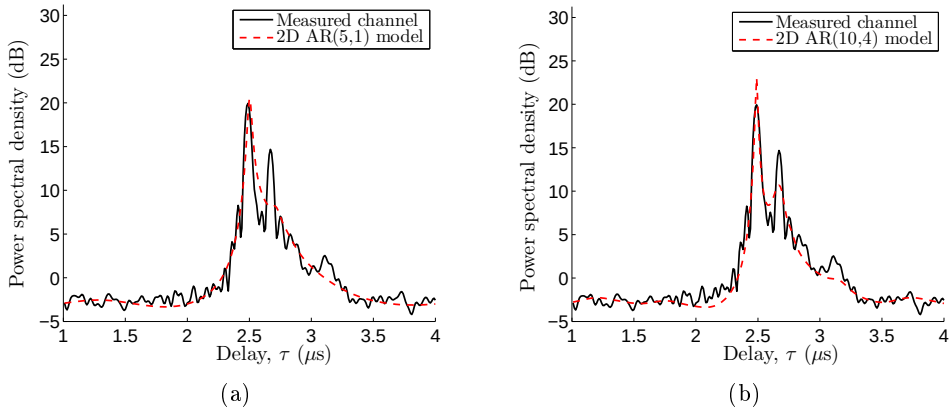

Figure 4.20: The delay PSDs for the multichannel 2D AR(p_1,p_2) models and the measured channel (micro/pico cell site – passageway).

to the estimated average Doppler shift and the Doppler spread of the measured channel.

The CDFs of the instantaneous channel capacity (3.48) of the multichannel 2D AR(5,1) and 2D AR(10,4) models as well as the instantaneous capacity CDF of the measured channel are shown in Fig. 4.21. The results presented in Fig. 4.21 are comparable to those obtained for the channel simulator developed in Subsection 3.6.3 and depicted in Fig. 3.13. The estimated mean values and the standard deviations of the capacity for the 2D AR(5,1), 2D AR(10,4), and the measured channel are shown in Table 4.6.

Table 4.5: Spectral moments (micro/pico cell site – passageway).

	Measured channel	2D AR(5,1)	2D AR(10,4)	Channel simulator (3.7)
Doppler shift, μ_{f_d} (Hz)	-0.275 $[-0.315, -0.24]$	-0.47	-0.29	-0.63
Squared Doppler spread, $\sigma^2_{f_d}$ (Hz^2)	16 $[15.88, 16.15]$	16.82	15.8	15.23
Delay shift, $\mu_{\tau'}$ (μs)	2.57 $[2.564, 2.57]$	2.56	2.55	2.55
Squared delay spread, $\sigma^2_{\tau'}$ (μs^2)	0.022 $[0.021, 0.023]$	0.019	0.018	0.013

Table 4.6: Estimated mean and standard deviation of the capacity (micro/pico cell site – passageway).

	Measured channel	2D AR(6,1)	2D AR(9,5)
Mean, μ_C (bps/Hz)	8.45	8.7	8.7
Standard deviation, σ_C (bps/Hz)	1.16	0.825	0.79

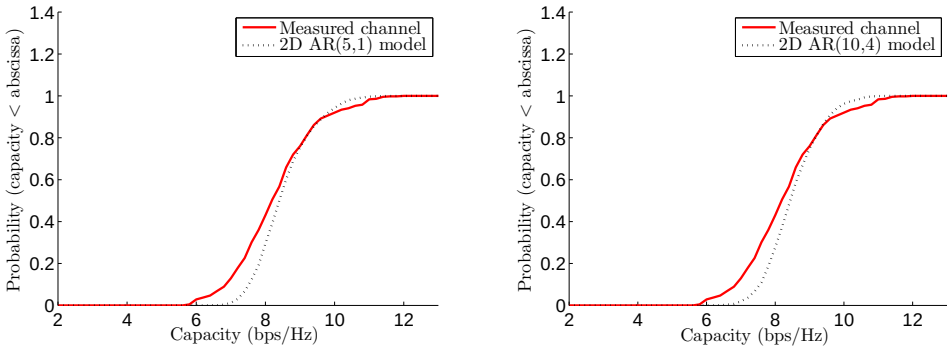

(a) (b)

Figure 4.21: Capacity CDFs of the multichannel 2D AR(p_1,p_2) models and the measured channel for an SNR $\rho = 20$ dB (micro/pico cell site – passageway).

4.7.5 Indoor Cell Site

For the real-world channel considered in this subsection, the multichannel 2D AR(5,3) and the 2D AR(15,3) models have been chosen based on the results provided by the cross-validation method and the CMF rule (Subsection 4.7.1), respectively. Both models are BIBO stable according to the stability test (4.23).

In Fig. 4.22, several TCCFs $\hat{\tilde{r}}_{t_{i_1,i_2}}[\iota]$ and FCCFs $\hat{\tilde{r}}_{f'_{i_1,i_2}}[\kappa]$, estimated from the measurement data, as well as the corresponding estimated TCCFs $\hat{r}_{t_{i_1,i_2}}[\iota]$ and

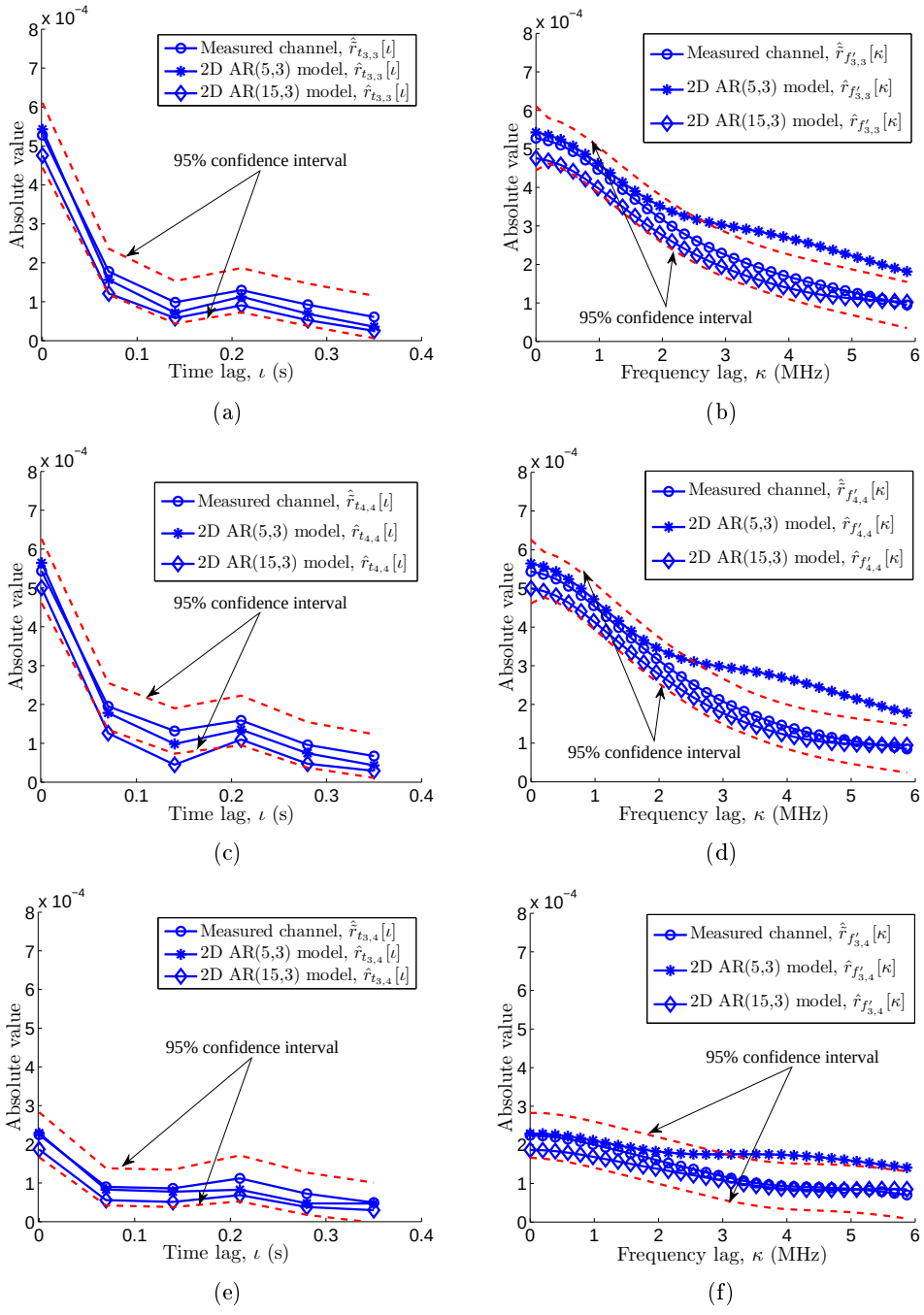

Figure 4.22: Examples of the estimated TCCFs and FCCFs of the physical channel and the corresponding TCCFs and FCCFs of the multichannel 2D AR(p_1,p_2) models (indoor cell site).

the FCCFs $\hat{r}_{f'_{i_1,i_2}}[\kappa]$ of the multichannel 2D AR(5,3) and 2D AR(15,3) models are depicted. It can be observed that while the increase in the model order from (5,3) to (15,3) improves the agreement between the FCCFs $\hat{\hat{r}}_{f'_{i_1,i_2}}[\kappa]$ and $\hat{r}_{f'_{i_1,i_2}}[\kappa]$, it worsens the fitting between the estimated TCCFs of the multichannel 2D AR models and the estimated TCCFs of the measured channel. The results presented in Fig. 4.22 can be compared to the results shown in Fig. 3.15

The estimated 2D delay-Doppler PSDs $\hat{P}_h(\tau', f_d)$ of the 2D AR(5,3) and 2D AR(15,3) models are demonstrated in Fig 4.23. The estimated single-dimensional Doppler PSDs and the delay PSDs are shown in Figs. 4.19 and 4.20, respectively, for the multichannel 2D AR(5,3) and AR(15,3) models as well as the corresponding single-dimensional PSDs estimated from the measured TVFR.

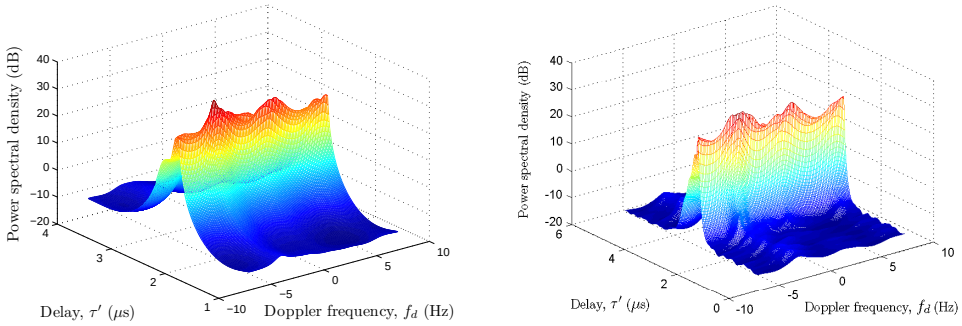

(a) (b)

Figure 4.23: The delay-Doppler PSD $\hat{P}_h(\tau', f_d)$ of the (a) 2D AR(5,1) model; (b) 2D AR(10,4) (indoor cell site).

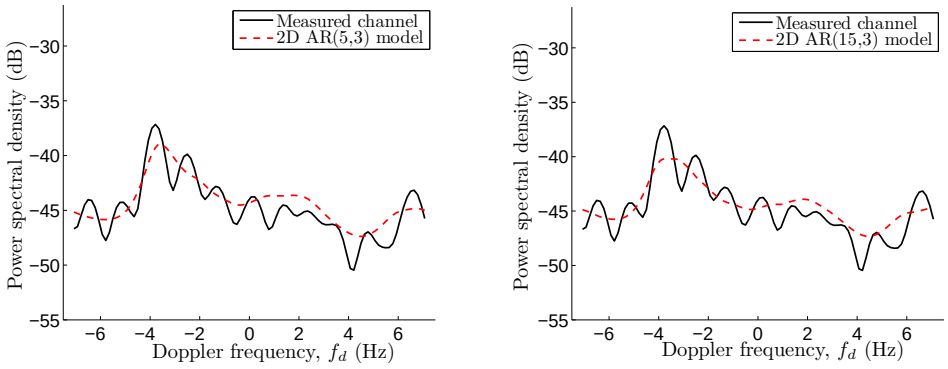

(a) (b)

Figure 4.24: The Doppler PSDs for the multichannel 2D AR(p_1,p_2) models and the measured channel (indoor cell site).

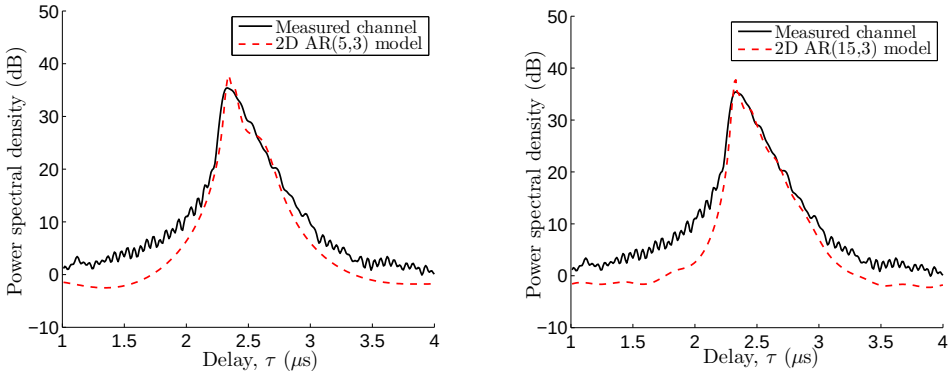

Figure 4.25: The delay PSDs for the multichannel 2D AR(p_1,p_2) models and the measured channel (indoor cell site).

The estimated first and second order spectral moments for the measured channel and the multichannel 2D AR models are presented in Table 4.7. As in the previous subsections, in Table 4.7 we include the spectral moments calculated for the channel simulator based on the model (3.7) developed in Subsection 3.6.4 based on the same measured TVFR. It appears that the increase in the order of the multichannel 2D AR model from (5,3) to (15,3) does not significantly influence the values of the estimated spectrum moments. Again, the calculated delay spread of the channel simulator (3.7) is smaller compared to the delay spread estimated from the measurement data and to the delay spread of the multichannel 2D AR models.

Table 4.7: Spectral moments (indoor cell site).

	Measured channel	2D AR(5,3)	2D AR(15,3)	Channel simulator (3.7)
Doppler shift, μ_{f_d} (Hz)	-1.23 $[-1.27, -1.2]$	-0.88	-0.845	-1.4
Squared Doppler spread, $\sigma^2_{f_d}$ (Hz^2)	13.5 $[13.33, 13.66]$	13.4	14.2	12.12
Delay shift, $\mu_{\tau'}$ (μs)	2.394 $[2.391, 2.396]$	2.394	2.392	2.383
Squared delay spread, $\sigma^2_{\tau'}$ (μs^2)	0.097 $[0.094, 0.1]$	0.083	0.086	0.057

In Fig. 4.26, the instantaneous channel capacity CDFs (3.48) of the multichannel 2D AR(5,3) and AR(15,3) models are shown together with the instantaneous capacity CDF of the measured channel. As it can be seen from Fig. 4.26, the instantaneous channel capacity CDFs of the 2D AR(5,3) and AR(15,3) models are close to the instantaneous channel capacity CDF of the measured channel.

The graphs presented in Fig. 4.26 can be compared to the capacity CDF of the channel simulator based on the model (3.7) depicted in Fig. 3.17. The estimated mean values and the standard deviations of the capacity for the 2D AR(5,3), 2D AR(15,3), and the measured channel are presented in Table 4.8.

Table 4.8: Estimated mean and standard deviation of the capacity (indoor cell site).

	Measured channel	2D AR(6,1)	2D AR(9,5)
Mean, μ_C (bps/Hz)	8.17	8.15	8.14
Standard deviation, σ_C (bps/Hz)	0.83	1	0.85

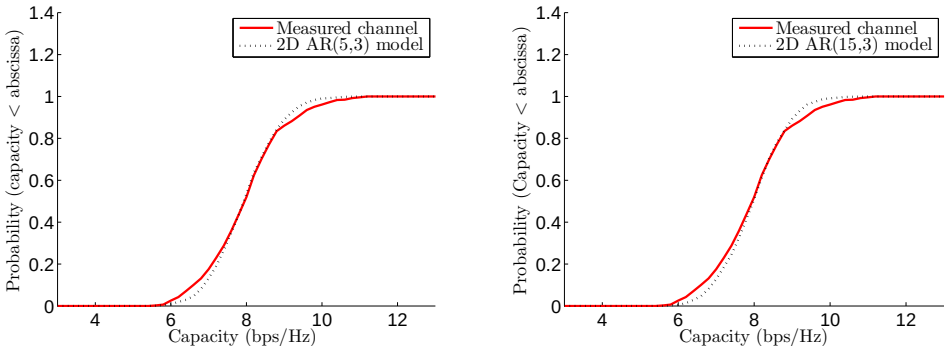

Figure 4.26: Capacity CDFs of the multichannel 2D AR(p_1,p_2) models and the measured channel for the SNR $\rho = 20$ dB (indoor cell site).

4.8 Concluding Remarks

In this chapter, we have described the use of the multichannel 2D AR model for simulating MIMO wideband mobile radio channels. The parameters of the multichannel 2D AR model are estimated from the measured TVFR of a real-world prototype channel. The estimates of the multichannel 2D AR model parameters can be obtained by solving the set of Yule-Walker normal equations or, alternatively, by employing the PEM method.

One of the main problems associated with the multichannel 2D AR model is a possible instability of a resulting channel simulator. The stabilization procedure proposed in this chapter can be used to stabilize the multichannel 2D AR model. However, due to the large number of the model parameters, the stabilization procedure might be time consuming even for the multichannel 2D AR models of a moderate order, say $p_1 > 5$, $p_2 > 5$ for 2×2 MIMO systems.

If the multichannel 2D AR model is to be used for generating realizations of the channel TVFR, which do not exceed the duration of several transmitted symbols, then the method of synthesizing the TVFR in the delay-Doppler domain can be employed. This method is based on the observation that the lack of the guaranteed stability of the multichannel 2D AR model is not a serious drawback for estimating the delay-Doppler PSD of a wireless channel. Thus, a spectrum shaping filter can be created and applied to an input white noise in the delay-Doppler domain.

In this chapter, we have considered the important characteristics of several multichannel 2D AR models developed based on the TVFRs of the real-world channels measured in different propagation environments. The results presented in this chapter can be compared to the performance results for the stochastic channel simulators designed in Chapter 3. Below is a summary of the key observations related to the development and performance of multichannel 2D AR models:

- The multichannel 2D AR model is generally less efficient in synthesizing realizations of the TVFR of a wireless MIMO channel than the channel simulation model (3.7) described in Chapter 3. This is due to the fact that a relatively large amount of data has to be stored in the memory for calculating the samples of the channel TVFR. This is true for multichannel 2D AR models represented in the form of (4.3) or (4.22) as well as in the form of the spectrum shaping filter (4.27).

- Estimating the parameters of the multichannel 2D AR(p_1,p_2) model can be characterized as a moderate complexity computational problem. For example, the computational cost of estimating the model parameters by using the PEM method described in Subsection 4.3.2 can roughly be estimated as

$$O\left\{(M-p_1)(N-p_2)N_T^2N_R^2\left[(p_1p_2+p_1+p_2)^2+(p_1p_2+p_1+p_2)+1)\right]\right\}.$$

- It has been observed that the multichannel 2D AR model even of a relatively low order, which provides only a very smooth estimate of the delay-Doppler PSD of a real-world prototype channel, is often sufficient for adequate representation of the important statistics of the prototype channel.

Chapter 5

Velocity Estimation in Wideband Mobile Stations Equipped With Multiple Antennas

5.1 Introduction

During the last two decades, a number of publications has been devoted to the problem of estimating the MS velocity from the received signal in cellular networks. Such interest is due to the fact that significant improvements in the performance of wireless communication systems are possible if the MS speed is known. For example, the knowledge of the MS velocity allows to minimize the number of handovers in multilayer cellular networks. Furthermore, the information about the MS speed can be used to tune up different adaptive signal processing algorithms implemented in the transceivers.

Several methods for estimating the MS velocity can be found in the literature, see e.g., [80–87]. The performance evaluation of some of the estimation algorithms, as well as their comparison, are presented in [88, Chapter 5] and also in [89]. According to the theoretical and simulation-based analysis provided in the references, the main factors that cause degradation in the performance of the available velocity estimators are the additive noise, presence of shadowing, and the nonisotropic scattering environment. An additional factor, which is often omitted from the consideration, is the limited time interval over which the channel statistics have to be estimated.

Although the existing velocity estimators can be employed without any changes in wideband MIMO systems, it is of interest to investigate how additional *degrees of freedom*, e.g., signal bandwidth and multiple antennas at a MS, can be utilized to improve the accuracy of the velocity estimation for different propagation scenarios. The results of the investigations might be useful in the context of

developing the newly emerged Ultra Mobile Broadband (UMB) [90] and mobile WiMAX [91] technologies. It is worth mentioning that the problem of improving the robustness of MS velocity estimators by taking advantage of a wide bandwidth and antenna arrays (at the BS), has been recently analyzed in [92].

In this chapter, we describe an MS velocity estimation method designed for wideband MIMO communication systems [93]. In our method, the speed of the MS is estimated using the well-known relationship between the DOAs and the Doppler shifts that characterizes the multipath signal components. According to [4, Chapter 7], the distribution of the DOAs is a function of delays. The assumption that we make regarding the propagation environment is that the multipath components arriving at the MS from a certain bounded interval of DOAs can be uniquely identified with a certain range of propagation delays. This assumption allows us to simplify the otherwise complicated parameter estimation algorithms that can be applied to simultaneously estimate the DOAs and the corresponding Doppler frequencies of the multipath components. The performance of the proposed MS velocity estimator has been evaluated on simulated channel TVFRs. The presented results demonstrate that the suggested velocity estimation algorithm is less sensitive to noise and nonisotropic scattering compared to several other known methods. It is also shown how the performance of the proposed MS speed estimator is affected by the available signal bandwidth.

The rest of the chapter is organized as follows. In Section 5.2, we describe the model of the channel TVFR. The MS velocity estimation method is presented in Section 5.3. Section 5.4 provides the results of the performance evaluation. Concluding remarks are given in Section 5.5.

5.2 The Time-Variant Frequency Response of the Channel

In this section, we establish the model for the TVFR of a mobile MIMO radio propagation channel. In MIMO systems, the MS and the BS are equipped with antenna arrays consisting of N_{MS} and N_{BS} elements, respectively. For simplicity reasons and without loss of generality, we let $N_{BS} = 1$.

It is assumed that the TVFR vector $\mathbf{H}(f', t) = [H_1(f', t), \ldots, H_{N_{MS}}(f', t)]^T$ of the mobile radio channel consists of a finite number L of multipath components (*cf.* (3.7)), i.e.,

$$\mathbf{H}(f', t) = \sum_{n=1}^{L} \mathbf{g}(\phi_l) c_l e^{j(2\pi f_{d_l} t - 2\pi f' \tau'_l + \theta_l)} \tag{5.1}$$

where f' and t denote the frequency and time variables, respectively, and $H_i(f', t)$, $i = 1, \ldots, N_{MS}$, is the TVFR of the i-th subchannel. Each of the L multipath

components is characterized by the path gain c_l, Doppler frequency f_{d_l}, propagation delay τ_l', phase shift θ_l, and the DOA ϕ_l. Here, we implicitly assume that the planar electromagnetic waves propagate horizontally.

The steering vector $\mathbf{g}(\phi)$ in (5.1) is defined as [94]

$$\mathbf{g}(\phi) = [g_1(\phi)e^{-jk_0\langle \mathbf{k},\mathbf{r}_1\rangle}, \ldots, g_{N_{MS}}(\phi)e^{-jk_0\langle \mathbf{k},\mathbf{r}_{N_{MS}}\rangle}]^T \tag{5.2}$$

where the vector $\mathbf{r}_i$, $i = 1, \ldots, N_{MS}$, specifies the location of the i-th MS antenna array element with respect to a chosen reference point; $\mathbf{k}$ is a unit vector pointing in the direction of the wave propagation; k_0 is the free-space wavenumber, related to the wavelength λ by $k_0 = 2\pi/\lambda$. The radiation pattern of the i-th antenna array element is given by $g_i(\phi)$, $i = 1, \ldots, N_{MS}$. If the MS is equipped with a uniform linear array (ULA), we presume that the radiation pattern of the MS antenna array is effectively restricted to the range of $\phi \in [-\pi/2, \pi/2]$ (see, e.g., [65]), where the DOA ϕ is measured w.r.t. the normal to the linear antenna array.

In practice, the TVFR $\mathbf{H}(f', t)$ has to be estimated, e.g., using pilot tones as in orthogonal frequency division multiplexing (OFDM) communication systems [4]. The errors in the estimated TVFR $\hat{\mathbf{H}}(f', t)$ are represented by a complex spatially uncorrelated (independent) additive white Gaussian noise (AWGN) vector $\mathbf{w}(f', t)$, i.e.,

$$\hat{\mathbf{H}}(f', t) = \mathbf{H}(f', t) + \mathbf{w}(f', t) \tag{5.3}$$

where each component of the vector $\mathbf{w}(f', t) = [w_1(f', t), \ldots, w_{N_{MS}}(f', t)]^T$ has zero-mean and variance $2\sigma_w^2$. Similar to the previous chapters, we assume that the TVFR $\mathbf{H}(f', t)$ is estimated at discrete frequencies $f_m' = -B/2 + m\triangle f' \in [-B/2, B/2]$, $m = 0, \ldots, M-1$, and at discrete time instances $t_n = n\triangle t \in [0, T]$, $n = 0, \ldots, N-1$, where B and T denote the frequency bandwidth and the time observation interval, respectively. The frequency sampling interval $\triangle f'$ and the time sampling interval $\triangle t$ are constants. The time sampling interval $\triangle t$ is supposed to be less than $1/(2f_{d_{\max}})$ with the maximum Doppler frequency defined as $f_{d_{\max}} = v/\lambda_c$, where v is the speed of the MS and $\lambda_c = c/f_c$[1] with c denoting the speed of light.

5.3 Velocity Estimation Algorithm

In this section, we describe the algorithm proposed for estimating the MS velocity. The basic idea behind the algorithm comes from the well-known relationship between the Doppler frequency f_{d_l} and the DOA ϕ_l of the l-th multipath component in (5.1). Under the condition that the Doppler effect is caused only by the

[1] In a typical wideband communication system, the inequality $B/f_c \ll 1$ still holds, where f_c is the center frequency of the modulated bandpass signal.

MS movement, this relationship can be expressed as

$$f_{d_l} = \frac{v}{\lambda_c}\cos(\phi_l - \alpha_v) \tag{5.4}$$

where v is the MS velocity and α_v designates the direction of the MS movement.

5.3.1 Least-Squares Velocity Estimator

Suppose that estimates of the DOAs $\{\hat{\phi}_k\}$ and the Doppler frequencies $\{\hat{f}_{d_k}\}$ of $K \leq L$ multipath components in (5.1) are available. The least-squares (LS) estimator of the MS velocity v and the direction of the MS movement α_v can be expressed as

$$\{\hat{v}, \hat{\alpha}_v\} = \arg\min_{\{v,\alpha_v\}} \left\{ \sum_{k=1}^{K} (\hat{f}_{d_k} - \frac{v}{\lambda_c}\cos(\hat{\phi}_k - \alpha_v))^2 \right\}. \tag{5.5}$$

Using the identity

$$\frac{v}{\lambda_c}\cos(\hat{\phi}_k - \alpha_v) = \frac{v}{\lambda_c}[\cos(\hat{\phi}_k)\cos(\alpha_v) + \sin(\hat{\phi}_k)\sin(\alpha_v)] \tag{5.6}$$

we can define the system of linear equations

$$\mathbf{A}\mathbf{b} = \mathbf{f}_d \tag{5.7}$$

where

$$\mathbf{A} = \begin{bmatrix} \cos(\hat{\phi}_1) & \sin(\hat{\phi}_1) \\ \vdots & \vdots \\ \cos(\hat{\phi}_K) & \sin(\hat{\phi}_K) \end{bmatrix}, \tag{5.8}$$

$$\mathbf{b} \equiv \begin{bmatrix} b_1 \\ b_2 \end{bmatrix} = \begin{bmatrix} v/\lambda_c \cos(\alpha_v) \\ v/\lambda_c \sin(\alpha_v) \end{bmatrix}, \tag{5.9}$$

and

$$\mathbf{f}_d = [\hat{f}_{d_1}, \ldots, \hat{f}_{d_K}]^T. \tag{5.10}$$

The LS solution of (5.7) is given by[2]

$$\hat{\mathbf{b}} = (\mathbf{A}^T\mathbf{A})^{-1}\mathbf{A}^T\mathbf{f}_d. \tag{5.11}$$

Thus, the LS estimate of the MS velocity that solves the minimization problem

[2]Since uncertainties due to the estimation errors are present in both the matrix $\mathbf{A}$ in (5.9) and the vector $\mathbf{f}_d$ in (5.11), it makes sense to find the total least-squares (TLS) [95] solution for the vector $\mathbf{b}$.

in (5.5) can be written as

$$\hat{v} = \lambda_c \sqrt{\hat{b}_1^2 + \hat{b}_2^2} \tag{5.12a}$$

$$\hat{\alpha}_v = \arctan\left(\frac{\hat{b}_2}{\hat{b}_1}\right). \tag{5.12b}$$

5.3.2 Estimation of the Direction-of-Arrivals and the Doppler Frequencies

Hypothetically, it seems to be an attractive approach to select the multipath components in (5.1) clustered around a known DOA $\tilde{\phi}_k$ by using, e.g., beamforming techniques [96]. Then, assuming the selected multipath components have approximately the same Doppler frequency, it is relatively easy to obtain the estimate $\hat{f}_{d_k}$. In practice, however, the small aperture (see, e.g., [94]) of an antenna array at the MS makes it impossible to construct a spatial filter (beamformer) with good selectivity properties[3] in the angular domain. On the other hand, in wideband communication systems, the 'aperture' in the frequency domain, determined by the signal bandwidth B, is relatively large. Thus, the multipath components in (5.1) with the propagation delays clustered around a known delay $\tilde{\tau}'_k$ can be selected. Furthermore, we assume that the Doppler spectrum of the multipath components clustered in the delay domain around $\tilde{\tau}'_k$ possesses a global maximum, which can be associated with a certain Doppler frequency f_{d_k}.

The above-mentioned considerations have led to the following algorithm for estimating the DOAs $\{\phi_k\}$ and the Doppler frequencies $\{f_{d_k}\}$, $k = 1, \ldots, K$.

Step 1. Select the multipath components with the propagation delays, which are close to a specified delay $\tilde{\tau}'_k$ chosen as described below. For this purpose, pass the estimated TVFR $\hat{H}_i[m,n] = \hat{H}_i[m\triangle f', n\triangle t]$, $i = 1, \ldots, N_{MS}$, of the i-th subchannel through a delay bandpass filter with the transfer function centered at $\tilde{\tau}'_k$. The filtering operation can be implemented in the form of a discrete Fourier transform (DFT) as

$$y_i[n;\tilde{\tau}'_k] = \frac{1}{M}\sum_{m=0}^{M-1} \hat{H}_i[m,n] e^{-j2\pi\tilde{\tau}'_k \triangle f' m} \tag{5.13}$$

where $y_i[n;\tilde{\tau}'_k]$ denotes the sampled signal at the output of the bandpass filter.

Step 2. Estimate the DOA ϕ_k. Assuming the antenna array calibration data as well as the locations of the antenna elements w.r.t. the reference point is available at the MS, the DOA ϕ_k can be estimated using the beamforming method

[3] By the selectivity properties, we understand the width of the main lobe and the level of the side lobes of the filter transfer function.

(see, e.g., [94, 96])

$$\hat{\phi}_k = \arg\max_{\phi_k} \left\{ \frac{\mathbf{g}^H(\phi_k) \left(\frac{1}{N} \sum_{n=0}^{N-1} \mathbf{y}[n;\tilde{\tau}'_k] \mathbf{y}^H[n;\tilde{\tau}'_k] \right) \mathbf{g}(\phi_k)}{\mathbf{g}^H(\phi_k)\mathbf{g}(\phi_k)} \right\} \tag{5.14}$$

where $\mathbf{y}[k;\tilde{\tau}'_k] = [y_1[n;\tilde{\tau}'_k], \ldots, y_{N_{MS}}[n;\tilde{\tau}'_k]]^T$, $\mathbf{g}(\phi)$ is defined in (5.2).

Step 3. Estimate the Doppler frequency f_{d_k} by allocating a maximum of the periodogram, i.e.,

$$\hat{f}_{d_k} = \arg\max_{f_{d_k}} \left\{ \frac{1}{N} \left| \sum_{n=0}^{N-1} z[n;\tilde{\tau}'_k, \hat{\phi}_k] e^{j2\pi f_{d_k} \triangle t\, n} \right|^2 \right\} \tag{5.15}$$

where the sampled function $z[n;\tilde{\tau}'_k, \hat{\phi}_k]$ is given by

$$z[n;\tilde{\tau}'_k, \hat{\phi}_k] = \mathbf{g}^H(\hat{\phi}_k)\mathbf{y}[n;\tilde{\tau}'_k]. \tag{5.16}$$

The Steps 1–3 presented above are illustrated with a signal flow diagram in Fig. 5.1.

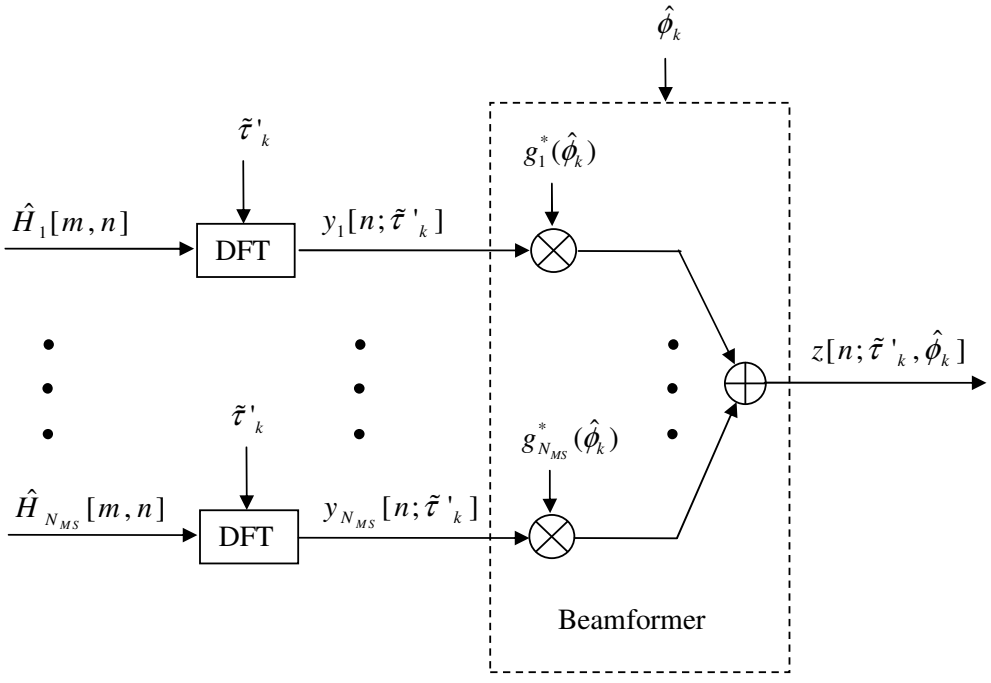

Figure 5.1: Signal flow diagram for estimating the DOAs and the Doppler frequencies.

Note that the choice of the delay bandpass filter used in Step 1 was mainly governed by the simplicity of implementation. For example, the DFT in Step 1

can be readily computed using the fast Fourier transform (FFT). It might be possible, however, to improve the characteristics of the filter, e.g., by using data windowing [65, 79].

Based on the conducted simulations, we suggest to use as $\{\tilde{\tau}'_k\}$ the locations of the K highest peaks in the impulse response of the first subchannel obtained by taking the FFT of $\hat{H}_1[m,n]$ w.r.t. the frequency index m.

On obtaining the estimates $\{\hat{\phi}_k, \hat{f}_{d_k}\}$, $k = 1, \ldots, K$, the MS velocity is determined as described in Subsection 5.3.1.

5.4 Simulation Results

In this section, we present the results of the performance evaluation for the MS velocity estimation algorithm described in the previous section.

The performance of the proposed MS velocity estimator has been assessed on a number of TVFRs $\mathbf{H}(f', t)$ generated using a simple geometrical model. In this model, the distance D between the BS and the MS is assumed to be 750 m. The MS is equipped with a ULA consisting of two ($N_{MS} = 2$) omnidirectional antenna elements separated by a half wavelength distance. The signal frequency band is centered at $f'_c = 2$ GHz. The normal to the MS antenna array points towards the BS. The scatterers are uniformly distributed in the region between the BS and the MS. The dimensions of the region are determined by the maximum allowed propagation delay $\tau'_{\max} = 1/\triangle f'$. Thus, the DOAs $\{\phi_l\}$ of the multipath components [see (5.1)] lie in the range $[-\pi/2, \pi/2]$ and, therefore, can be unambiguously estimated. The path gains $\{c_l\}$ are realizations of i.i.d. random variables, each having a uniform distribution in the interval $[0, 1]$. The path gains are first normalized, so that $\sum_{l=1}^{L} c_l^2 = 1$, then each of them is multiplied by the exponential factor $\exp[\log(0.1)(\tau'_l - \tau'_{\min})/(\tau'_{\max} - \tau'_{\min})]$, where $\tau'_{\min} = D/c$. The chosen multiplication factor represents the exponential decay normally observed in the measured channel power-delay profile (PDP) [97]. The direction of the MS movement α_v is an outcome of a random number generator having a uniform distribution in the interval $[0, 2\pi)$. The other parameters are specified as below:

- Number of multipath components: $L = 230$;
- Time interval between snapshots: $\triangle t = 1$ ms;
- Number of snapshots: $N = 100$;
- Interval between frequencies: $\triangle f' = 3.125 \cdot 10^5$ Hz.

Note that the propagation delay τ'_l of the l-th multipath component is a function of the DOA ϕ_l in the synthesized TVFR of the channel. An example of the simulated multipath components in the delay-DOA plane is depicted in Fig. 5.2.

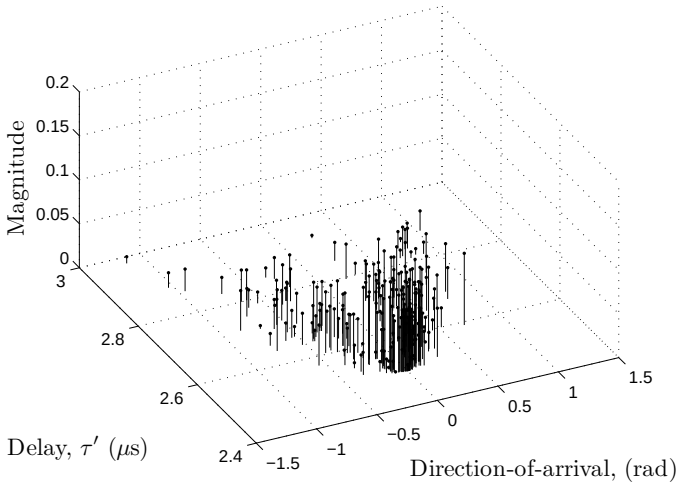

Figure 5.2: Example of the simulated multipath components in the delay-DOA plane.

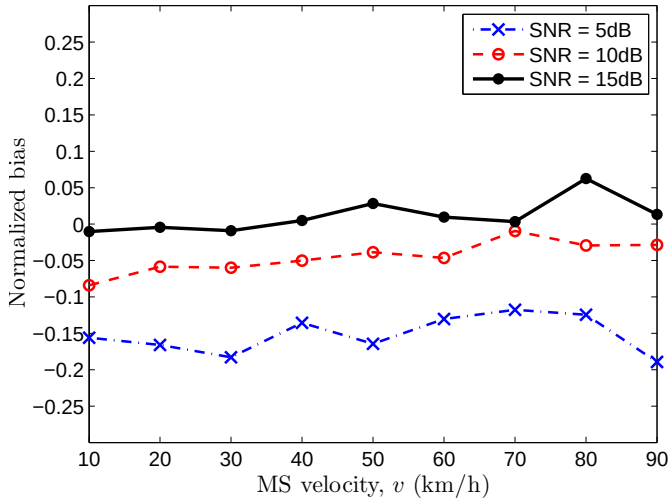

Figure 5.3: Normalized bias as a function of the MS velocity and the SNR (B = 20 MHz).

The performance of the MS velocity estimator is evaluated in terms of the normalized bias $E\{(\hat{v}-v)/v\}$ and the mean-squared relative error (MSRE) $E\{[(\hat{v}-v)/v]^2\}$ of the estimates. These two characteristics are shown in Figs. 5.3 and 5.4, respectively, for different values of the SNR. It can be observed that the normalized bias and the MSRE are almost independent of the actual MS speed. As expected, with increasing SNR, the velocity estimates become less biased and have smaller MSRE.

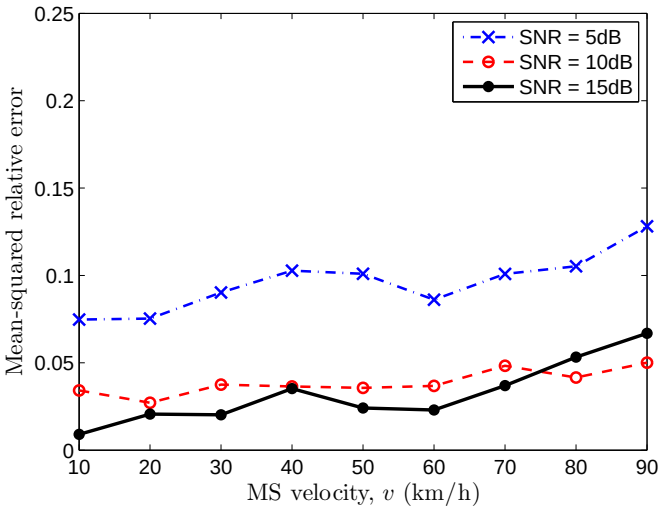

Figure 5.4: Mean-squared relative error as a function of the MS velocity and the SNR ($B = 20$ MHz).

Figures 5.5 and 5.6 demonstrate the degree to which the performance of the proposed velocity estimation algorithm depends on the available signal bandwidth B. It can be seen that for $B \geq 15$ MHz the normalized bias and the MSRE do not change significantly. A somewhat greater MSRE in the velocity estimates is observed for $B = 5$ MHz.

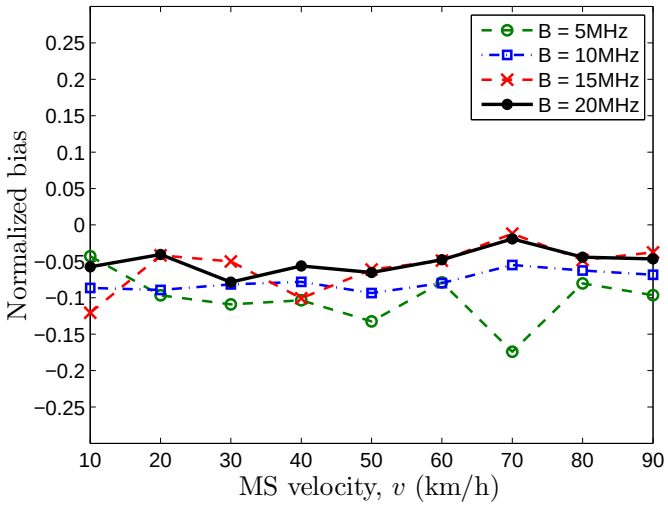

Figure 5.5: Normalized bias as a function of the MS velocity and the bandwidth (SNR = 10 dB).

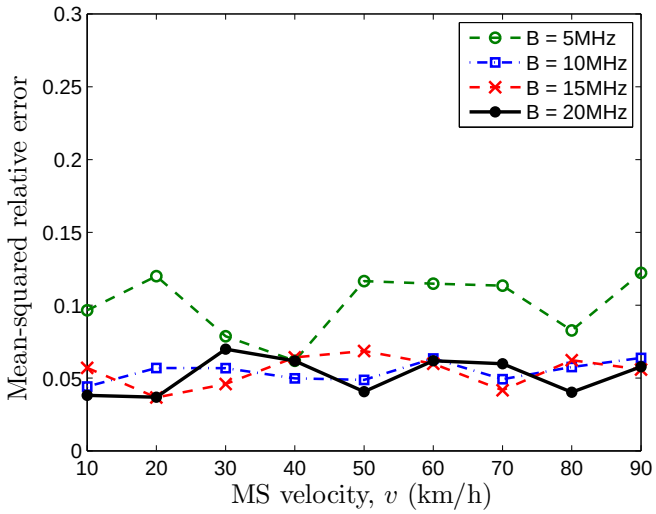

Figure 5.6: Mean-squared relative error as a function of the MS velocity and the bandwidth (SNR = 10 dB).

We have also compared the performance of the proposed MS velocity estimation algorithm with several existing methods, namely: the instantaneous frequency (IF) method [85], the level-crossing rate (LCR) method [80], the zero-crossing rate (ZCR) method [80], and the covariance-based (COV) estimation method [81][4]. All of these methods assume isotropic scattering. To satisfy this assumption, the performances of the velocity estimators have been compared based on the TVFRs, generated using the geometrical one-ring simulation model [35]. In this model, the scatterers are located on a ring. The DOAs $\{\phi_n\}$ are realizations of i.i.d. random variables, each having a uniform distribution in the interval $[-\pi, \pi]$. All path gains $\{c_n\}$ are equal to $1/\sqrt{N}$. To avoid the ambiguity in the estimation of the DOAs $\{\phi_n\}$, three neighboring elements of an 8-element omnidirectional uniform circular array (UCA) are used as the MS antenna. The other simulation model parameters are unchanged compared to the channel simulator described above. The Rician K-factor, which is zero in this propagation scenario, is assumed known in the IF velocity estimation method.

The normalized bias and the MSRE of the velocity estimates obtained using the aforementioned estimation methods are depicted in Figs. 5.7 and 5.8, respectively. The performance results for the IF, LCR, ZCR, and COV methods are in agreement with the similar results presented in [88, Chapter 5]. It can be observed that the proposed velocity estimation method demonstrates smaller bias and smaller MSRE in the broad range of the considered MS speeds.

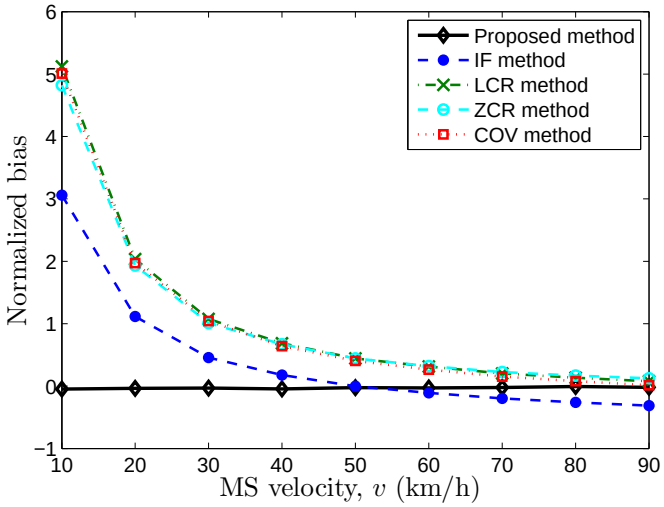

Figure 5.7: Normalized bias as a function of the MS velocity (SNR = 10 dB, B = 10 MHz).

[4]The channel statistics required for the velocity estimation by using the IF, LCR, ZCR, and COV methods have been averaged over M frequencies and N_{MS} subchannels.

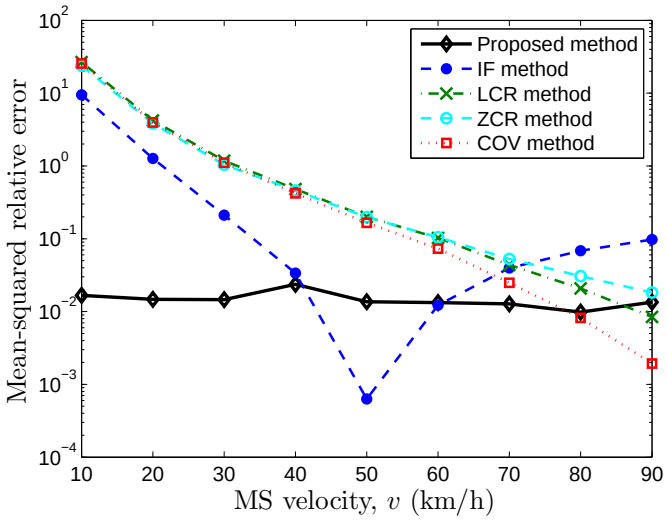

Figure 5.8: Mean-squared relative error as a function of the MS velocity (SNR = 10 dB, B = 10 MHz).

5.5 Concluding Remarks

In this chapter, we have considered a method for the velocity estimation in MSs equipped with multiple antennas and operating over wideband communication channels. The velocity is estimated by employing the well-known relationships between the DOAs, the MS speed, and the Doppler frequencies of the multipath components representing the TVFR of the channel. The method is based on the assumption that the Doppler spectrum of the multipath components clustered in the delay domain possesses a global maximum, which can be associated with a certain Doppler frequency.

Using computer simulations, the performance of the proposed MS velocity estimation method has been evaluated for different SNRs and different signal bandwidths. It has been demonstrated that the new estimation algorithm is not restricted to isotropic scattering scenarios. The proposed velocity estimator appears to be more robust to noise compared to several other existing MS speed estimation methods.

Chapter 6

Summary of Contributions and Outlook

6.1 Contributions

In this thesis, we have focused on the methods for designing measurement-based simulation models for wireless communication channels. Below is the summary of the contributions:

- A stationarity test has been proposed for real-world wireless communication channels. The test has been extended to validate the stationarity of MIMO wireless channels.
- The stationarity of the TVFRs of wireless communication channels measured in different propagation environments has been analyzed. We have found that the length of the channel stationarity intervals decreases as the number of antennas at the transmitter and the receiver increases.
- We have proposed a method for designing measurement-based stochastic channel simulation models for time-variant wideband MIMO wireless channels. The method has also been adapted for designing measurement-based stochastic channel simulators for wideband SISO and narrowband MIMO wireless channels.
- Experimental investigations based on simulations and measurement data corresponding to various propagation environments have shown that the proposed method can be used for creating simulators for wireless communication channels. Additionally, it has been demonstrated that the method is robust against white noise present in the measurement data.
- We have proposed the multichannel 2D AR model for simulating MIMO wideband mobile radio channels. The parameters of the multichannel 2D

AR model are estimated from the measured TVFR of a real-world channel. We have investigated the problem of a possible instability of the resulting multichannel 2D AR channel model. A model stabilization procedure has been proposed to stabilize the multichannel 2D AR model. Also, we have considered synthesizing the TVFRs of MIMO wideband mobile radio channels in the delay-Doppler domain. This channel simulation method can be used even in the case of unstable multichannel 2D AR models.

- We have analyzed the problem of estimating the velocity in wideband MSs equipped with multiple antennas. Using a developed velocity estimation algorithm, it has been demonstrated that the MS velocity estimations can be significantly improved as compared to the results provided by several existing methods.

6.2 Outlook

The results of the basic performance analysis for the stationarity test developed in Chapters 2 have been presented. However, a more detailed study of the test behavior under various conditions is required. The purpose of this study is to investigate the dependence between the level of confidence for an outcome of the stationarity test and the data sample size, i.e., the available signal bandwidth.

The part, which has not been covered in this dissertation, is the analysis of effects the errors in representing the correlation properties in time, frequency, and space produce on the performance of wireless receivers. Potentially, such analysis opens possibilities for optimizing the choice of the parameters in the algorithm presented in Chapters 3 and also for reducing the computational load associated with determining the parameters of the simulation model (3.7).

The methods for designing measurement-based channel simulators described in Chapters 3 and 4 allow synthesizing realizations of the channel TVFR with the correlation properties approximating those of a prototype real-world channel. Presuming that the first-order PDF of the TVFR of the prototype real-world channel can be approximated by the complex Gaussian PDF, the channel simulator developed by using one of the methods presented in this thesis allows an adequate analysis of the performance of wireless communication systems. The justification for the assumed Gaussianity of real-world radio channels, including empirical results obtained during multiple measurement campaigns, can be found in many references. However, it has also been reported in the literature that the estimated distribution of the TVFR of measured channels can significantly deviate from the complex Gaussian PDF. In [14] and [15], it is mentioned that a general approach to simulating stationary random processes with specified correlation properties and arbitrary first-order PDFs is based on a non-linear memoryless transformation of

Gaussian random processes. A possible application of this approach to the development of channel simulators for wireless communication channels constitutes an interesting research topic.

In the stochastic channel simulation model presented in Chapter 3, the space-time-frequency correlation matrix $\underline{\mathbf{R}}$ of the model is represented as a sum of the Kroneker products of the matrices $\mathbf{R}_{t_l}$, $\mathbf{R}_{f'_l}$, and $\mathbf{R}_{g_l}$ defined in (3.12), (3.13), (3.14), respectively. The correlation matrices $\mathbf{R}_{g_l}$, $l = 1, \ldots, L$, can be further parameterized in terms of the DOAs and DODs. Such parametrization can reduce the total number of the channel simulation model parameters. To investigate this possibility, the measurement data have to be supplemented with accurate calibration data for the transmitter and receiver equipment used in a measurement campaign.

The methods for designing measurement-based simulation models presented in this thesis are appropriate for generating wireless channels that satisfy the wide-sense stationarity assumption in the delay-Doppler domain. However, as it has been mentioned above, for real-world channels this assumption can be accepted only on limited intervals of time. Therefore, further research is necessary for developing measurement-based channel simulation models capable of reproducing the quasi-stationary (nonstationary) behavior of physical radio communication channels. This subject is particularly important for the mobile-to-mobile communications, where very short intervals of channel stationarity can be expected.

Appendix A

Measurement Equipment and Propagation Scenarios

The content of this appendix is a compilation of the relevant details, which have been found in the two technical reports provided by Telenor R&D together with the measurement data.

A.1 Measurement Equipment

The measurement campaign was conducted by Telenor R&D in Oslo, Norway, in July 2003. The measurements were performed using a wideband channel sounder with synchronized multiplexing of the transmitter and receiver antennas. The channel sounder was manufactured by SINTEF Telecom and Informatics, Trondheim, Norway, on assignment from Telenor R&D. Both the transmitter and the receiver were equipped with eight element uniform linear arrays consisting of vertically polarized rectangular patch antennas with an inter-element spacing of one-half wavelength. A linear frequency chirp signal was used for channel sounding. The block diagrams of the channel sounder transmitter and receiver are shown in Figs. A.1 and A.2, respectively.

The transmitter was mounted on a mobile trolley at the height of 1.5 m above ground. The receiver antenna was stationary and mounted on a 1.7 m high tripod mast. In addition, the following parameters describing the set up are listed below.

- Carrier frequency: $f_c' = 5.255$ GHz;
- Bandwidth: $B = 100$ MHz;
- Interval between the frequencies: $\triangle f' = 1.957 \cdot 10^5$ Hz;
- Time between channel snapshots: $\triangle t = 0.07$ s;
- Impulse response length: 5.12 μs.

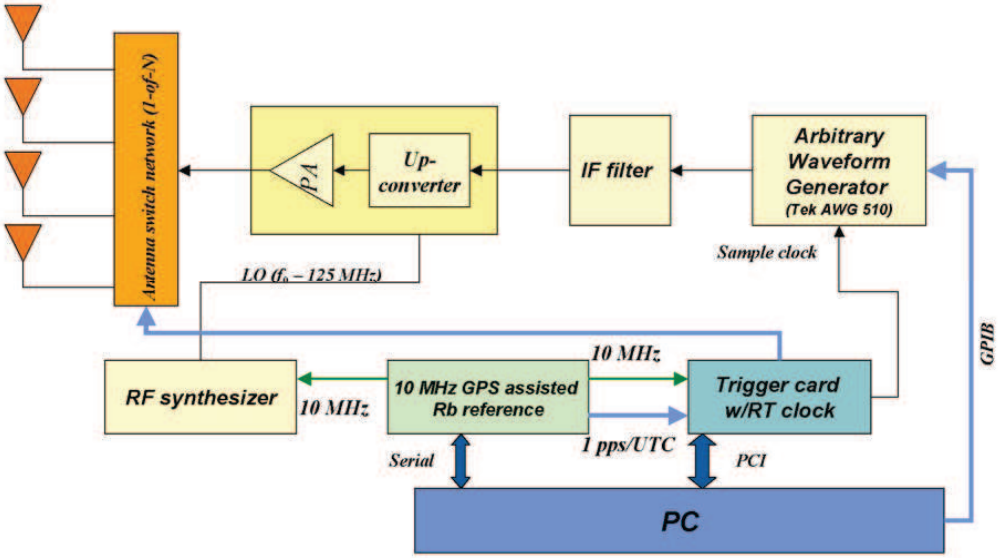

Figure A.1: Channel sounder transmitter.

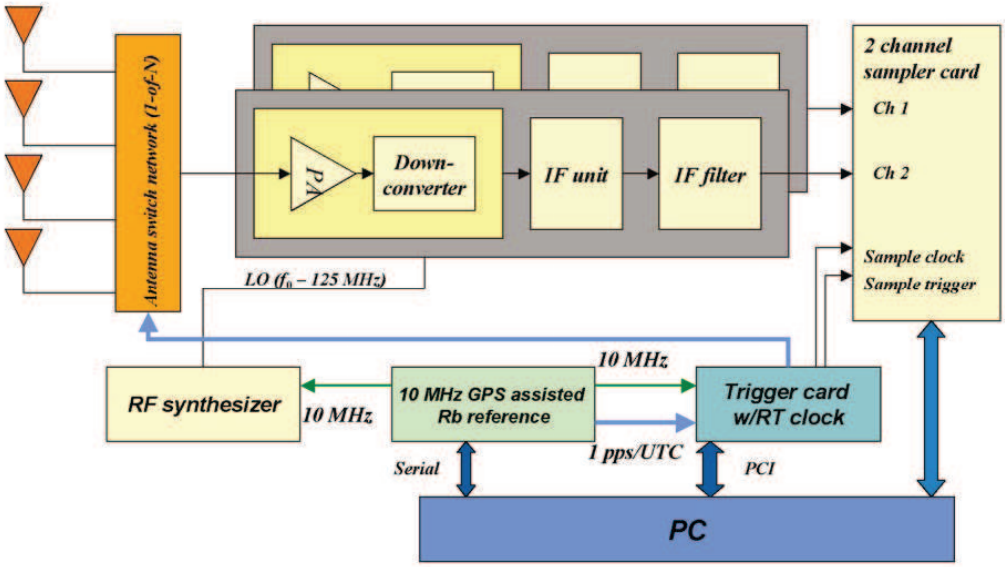

Figure A.2: Channel sounder receiver.

A.2 Propagation Scenarios

A.2.1 Micro Cell Site - Regular Street Geometry

This site is a part of Oslo downtown with a regular street grid. The building mass is homogenous and materials used are mostly brick and concrete. The building height varies between 20 – 30 m. In Fig. A.3, the position of the receiving antenna is shown.

The measurement route is shown on the map in Fig. A.4. The photo of the measurement route is depicted in Fig. A.5.

Figure A.3: Position of the receiving antenna (micro cell site – regular street geometry).

Figure A.4: Map of the measurement route (micro cell site – regular street geometry).

Figure A.5: Photo of the measurement route (micro cell site – regular street geometry).

A.2.2 Micro Cell Site - Open Market Place

The second measurement site is a market square partly filled with market stalls. The surrounding buildings are of variable size and height. The size of the square is about $100 \times 100\,\mathrm{m}^2$. One side of the square is approximately 5 m above the other. The receiving antenna was placed at the elevated side of the square. The position of the receiving antenna is marked with a red circle in Fig. A.6. The measurement route is shown in Fig. A.7.

Figure A.6: Position of the receiving antenna (micro cell site - open market place).

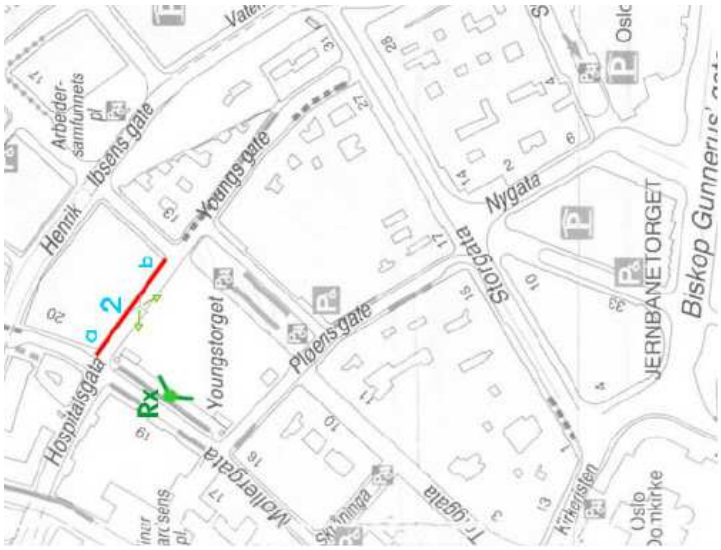

Figure A.7: Map of the measurement route (micro cell site – open market place).

A.2.3 Micro/Pico Cell Site - Passageway

At the south-east side of the market square, described in the previous subsection, a pedestrian passageway leads through a building to the next street. The route is shown on the map in Fig. A.8. This site was chosen for testing the so-called 'key-hole' effect.

The interior of the passageway is presented in Fig. A.9.

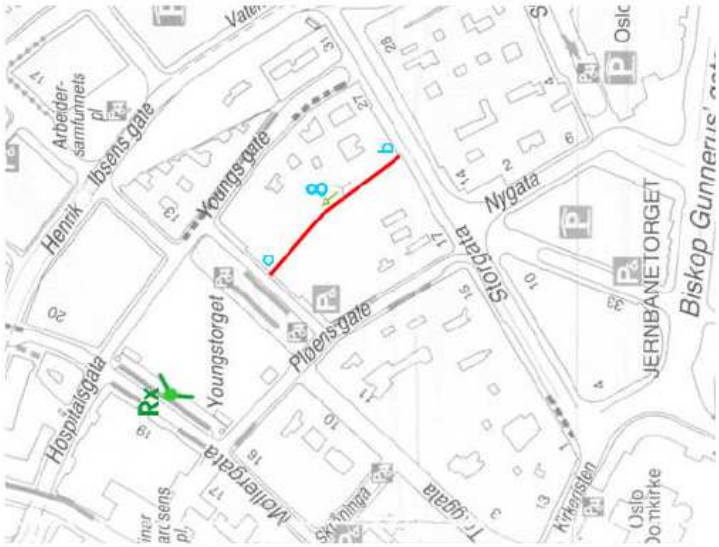

Figure A.8: Map of the measurement route (micro/pico cell site - passageway).

Figure A.9: Photo of the measurement route (micro/pico cell site - passageway).

A.2.4 Indoor Cell Site

The indoor measurements were performed in the Telenor headquarters building. This is a modern office building with open indoor areas. The building materials used are mostly glass and steel with wood covered computer floors or stone tiles. Very few cubicle offices are used. The working zones are with a high degree of openness. The building has an irregular structure.

The interior of the working zone at Telenor headquarters is shown in Fig. A.10. The map of the measurement route and the photo of the route are shown in Figs. A.11 and A.12, respectively.

Figure A.10: Working zone interior (indoor cell site).

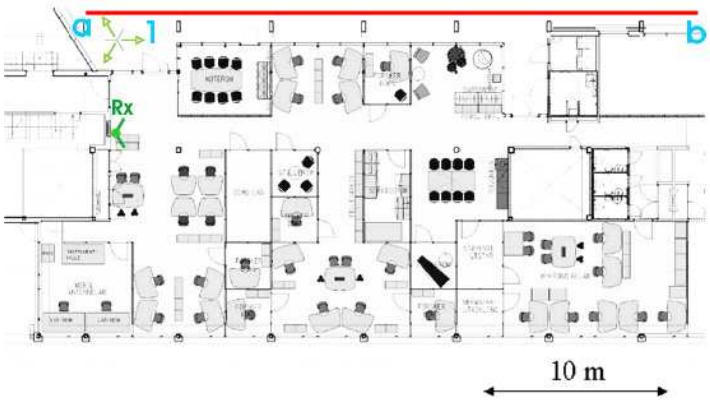

Figure A.11: Map of the measurement route (indoor cell site).

Figure A.12: Photo of the measurement route (indoor cell site).

References

[1] M. K. Simon and M.-S. Alouini, *Digital Communication over Fading Channels*. Wiley, 2000.

[2] T. Rappaport, *Wireless Communications: Principles and Practice*, 2nd ed. NJ: Printice Hall PTR, 2002.

[3] R. Vaughan and J. B. Andersen, *Channels, Propagation and Antennas for Mobile Communications*. Institution of Electrical Engineers, London, UK, 2003.

[4] A. F. Molisch, *Wireless Communications*. Chichester: Wiley-IEEE Press, 2005.

[5] P. Almers, E. Bonek, A. Burr *et al.*, "Survey of channel and radio propagation models for wireless MIMO systems," *EURASIP Journal on Wireless Communications and Networking*, vol. 2007, pp. Article ID 19 070, 19 pages, 2007, doi:10.1155/2007/19070.

[6] K. Yu and B. Ottersten, "Models for MIMO propagation channels: A review," *Wireless Communications and Mobile Computing*, vol. 2, pp. 653–666, 2002, doi: 10.1002/wcm.78.

[7] M. Steinbauer, A. F. Molisch, and E. Bonek, "The double-directional radio channel," *IEEE Antennas Propag. Mag.*, vol. 43, no. 4, pp. 51–63, Aug. 2001.

[8] B. H. Fleury, P. Jourdan, and A. Stucki, "High-resolution channel parameter estimation for MIMO applications using the SAGE algorithm," in *2002 Int. Zurich Seminar on Broadband Communications*, Zurich, Switzerland, Feb. 2002, pp. 30–1–30–9.

[9] R. T. A. Richter, M. Landmann, "RIMAX – a flexible algorithm for channel parameter estimation from channel sounding measurements," COST 273, Athens, Greece, Tech. Rep. TD(04)045, Jan. 2004.

[10] P. Bello, "Characterization of randomly time-variant linear channels," *IEEE Trans. Commun. Syst.*, vol. 11, no. 4, pp. 360–393, Dec. 1963.

[11] G. D. Durgin, *Space–Time Wireless Channels*. NJ: Prentice Hall, 2003.

[12] J. D. Parsons, *The Mobile Radio Propagation Channel*, 2nd ed. John Wiley & Sons, 2000.

[13] D. B. Percival, "Simulating Gaussian random processes with specified spectra," *Computing Science and Statistics*, vol. 24, pp. 534–538, 1992.

[14] G. E. Johnson, "Constructions of particular random processes," *Proc. IEEE*, vol. 82, no. 2, pp. 270–285, Feb. 1994.

[15] V. P. Bakalov, *Numerical Simulation of Random Processes.* Science-Press, 2002, in Russian.

[16] R. Parra-Michel, V. Y. Kontorovitch, and A. G. Orozco-Lugo, "Simulation of wideband channels with non-separable scattering functions," in *Proc. IEEE International Conference on Acoustics, Speech, and Signal Processing (ICASSP '02)*, vol. 3, 13–17 May 2002, pp. III–2829–III–2832.

[17] G. Matz, "On non-WSSUS wireless fading channels," *IEEE Trans. Wireless Commun.*, vol. 4, no. 5, pp. 2465–2478, Sep. 2005.

[18] I. G. A. Gehring, M. Steinbauer and M. Grigat, "Empirical channel stationarity in urban environments," in *Proceedings of the 4th European Personal Mobile Communications Conference (EPMCC '01)*, Vienna, Austria, Feb 2001.

[19] S. Kay, "A new nonstationarity detector," *IEEE Trans. Signal Process.*, vol. 56, no. 4, pp. 1440–1451, April 2008.

[20] R. J. C. Bultitude, G. Brussaard, M. H. A. J. Herben, and T. J. Willink, "Radio channel modelling for terrestrial vehicular mobile applications," in *Proc. Millenium Conf. Antennas and Propagation*, Davos, Switzerland, Apr. 2000, pp. 1–5.

[21] J. S. Bendat and A. G. Peirsol, *Random Data: Analysis and Measurement Procedures*, 3rd ed. NY: Wiley-Interscience, 2000.

[22] R. J. C. Bultitude, "Estimating frequency correlation functions from propagation measurements on fading radio channels: a critical review," *IEEE J. Sel. Areas Commun.*, vol. 20, no. 6, pp. 1133–1143, Aug. 2002.

[23] T. J. Willink, "Wide-sense stationarity of mobile MIMO radio channels," *IEEE Trans. Veh. Technol.*, vol. 57, no. 2, pp. 704–714, March 2008.

[24] M. B. Priestley and T. S. Rao, "A test for non-stationarity of time-series," *J. R. Stat. Soc., Ser. B*, vol. 31, no. 1, pp. 140–149, 1969.

[25] R. von Sachs and M. H. Neumann, "A wavelet-based test for stationarity," *Journal of Time Series Analysis*, vol. 21, no. 5, pp. 597 – 613, 2002.

[26] J. Xiao, P. Borgnat, P. Flandrin, and C. Richard, "Testing stationarity with surrogates - a one-class SVM approach," in *IEEE/SP 14th Workshop on Statistical Signal Processing, 2007, SSP '07*, Aug 2007, pp. 720–724.

[27] D. Umansky and M. Pätzold, "Stationarity test for wireless communication channels," accepted for publication in IEEE Global Telecommunications Conference (GLOBECOM 2009).

[28] A. Papoulis and S. U. Pillai, *Probability, Random Variables and Stochastic Processes*, 4th ed. New York: McGraw-Hill, 2002.

[29] D. B. Percival and A. T. Walden, *Wavelet Methods for Time Series Analysis.* Cambridge University Press, 2006.

[30] Y. Ephraim and M. Rahim, "On second-order statistics and linear estimation of cepstral coefficients," *IEEE Trans. Speech Audio Process.*, vol. 7, no. 2, pp. 162–176, Mar. 1999.

[31] P. Stoica and N. Sandgren, "Smoothed nonparametric spectral estimation via cepsturm thresholding - introduction of a method for smoothed nonparametric spectral estimation," *IEEE Signal Process. Mag.*, vol. 23, no. 6, pp. 34–45, Nov. 2006.

[32] V. S. Pugachev, *Probability Theory and Mathematical Statistics for Engineers.* Oxford: Pergamon Press, 1984.

[33] G. A. F. Seber, *Multivariate Observations.* Wiley, 2004.

[34] S. L. Marple, *Digital Spectral Analysis with Applications.* NJ: Prentice Hall, 1987.

[35] M. Pätzold and B. O. Hogstad, "Design and performance of MIMO channel simulators derived from the two-ring scattering model," in *Proc. 14th IST Mobile & Communications Summit, IST 2005*, Dresden, Germany, June 2005.

[36] J. C. Spall, *Introduction to Stochastic Search and Optimization: Estimation, Simulation, and Control.* NJ: John Wiley & Sons, 2003.

[37] S. Sorooshyari and D. G. Daut, "Generation of correlated Rayleigh fading envelopes for accurate performance analysis of diversity systems," in *Proc. 14th IEEE on Personal, Indoor and Mobile Radio Communications PIMRC 2003*, vol. 2, 7–10 Sept. 2003, pp. 1800–1804.

[38] J. P. Kermoal, L. Schumacher, K. I. Pedersen, P. E. Mogensen, and F. Frederiksen, "A stochastic MIMO radio channel model with experimental validation," *IEEE J. Sel. Areas Commun.*, vol. 20, no. 6, pp. 1211–1226, Aug. 2002.

[39] W. Weichselberger, M. Herdin, H. Ozcelik, and E. Bonek, "A stochastic MIMO channel model with joint correlation of both link ends," *IEEE Trans. Wireless Commun.*, vol. 5, no. 1, pp. 90–100, Jan. 2006.

[40] K. I. Pedersen, J. B. Andersen, J. P. Kermoal, and P. Mogensen, "A stochastic multiple-input multiple-output radio channel model for evaluation of space-time coding algorithms," in *Proc. 52nd Vehicular Technology Conference IEEE VTS-Fall VTC 2000*, vol. 2, 24–28 Sept. 2000, pp. 893–897.

[41] K. Yu, M. Bengtsson, B. Ottersten, D. McNamara, P. Karlsson, and M. Beach, "Modeling of wide-band MIMO radio channels based on NLoS indoor measurements," *IEEE Trans. Veh. Technol.*, vol. 53, no. 3, pp. 655–665, May 2004.

[42] N. Costa and S. Haykin, "A novel wideband MIMO channel model and experimental validation," *IEEE Trans. Antennas Propag.*, vol. 56, no. 2, pp. 550–562, Feb. 2008.

[43] C. Xiao, J. Wu, S. Y. Leong, Y. R. Zheng, and K. B. Letaief, "A discrete-time model for triply selective MIMO Rayleigh fading channels," *IEEE Trans. Wireless Commun.*, vol. 3, no. 5, pp. 1678–1688, Sept. 2004.

[44] J. Mietzner, C. Xiao, P. A. Hoeher, and K. Ben Letaief, "A note on discrete-time triply-selective MIMO Rayleigh fading channel models," *IEEE Trans. Wireless Commun.*, vol. 7, no. 3, pp. 837–837, March 2008.

[45] A. Alcocer-Ochoa, V. Y. Kontorovitch, and R. Parra-Michel, "A wideband MIMO channel simulator using the Kronecker model," in *Proc. 3rd International Conference on Electrical and Electronics Engineering*, 6–8 Sept. 2006, pp. 1–4.

[46] ——, "An orthogonalization approach for communication channel modeling," in *Proc. VTC-2005-Fall Vehicular Technology Conference 2005 IEEE 62nd*, vol. 2, 25–28 Sept., 2005, pp. 1079–1083.

[47] D. Umansky and M. Pätzold, "Design of measurement-based stochastic wideband MIMO channel simulators," accepted for publication in IEEE Global Telecommunications Conference (GLOBECOM 2009).

[48] ——, "Estimation of path gains and Doppler frequencies from the temporal autocorrelation function of mobile fading channels," presented at the 13th European Wireless Conf., 2007.

[49] ——, "Design of measurement-based wideband mobile radio channel simulators," in *Proc. 4th International Symposium on Wireless Communication Systems ISWCS 2007*, Oct. 17–19, 2007, pp. 229–235.

[50] ——, "Design of wideband mobile radio channel simulators based on real-world measurement data," in *Proc. IEEE Vehicular Technology Conference VTC Spring 2008*, May 11–14, 2008, pp. 319–324.

[51] K. W. Yip and T. S. Ng, "Karhunen-Loeve expansion of the WSSUS channel output and its application to efficient simulation," *IEEE J. Sel. Areas Commun.*, vol. 15, no. 4, pp. 640–646, May 1997.

[52] V. S. Pugachev and I. N. Sinitsyn, *Stochastic Systems: Theory and Applications*. World Scientific Publishing Company, 2002.

[53] L. E. Franks, *Signal Theory*. Prentice Hall, 1969.

[54] H. L. V. Trees, *Detection, Estimation, and Modulation Theory.* Wiley-Interscience, 2001, vol. Part I.

[55] S. Mallat, *A Wavelet Tour of Signal Processing*, 2nd ed. Academic Press, 1999.

[56] K. Werner, M. Jansson, and P. Stoica, "On estimation of covariance matrices with Kronecker product structure," *IEEE Trans. Signal Process.*, vol. 56, no. 2, pp. 478–491, Feb. 2008.

[57] S. G. Mallat and Z. Zhang, "Matching pursuits with time-frequency dictionaries," *IEEE Trans. Signal Process.*, vol. 41, no. 12, pp. 3397–3415, Dec. 1993.

[58] C. D. Meyer, *Matrix Analysis and Applied Linear Algebra.* SIAM, 2001.

[59] P. Stoica and Y. Selen, "Cyclic minimizers, majorization techniques, and the expectation-maximization algorithm: a refresher," *IEEE Signal Process. Mag.*, vol. 21, no. 1, pp. 112–114, Jan 2004.

[60] J. Benesty, M. M. Sondhi, and Y. Huang, Eds., *Springer Handbook of Speech Processing.* Springer, 2007.

[61] M. Unser, "On the approximation of the discrete Karhunen-Loève transform for stationary processes," *Signal Processing*, vol. 7, no. 3, pp. 231–249, December 1984.

[62] D. N. Politis, "Computer-intensive methods in statistical analysis," *IEEE Signal Process. Mag.*, vol. 15, no. 1, pp. 39–55, Jan. 1998.

[63] D. Umansky and M. Pätzold, "A two-dimensional autoregressive model for MIMO wideband mobile radio channels," in *Proc. IEEE Global Telecommunications Conference IEEE GLOBECOM 2008*, Nov. 2008, pp. 1–6.

[64] S. M. Kay, *Modern Spectral Estimation, Theory and Application.* NJ: Prentice Hall, 1988.

[65] P. Stoica and R. L. Moses, *Spectral Analysis of Signals.* NJ: Prentice Hall, 2005.

[66] S. J. Howard and K. Pahlavan, "Autoregressive modeling of wide-band indoor radio propagation," *IEEE Trans. Commun.*, vol. 40, no. 9, pp. 1540–1552, Sep. 1992.

[67] K. E. Baddour and N. C. Beaulieu, "Accurate simulation of multiple cross-correlated Rician fading channels," *IEEE Trans. Commun.*, vol. 52, no. 11, pp. 1980–1987, Nov. 2004.

[68] ——, "Autoregressive modeling for fading channel simulation," *IEEE Trans. Wireless Commun.*, vol. 4, no. 4, pp. 1650–1662, Jul. 2005.

[69] C. W. Therrien and H. T. El-Shaer, "Multichannel 2-D AR spectrum estimation," *IEEE Trans. Acoust., Speech, Signal Process.*, vol. 37, no. 11, pp. 1798–1800, Nov. 1989.

[70] D. E. Dudgeon and R. M. Mersereau, *Multidimensional Digital Signal Processing.* NJ: Prentice Hall, 1984.

[71] C. W. Therrien, "Relations between 2-D and multichannel linear prediction," *IEEE Trans. Acoust., Speech, Signal Process.*, vol. 29, no. 3, pp. 454–456, Nov. 1981.

[72] E. I. Jury, "Stability of multidimensional scalar and matrix polynomials," *Proc. IEEE*, vol. 66, no. 9, pp. 1018–1047, Sep. 1978.

[73] T. Kaczorek, *Two-Dimensional Linear Systems.* Berlin: Springer-Verlag, 1985.

[74] R. P. Roesser, "A discrete state-space model for linear image processing," *IEEE Trans. Autom. Control*, vol. 20, no. 1, pp. 1–10, Feb. 1975.

[75] F. Gembicki and Y. Haimes, "Approach to performance and sensitivity multiobjective optimization: The goal attainment method," *IEEE Trans. Autom. Control*, vol. 20, no. 6, pp. 769–771, Dec. 1975.

[76] P. J. Fleming and A. P. Pashkevich, "Application of multi-objective optimisation to compensator design for SISO control systems," *Electronics Letters*, vol. 22, no. 5, pp. 258–259, Feb. 1986.

[77] L. Ljung, *System Identification: Theory for the User*, 2nd ed. Prentice Hall PTR, 1999.

[78] P. Stoica and Y. Selen, "Model-order selection: a review of information criterion rules," *IEEE Signal Process. Mag.*, vol. 21, no. 4, pp. 36–47, July 2004.

[79] E. O. Brigham, *The Fast Fourier Transform and Its Applications.* NJ: Prentice Hall, 1988.

[80] M. D. Austin and G. L. Stüber, "Velocity adaptive handoff algorithms for microcellular systems," *IEEE Trans. Veh. Technol.*, vol. 43, no. 3, pp. 549–561, Aug. 1994.

[81] A. Sampath and J. M. Holtzman, "Estimation of maximum Doppler frequency for handoff decisions," in *IEEE 43th Vehicular Technology Conf.*, Secaucus, NJ, USA, May 1993, pp. 859–862.

[82] K. D. Anim-Appiah, "On generalized covariance-based velocity estimation," *IEEE Trans. Veh. Technol.*, vol. 48, no. 5, pp. 1546–1557, Sep. 1999.

[83] R. Narasimhan and D. C. Cox, "Speed estimation in wireless systems using wavelets," *IEEE Trans. Commun.*, vol. 47, no. 9, pp. 1357–1364, Sep. 1999.

[84] K. E. Baddour and N. C. Beaulieu, "Robust Doppler spread estimation in nonisotropic fading channels," *IEEE Trans. Wireless Commun.*, vol. 4, no. 6, pp. 2677–2682, Nov. 2005.

[85] G. Azemi, B. Senadji, and B. Boashash, "Mobile unit velocity estimation based on the instantaneous frequency of the received signal," *IEEE Trans. Veh. Technol.*, vol. 53, no. 3, pp. 716–724, May 2004.

[86] M. Türkboylari and G. Stüber, "Eigen-matrix pencil method-based velocity estimation for mobile cellular radio systems," in *2000 IEEE Int. Conf. on Communications (ICC 2000)*, vol. 2, New Orleans, LA, USA, Jun. 2000, pp. 690–694.

[87] W. Sheng and S. D. Blostein, "SNR-independent velocity estimation for mobile cellular communications systems," in *Proc. IEEE Int. Conf. on Acoustics, Speech, and Signal Processing (ICASSP'02)*, vol. 3, Orlando, Florida, USA, May 2002, pp. 2469–2472.

[88] M. Ibnkahla, *Signal Processing for Mobile Communications Handbook*. CRC Press, 2004.

[89] A. Abdi, H. Zhang, and C. Tepedelenlioglu, "A unified approach to the performance analysis of speed-estimation techniques in mobile communication," *IEEE Trans. Commun.*, vol. 55, no. 12, pp. 2381–2381, Dec. 2007.

[90] J. Gozalvez, "Ultra Mobile Broadband [Mobile Radio]," *IEEE Veh. Technol. Mag.*, vol. 2, no. 1, pp. 51–55, Mar. 2007.

[91] B. Li *et al.*, "A survey on mobile WiMAX," *IEEE Commun. Mag.*, vol. 45, no. 12, pp. 70–75, Dec. 2007.

[92] H. Zhang and A. Abdi, "Nonparametric mobile speed estimation in fading channels: Performance analysis and experimental results," *IEEE Trans. Wireless Commun.*, vol. 8, no. 4, pp. 1683–1692, April 2009.

[93] D. Umansky and M. Pätzold, "Velocity estimation in wideband mobile stations equipped with multiple antennas," in *Proc. IEEE 69th Vehicular Technology Conference VTC Spring 2009*, Apr. 26–29, 2009, pp. 1–6.

[94] D. H. Johnson and D. E. Dudgeon, *Array signal processing: Concepts and Techniques*. NJ: Prentice Hall, 1993.

[95] S. V. Huffel and J. Vandewalle, *The Total Least Squares Problem: Computational Aspects and Analysis*. SIAM, 1991.

[96] B. D. Van Veen and K. M. Buckly, "Beamforming: A versatile approach to spatial filtering," *IEEE ASSP Mag.*, vol. 5, no. 2, pp. 4–24, Apr. 1988.

[97] V. Erceg *et al.*, "A model for the multipath delay profile of fixed wireless channels," *IEEE J. Sel. Areas Commun.*, vol. 17, no. 3, pp. 399–410, Mar. 1999.